CONTRACTOR REPORT

SAND91—7034
Unlimited Release
UC—814

Yucca Mountain Site Characterization Project

Numerical Studies of Rock-Gas Flow in Yucca Mountain

Benjamin Ross, Steven Amter, Ning Lu
Disposal Safety Incorporated
1660 L Street, NW, Suite 314
Washington, DC 20036

Prepared by Sandia National Laboratories Albuquerque, New Mexico 87185 and Livermore, California 94550 for the United States Department of Energy under Contract DE-AC04-76DP00789

Printed February 1992

"Prepared by Yucca Mountain Site Characterization Project (YMSCP) participants as part of the Civilian Radioactive Waste Management Program (CRWM). The YMSCP is managed by the Yucca Mountain Project Office of the U.S. Department of Energy, DOE Field Office, Nevada (DOE/NV). YMSCP work is sponsored by the Office of Geologic Repositories (OGR) of the DOE Office of Civilian Radioactive Waste Management (OCRWM)."

Issued by Sandia National Laboratories, operated for the United States Department of Energy by Sandia Corporation.

Available to DOE and DOE contractors from
Office of Scientific and Technical Information
PO Box 62
Oak Ridge, TN 37831

Prices available from (615) 576-8401, FTS 626-8401

Available to the public from
National Technical Information Service
US Department of Commerce
5285 Port Royal Rd
Springfield, VA 22161

NTIS price codes:
Printed copy: A06
Microfiche copy: A01

SAND91-7034
Unlimited Release
Printed February 1992

Distribution
Category UC-814

Numerical Studies of Rock-Gas Flow in Yucca Mountain

Benjamin Ross, Steven Amter, and Ning Lu

Disposal Safety Incorporated
1660 L Street, N.W., Suite 314
Washington, D.C. 20036
(202) 293-3993

Prepared for

Sandia National Laboratories
System Performance Assessment Division
Albuquerque, N.M. 87185

Under Sandia Contract 54-9698
Contract monitor, Michael L. Wilson

Abstract

A computer model (TGIF—Thermal Gradient Induced Flow) of two-dimensional, steady-state rock-gas flow driven by temperature and humidity differences is described. The model solves for the "fresh-water head," a concept that has been used in models of variable-density water flow but has not previously been applied to gas flow. With this approach, the model can accurately simulate the flows driven by small differences in temperature. The unsaturated tuffs of Yucca Mountain, Nevada, are being studied as a potential site for a repository for high-level nuclear waste. Using the TGIF model, preliminary calculations of rock-gas flow in Yucca Mountain are made for four east-west cross-sections through the mountain. Calculations are made for three repository temperatures and for several assumptions about a possible semi-confining layer above the repository. The gas-flow simulations are then used to calculate travel-time distributions for air and for radioactive carbon-14 dioxide from the repository to the ground surface.

The work described in this report was performed under Yucca Mountain Site Characterization Project Work Breakdown Structure Element 1.2.1.4.1.

TABLE OF CONTENTS

LIST OF TABLES

LIST OF FIGURES

CHAPTER 1
INTRODUCTION

The potential nuclear waste repository at Yucca Mountain, Nevada, would be located above the water table in partially saturated tuff. Gas in the rock, called "rock gas," fills most of the larger-diameter pores and fractures and can move through it. Flow of rock gas may be important for several reasons:

- Carbon-14 released from the repository would migrate in the gas phase.
- Flow of water vapor out of the mountain may make an important contribution to the water balance.
- Gas convection may be a significant mechanism for removal of heat from the repository.

Field observations [Weeks, 1987; 1991] show that large-scale flows of air through Yucca Mountain are driven by the combination of topographic relief and temperature differences between the surface and subsurface. Because the subsurface is, on average, warmer than the atmosphere, there is a "chimney effect" which causes warm gas inside the mountain to rise. This flow is most rapid in winter and partially reverses itself in summer. Lesser but significant contributions to rock gas flow are made by barometric pressure fluctuations, aerodynamic effects of wind blowing over the mountain, and the effect on density of the humidity difference between rock gas and air. Because the Yucca Mountain unsaturated zone has a large thickness and permeabiliity, the magnitude of these flows can be substantial.

We have developed a model of rock-gas flow driven by temperature and humidity differences. The model, called TGIF (Thermal Gradient Induced Flow), calculates two-dimensional steady-state flows. A steady-state model cannot simulate flows driven by driving forces that change so fast that pressures cannot equilibrate through the system; examples of such driving forces at Yucca Mountain are barometric pressure fluctuations and temperature differences between day and night. These rapidly oscillating flows are omitted from the model; they may remove a significant amount of water from the mountain, but because their time scales are too short to allow the pressure changes to penetrate very far into the mountain [Montazer et al., 1985] they do not cause net movement of gas at depth. Consequently they should not significantly affect contaminant transport or heat transfer.

Another phenomenon not treated by the model, wind, does appear to drive a substantial net gas flux at depth [Weeks, 1991]; further research is needed to devise a way to model this effect.

The TGIF model solves for the "fresh-water head," a concept which has been used in models of variable-density water flow but has not previously been applied to gas flow. With this approach, the model can accurately simulate the flows driven by small differences in temperature. Existing models of rock-gas flow (such as the TOUGH model used by Tsang and Pruess [1987]), which solve for the pressure, tend to lose accuracy when temperature differences become small. As temperatures approach the boiling point of water, TGIF becomes inapplicable; it thus complements TOUGH, which can simulate flows at higher temperatures.

Using the TGIF model, we have calculated the annual-average rock-gas flow through Yucca Mountain. The calculations use four parallel, east-west cross-sections which are equally spaced through the potential repository. Simulated topography and stratigraphy were taken from the Sandia National Laboratories Interactive Graphics Information System and U.S. Geological Survey topographic and geologic maps. The system was simulated with the natural geothermal temperature gradient and with the repository heated to 315 K and 330 K; temperature fields were obtained by solving the steady-state heat conduction equation. (This is an approximation; in future work, convection terms will be added to the heat transfer model.) Two different values for the permeability of the Paintbrush nonwelded tuff unit, which acts as a semi-confining bed for gas flow, were simulated.

For each simulation, travel paths were determined for 323 particles traveling from points evenly distributed throughout the potential repository area to the surface. Travel times were calculated along each path line for both an unretarded particle that moves with the rock gas and a particle of carbon-14 that is retarded by isotopic exchange with bicarbonate dissolved in the aqueous phase. (The concentration of dissolved bicarbonate was determined by assuming thermodynamic equilibrium with solid calcite and the measured rock-gas composition.)

The results of these calculations are presented as histograms of travel times. Each histogram represents the distribution of travel times throughout the repository (combining all four cross-sections) for a given repository temperature and confining-bed permeability.

Chapters 2 through 4 of this report present the models. Chapter 2 derives the equations for gas flow in terms of fresh water head and describes the model's implementation. Chapter 3 presents the heat-conduction model which is used to calculate temperatures as input to the gas-flow model. Chapter 4 describes the particle-tracking program which is used to compute gas flow lines and particle travel times.

The next two chapters present results of analyses of gas flow at Yucca Mountain. Chapter 5 gives the results of a sensitivity study to determine the effect of varying poorly known parameters. Chapter 6 presents the principal results of the study, the calculations of flow along four parallel cross-sections through the proposed repository site. Chapter 7 summarizes the conclusions of the study and makes recommendations for further research.

CHAPTER 2
THE GAS FLOW MODEL

2.1 Physical basis

Yucca Mountain has the geometry of a linear ridge and is underlain by a 500-m-thick unsaturated zone that is composed of alternating layers of ash-flow and bedded tuffs [Scott and Bonk, 1984]. Intrinsic permeabilities in the ash-flow tuffs are high due to welding and consequent fracturing. Because the water table lies below the elevation of the adjoining valleys, rock gas can circulate throughout the mountain.

The density of a gas is dependent upon temperature, composition, and pressure. Temperatures inside Yucca Mountain vary much less than in the surrounding atmosphere and the density of pore gas in the mountain reflects this. The composition of the gas in the mountain differs markedly from the atmosphere. Inside the mountain, the gas is generally saturated with water vapor, while the surrounding atmosphere is usually extremely dry. The gas inside the mountain also appears to contain more carbon dioxide than the atmosphere [Yang et al., 1985]. Because water vapor is lighter than air, rock gas will be less dense than air at equal temperature. (The density effects of carbon dioxide are small compared to those of water vapor.)

The density contrast is greatest in the winter, because the gas inside the mountain is warmer and wetter than the atmosphere, and the flow velocities are greatest at that season. The pattern of circulation is shown in Figure 2-1a. Dense air from the atmosphere displaces lighter air in the mountain, resulting in an outward flow of air at the peak and an inward flow at the base. In the summer, gas inside the mountain still is wetter, but the temperature pattern is reversed. The density contrast is thus not as great as in the winter, and gas flow velocities are correspondingly lower. The general summertime pattern of flow is shown in Figure 2-1b. Cooler air inside the mountain sinks, resulting in inward flow at the peak and outward flow at the base of the mountain. During the summer, when night-time air temperatures may be lower than inside the mountain, low-velocity diurnal reversals of airflow sometimes occur in boreholes.

Over periods of hours or days, barometric pressure fluctuations and pressures induced by winds impinging on the mountain also make a significant contribution to gas flow [Weeks, 1987; 1991]. These phenomena are not included in the model.

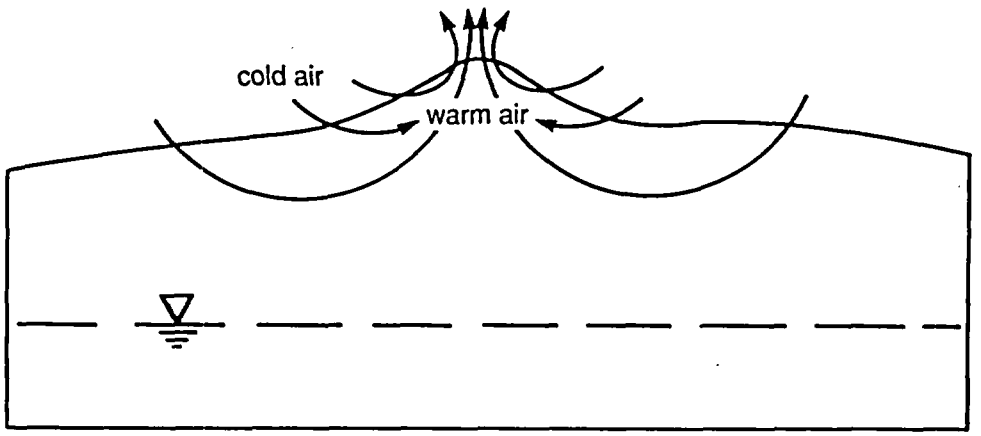

a. **Winter**

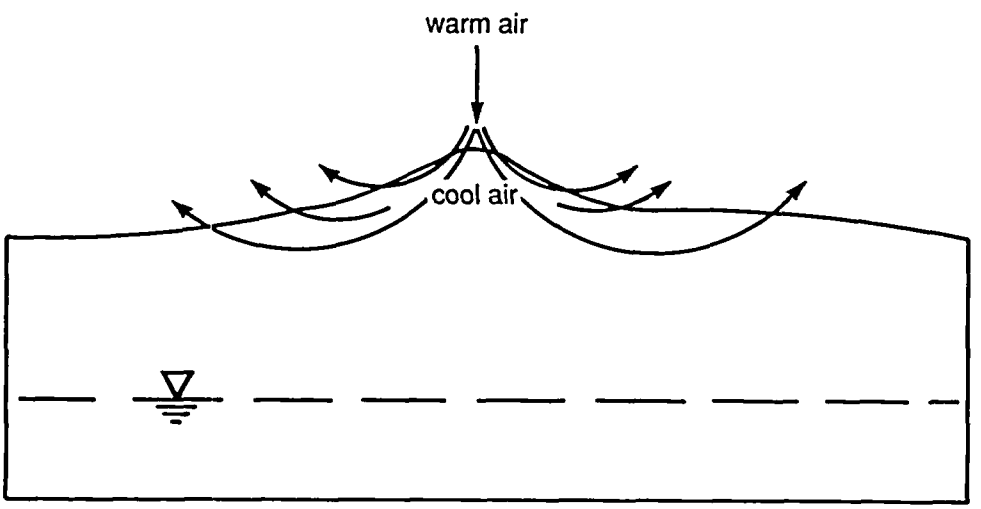

b. **Summer**

Figure 2-1. Seasonal air flow at Yucca Mountain; (a) warm air rising inside the mountain during winter; (b) cool air sinking during summer.

2.2 Governing equation for rock-gas flow

2.2.1 Assumptions

The modeling approach taken here is to assume that the rock gas is always saturated with water vapor (that is, its relative humidity is 100%). As gas flows through regions of differing temperature and pressure in the mountain, moisture evaporates or condenses so as to maintain this condition. This assumption determines the gas density as a function of pressure and temperature; with the fluid properties thus specified, equations for buoyant flow can be derived and solved.

More specifically, this modeling approach involves several assumptions:

Thermodynamic equilibrium exists among air, water vapor, and water. This assumption is justified by the intimate contact between air and water in small pores in the subsurface of Yucca Mountain.

The gas is saturated with water vapor. Measurements indicate that moisture suction at Yucca Mountain is a few tens of meters. As the thermodynamic quantity RT, when converted to units of unsaturated-zone suction potential, is equivalent to 14 km of head, this causes a vapor pressure lowering of less than 1%.

The gas behaves as an ideal gas. This assumption, although it is an approximation, will create very little inaccuracy as long as we treat both air and rock gas consistently.

Changes in partial pressure of water vapor are accommodated by changes in gas composition, with the total pressure remaining nearly constant. This assumption implies, for example, that a rise in temperature evaporates additional water (relative humidity remains at 100%), increasing both the mass of water in the vapor state and the vapor pressure, but the partial pressure of air decreases almost equally (air flows out of the elemental volume) and total pressure remains nearly constant.

Molecular diffusion resulting from gradients of water vapor partial pressure has a negligible effect on gas flow. The basis for this assumption is given in Appendix A.

The unsaturated zone stays at constant saturation. This implies that there is a source of water that replenishes water lost to evaporation and mixing with drier air from the surrounding atmosphere. The water source is probably some combination of precipitation and upward flow from the water table. Both field experiment results and numerical simulations [Doughty and Pruess, 1990] show that this remains true under Yucca Mountain conditions until temperatures reach the boiling point of water.

In the development of our model, a few additional simplifying assumptions not required by the general approach have been made. These are:

The gas flow field is at steady state. Data of Montazer et al. [1985] show that pressure throughout the mountain equilibrates on a time scale of weeks to months. Therefore, this assumption should be good enough to calculate the ^{14}C migration over a period of many years.

Gas viscosity is independent of pressure. The pressure-dependence of the dynamic viscosity of air is extremely small and can safely be ignored.

Acceleration of gravity is uniform.

Gas permeability is independent of pressure. Data reviewed by Tsang [1991] show that hydrostatic pressures must approach 10% of the lithostatic pressure before the fracture permeability changes appreciably. As the pressure changes treated here are many orders of magnitude smaller, this assumption should be very good.

All gas-filled voids in the matrix may be treated as a single porosity on time scales of years. This assumption is analyzed in detail in Appendix B, where it is shown to be very accurate for computations of carbon-14 migration.

2.2.2 Derivation

The assumptions listed in the previous section imply that the system can be described by three equations: a constitutive relation, Darcy's Law, and a volume balance.[1]

The constitutive relation is easily derived. From the assumptions that the rock gas behaves as an ideal gas and the humidity is always 100%, a constitutive relation may be written as

$$\rho = \frac{1}{RT}\left[P_v\Omega_v + (P - P_v)\Omega_a\right] \tag{2-1}$$

where ρ is the fluid density, R is the gas constant, T is the temperature, P_v is the vapor pressure of water (which depends on temperature), and Ω_v and Ω_a are the molar weights of water and dry air.

Darcy's Law relates the gas flux to the applied forces. In this case, there are two forces: gravity and the pressure gradient. The gas flux is therefore

$$\mathbf{q} = -\frac{k}{\mu}(\nabla P - g\rho\hat{z}) \tag{2-2}$$

where g is the acceleration of gravity and $\hat{z}$ is a downward-pointing unit vector.

The volume balance is the most complex of these governing equations. Consider now the flow of rock gas (air and water vapor) through a very small cube of space in the unsaturated zone, as illustrated in Figure 2-2, in the presence of gradients of temperature and pressure. The volume of gas leaving the cube per unit time will generally differ from the volume entering the cube, because gradients of temperature and pressure can cause expansion or contraction.

---

[1]A volume balance is used rather than a mass balance because the volume flux of a fluid, rather than the mass flux, is related to the applied forces by Darcy's Law. In a system such as this one where fluid composition varies, mass fluxes due to binary diffusion can exist in the absence of any applied force. Such fluxes are not predicted by Darcy's Law. The mass balance equation used by many authors represents an imperfect approximation to the more fundamental volume balance equation. (See Bear [1979], Eq. (A-24), where a term is dropped in the derivation of the mass balance from the volume balance.)

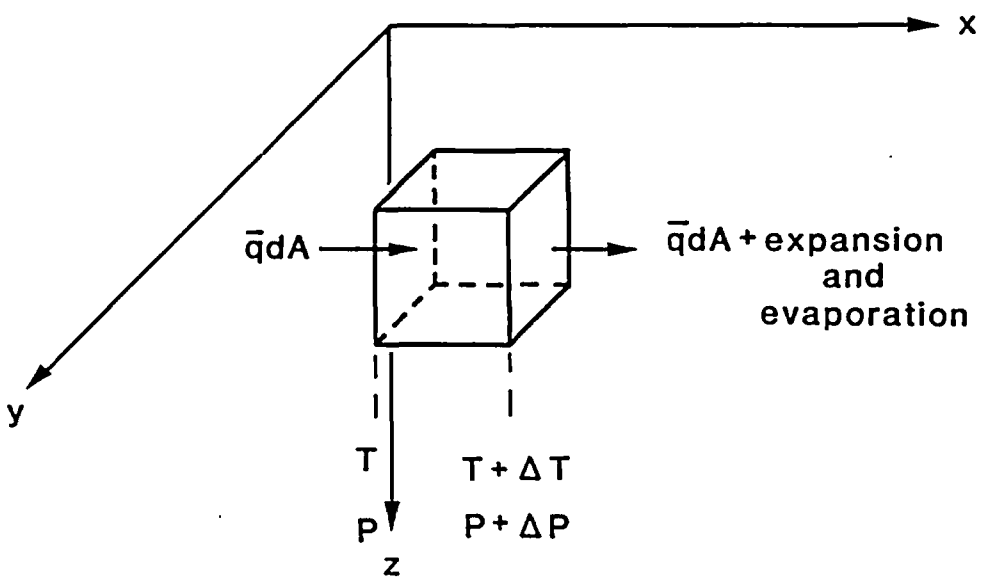

Figure 2-2. Elemental volume illustrating flow and gas volume balance under gradients of temperature and pressure.

The nature of the expansion or contraction of the gas passing through a fixed reference volume may be clarified by recalling the theory of ideal gases, which views gas molecules as perfectly elastic particles, each of which occupies the same volume of space. The volume of space maintained by collisions with other gas particles is directly proportional to the particle's kinetic energy, hence its temperature, and inversely proportional to the confining pressure. We can consider the "volume of the gas" in our cube at a given temperature to be equal to the volume occupied by a single gas molecule multiplied by the number of molecules. Thus, a change in gas volume reflects a change in the number of molecules or the volume occupied by each molecule as the gas moves under the influence of temperature and pressure gradients. The density (spacing of molecules) of the gas clearly changes with position, but not, in a steady-state system, with time.

Because of evaporation and condensation, neither the density nor the number of gas molecules in a parcel of rock gas remains constant as the gas moves. What does remain constant is the number of molecules of dry air (that is, all the components of rock gas other than water vapor) in the parcel. This allows us to write a volume balance equation relating the volume rate of flow per unit area, $\mathbf{q}$, to the volume occupied by the fluid containing a fixed number of moles of dry air, V. This equation, for steady state, is

$$\nabla \cdot \mathbf{q} = \mathbf{q} \cdot \frac{\nabla V}{V} \tag{2-3}$$

Now the volume V depends on position via temperature, T, and pressure P. Thus we need to develop an expression relating V to T and P. This relationship must take account of evaporation or condensation, as well as expansion or contraction of the gas.

To develop such an equation, we begin from the thought experiment shown in Figure 2-3. The figure depicts an air-filled chamber. The chamber is sealed against gas flow so that the amount of dry air in it remains constant. A sponge suspended in the chamber is connected by a capillary tube to a large reservoir of water that has a free surface at a lower, constant elevation. The pores of the sponge are thus partially filled with water, and evaporation or condensation in the sponge keeps the relative humidity very close to 100%. Both the temperature and the confining pressure of the chamber are externally controlled. The temperature is controlled by a heat source that has a variable-setting thermostat, and the pressure is regulated by a frictionless piston upon which weights may be placed.

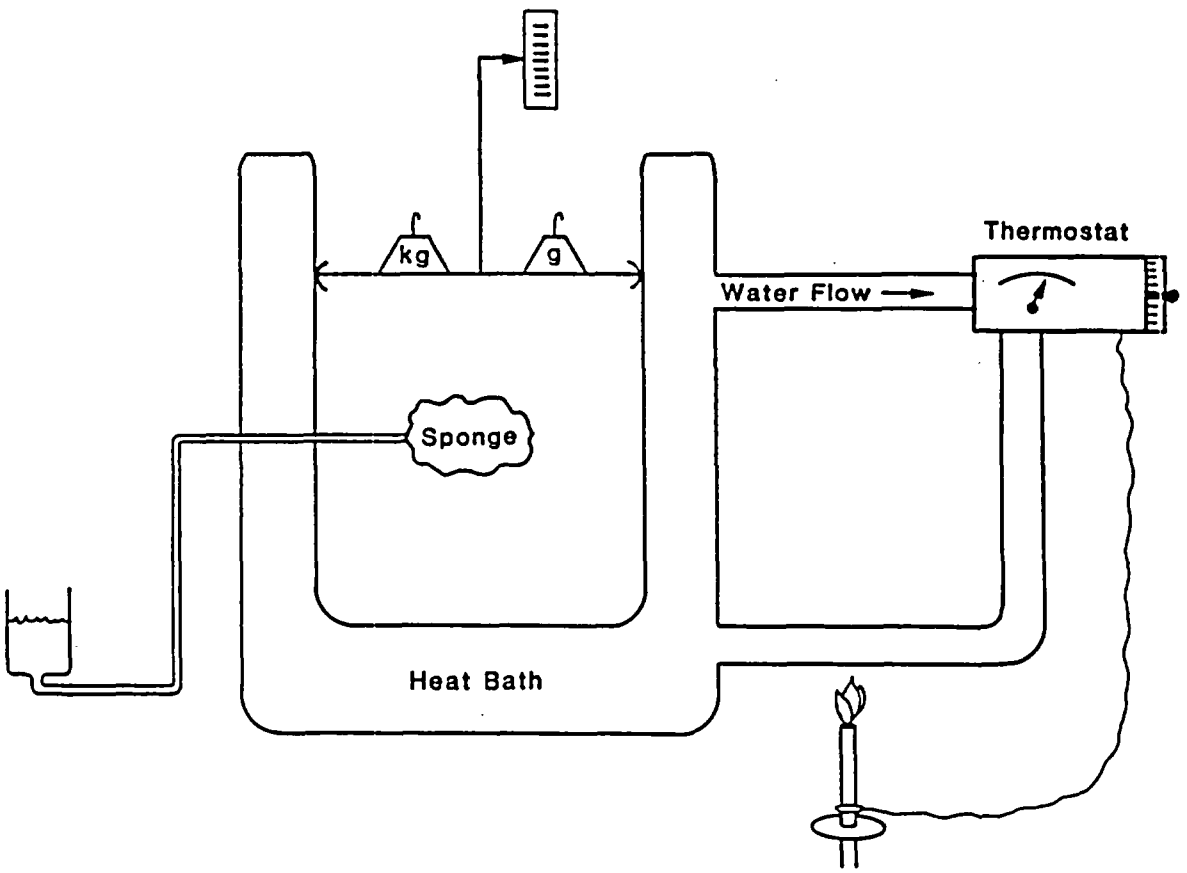

Figure 2-3. Illustration of thought experiment.

Let us examine the effect of increasing the temperature. When the temperature inside the chamber increases, the air becomes undersaturated with water vapor, allowing additional evaporation of water and changing both the number of moles of gas and the bulk composition of the gas in the chamber. The increase in the partial pressure of water vapor causes the piston to rise commensurately, without a change in the total pressure, which is a function only of the amount of weight on the piston.

Thus, the volume balance must include a pressure-gradient term and a source term that depends on the temperature gradient. Both of these terms can be evaluated by noting that from (2-1) and the ideal gas law

$$V = \frac{n_a RT}{P - P_v(T)} \tag{2-4}$$

where n_a is the number of moles of dry air in the parcel of air whose volume is V.

For expansion or contraction of the parcel of gas

$$\delta V = \frac{\partial}{\partial P}\left[\frac{n_a RT}{P - P_v(T)}\right]\delta P + \frac{\partial}{\partial T}\left[\frac{n_a RT}{P - P_v(T)}\right]\delta T \tag{2-5}$$

or

$$\delta V = -\frac{n_a RT}{[P - P_v(T)]^2}\delta P + \frac{n_a R}{P - P_v(T)}\delta T + \frac{n_a RT}{[P - P_v(T)]^2}\frac{dP_v}{dT}.\delta T \tag{2-6}$$

Dividing by unit vectors to get gradients in space gives

$$\nabla V = \left[\frac{n_a R}{P-P_v(T)} + \frac{n_a RT}{[P-P_v(T)]^2}\frac{dP_v}{dT}\right]\nabla T - \frac{n_a RT}{[P-P_v(T)]^2}\nabla P \tag{2-7}$$

Inserting (2-4) and (2-7) into (2-3) yields the steady-state volume balance equation:

$$\nabla \cdot \mathbf{q} - \mathbf{q} \cdot \left[\left[\frac{1}{T} + \frac{1}{P_a}\frac{dP_v}{dT}\right]\nabla T - \frac{1}{P_a}\nabla P\right] = 0 \tag{2-8}$$

where $P_a = P - P_v$.

For given boundary conditions, Equations (2-1), (2-2), and (2-8) can be solved for fields of density ρ, pressure P, and gas flux q. But gas flux, when expressed in terms of the pressure P as shown in Equation (2-2), is the difference of two nearly equal terms. As is well known, this can lead to numerical difficulties.

To calculate the flux directly from the pressure, very accurate pressures are needed. This requires a large numerical effort. Furthermore, it is difficult to determine what phenomena are small enough to be neglected. Terms that are small compared to ∇P may not be small compared to $\nabla P - g\rho\hat{z}$ [Davies, 1987].

These problems may be alleviated by canceling out analytically as large a portion of the large terms in (2-2) as possible. This approach has been developed by Huyakorn and Taylor [1976] for steady flows of incompressible saline water and by Frind [1982] and Huyakorn et al. [1987] for unsteady flows of the same fluid. These authors define a reference fluid density ρ_o and a reference pressure P_o and substitute for the pressure:

$$P = P_o + g\rho_o(z + h) \tag{2-9}$$

or

$$h = \frac{P - P_o}{g\rho_o} - z \tag{2-10}$$

The problem is then recast in terms of the new variable h. This variable is well-known in field studies of saline water, where it is called freshwater head [Lusczynski, 1961].

With the definition of (2-10), the Darcy flux can be written as:

$$\mathrm{q} = -\frac{g\rho_o k}{\mu}\left[\nabla h - \rho'\hat{z}\right] \tag{2-11}$$

where

$$\rho' = \frac{\rho}{\rho_o} - 1 = \frac{g}{RT}\left(h_v\Omega_v + h_a\Omega_a\right) - 1 \tag{2-12}$$

$$h_a = P_a/g\rho_o \tag{2-13a}$$

$$h_v = P_v/g\rho_o \tag{2-13b}$$

Substitution of Equation (2-9) into (2-8) yields:

$$\nabla \cdot \mathbf{q} - \mathbf{q} \cdot \left[\left[\frac{1}{T} + \frac{1}{h_a}\frac{dh_v}{dT}\right]\nabla T - \frac{1}{h_a}(\hat{z} + \nabla h)\right] = 0 \tag{2-14}$$

Now we insert (2-11) into (2-14):

$$\nabla \cdot \left[-\frac{g\rho_o k}{\mu}(\nabla h - \rho'\hat{z})\right] + \frac{g\rho_o k}{\mu}(\nabla h - \rho'\hat{z}) \cdot \left[\left[\frac{1}{T} + \frac{1}{h_a}\frac{dh_v}{dT}\right]\nabla T - \frac{1}{h_a}(\hat{z} + \nabla h)\right]$$

$$= 0 \tag{2-15}$$

Expanding and dividing by $-g\rho_o$ gives

$$\frac{k}{\mu}\nabla^2 h - \frac{k}{\mu}\frac{\partial \rho'}{\partial z} + \nabla\left[\frac{k}{\mu}\right] \cdot \nabla h - \rho'\frac{\partial}{\partial z}\left[\frac{k}{\mu}\right] + \frac{k}{\mu h_a}(\nabla h)^2 + \frac{k}{\mu h_a}(1-\rho')\frac{\partial h}{\partial z}$$

$$- \frac{k}{\mu h_a}\rho' - \frac{k}{\mu}\left[\frac{1}{T} + \frac{1}{h_a}\frac{dh_v}{dT}\right]\nabla T \cdot \nabla h + \frac{k}{\mu}\left[\frac{1}{T} + \frac{1}{h_a}\frac{dh_v}{dT}\right]\rho'\frac{\partial T}{\partial z} = 0 \tag{2-16}$$

Now we expand the spatial derivatives of ρ' and μ in terms of the variables T and h_a. Using the fact that $\partial\mu/\partial P = 0$ to a very good approximation, we can write

$$\nabla\frac{k}{\mu} = \frac{1}{\mu}\nabla k - \frac{k}{\mu^2}\frac{\partial \mu}{\partial T}\nabla T \tag{2-17a}$$

and

$$\frac{\partial \rho'}{\partial z} = \frac{\partial \rho'}{\partial T}\frac{\partial T}{\partial z} + \frac{\partial \rho'}{\partial h_a}\frac{\partial h_a}{\partial z} \tag{2-17b}$$

Inserting these expansions into (2-16) yields

$$\nabla^2 h - \left[\frac{\partial \rho'}{\partial T}\frac{\partial T}{\partial z} + \frac{\partial \rho'}{\partial h_a}\frac{\partial h_a}{\partial z}\right] + \frac{1}{k}\nabla k \cdot \nabla h - \frac{1}{\mu}\frac{\partial \mu}{\partial T}\nabla T \cdot \nabla h$$

$$- \frac{\rho'}{k}\frac{\partial k}{\partial z} + \frac{\rho'}{\mu}\frac{\partial \mu}{\partial T}\frac{\partial T}{\partial z} + \frac{1}{h_a}(\nabla h)^2 + \frac{1-\rho'}{h_a}\frac{\partial h}{\partial z} - \frac{\rho'}{h_a}$$

$$- \left[\frac{1}{T} + \frac{1}{h_a}\frac{dh_v}{dT}\right]\nabla T \cdot \nabla h + \left[\frac{1}{T} + \frac{1}{h_a}\frac{dh_v}{dT}\right]\rho'\frac{\partial T}{\partial z} = 0 \qquad (2\text{-}18)$$

Using (2-10), (2-12), and (2-13a), we expand the derivatives of ρ' in terms of the independent variables T and h_a:

$$\frac{\partial \rho'}{\partial T} = -\frac{g}{RT^2}(h_v\Omega_v + h_a\Omega_a) + \frac{g\Omega_v}{RT}\frac{dh_v}{dT} = -\left[\frac{1+\rho'}{T}\right] + \frac{g\Omega_v}{RT}\frac{dh_v}{dT} \qquad (2\text{-}19a)$$

$$\frac{\partial \rho'}{\partial h_a} = \frac{g\Omega_a}{RT} \qquad (2\text{-}19b)$$

$$\frac{\partial h_a}{\partial z} = \frac{\partial}{\partial z}\left[\frac{P_o}{g\rho_o} + z + h - h_v\right] = 1 + \frac{\partial h}{\partial z} - \frac{dh_v}{dT}\frac{\partial T}{\partial z} \qquad (2\text{-}19c)$$

Substituting (2-19a-c) into (2-18) and collecting terms yields:

$$\nabla^2 h + \frac{1}{h_a}(\nabla h)^2 + \frac{1}{k}\nabla k \cdot \nabla h - \left[\frac{1}{\mu}\frac{\partial \mu}{\partial T} + \frac{1}{T} + \frac{1}{h_a}\frac{dh_v}{dT}\right]\nabla T \cdot \nabla h$$

$$+ \left[\frac{1+\rho'}{T} + \frac{g(\Omega_a - \Omega_v)}{RT}\frac{dh_v}{dT} + \frac{\rho'}{\mu}\frac{\partial \mu}{\partial T} + \rho'\left[\frac{1}{T} + \frac{1}{h_a}\frac{dh_v}{dT}\right]\right]\frac{\partial T}{\partial z}$$

$$+ \left[-\frac{g\Omega_a}{RT} + \frac{1-\rho'}{h_a}\right]\frac{\partial h}{\partial z} - \frac{\rho'}{k}\frac{\partial k}{\partial z} - \frac{\rho'}{h_a} - \frac{g\Omega_a}{RT} = 0 \qquad (2\text{-}20)$$

or:

$$\nabla^2 h - m\nabla T \cdot \nabla h + \frac{1}{h_a}(\nabla h)^2 + \left[\frac{1}{T} + g\frac{\Omega_a - \Omega_v}{RT}\frac{dh_v}{dT} + \rho'\left(\frac{1}{T} + m\right)\right]\frac{\partial T}{\partial z}$$

$$+ \left[\frac{1-\rho'}{h_a} - \frac{g\Omega_a}{RT}\right]\frac{\partial h}{\partial z} - \frac{g\Omega_a}{RT} - \frac{\rho'}{h_a} + \frac{1}{k}\nabla k \cdot (\nabla h - \rho'\hat{z}) = 0 \qquad (2\text{-}21)$$

where

$$m = \frac{1}{\mu}\frac{d\mu}{dT} + \frac{1}{T} + \frac{1}{h_a}\frac{dh_v}{dT} \quad (2\text{-}22)$$

2.2.3 Discretization

For a homogeneous medium, the governing equation derived above can be taken directly and discretized in a node centered, finite difference form that can be solved for the value of h as a function of position. However, Yucca Mountain contains tilted layers of differing permeability. For such a system, it is more convenient to align the axes with the bedding. In this section, we present the discretized governing equation for the case of a two-dimensional, homogeneous system in which the permeability is constant. The additional terms needed to model zones of differing permeability will be added in Section 2.3.

A rotation of coordinates requires the modification of all terms which contain the term $\hat{z}$, or derivatives with respect to z. The following substitutions must be made:

$$\hat{z} = \hat{u} \sin\theta + \hat{v} \cos\theta \quad (2\text{-}23)$$

$$\frac{\partial T}{\partial z} = \frac{\partial T}{\partial u} \sin\theta + \frac{\partial T}{\partial v} \cos\theta \quad (2\text{-}24)$$

where $\hat{u}$ and $\hat{v}$ are the unit vectors in coordinates aligned with the gridding, and θ is the rotation angle between global coordinates (in which the z-axis points downward) and grid coordinates. The gradient operator is invariant with respect to a rotation of coordinates.

Equation (2-21) in finite difference form, for a node centered mesh of varying intervals [Bear and Verruijt, 1987], with the v-axis tilted θ degrees to $\hat{z}$, is

$$h_{i,j} = [A_i + B_i + C_j + E_j]^{-1} \left\{ [A_i h_{i+1,j} + B_i h_{i-1,j} + C_j h_{i,j+1} + E_j h_{i,j-1}] \right.$$

$$- \left[\frac{1}{\mu} \frac{d\mu}{dT} + \frac{1}{T} + \frac{1}{h_a} \frac{dh_v}{dT} \right] \left[\frac{(T_{i+1,j} - T_{i-1,j})(h_{i+1,j} - h_{i-1,j})}{(u_{i+1} - u_{i-1})^2} \right.$$

$$\left. + \frac{(T_{i,j+1} - T_{i,j-1})(h_{i,j+1} - h_{i,j-1})}{(v_{j+1} - v_{j-1})^2} \right]$$

$$+ \left[\frac{1}{T_{i,j}} \left[1 + g \left[\frac{\Omega_a - \Omega_v}{R} \right] \frac{dh_v}{dT} \right] + \left[\frac{1}{\mu} \frac{\partial \mu}{\partial T} + \frac{2}{T} + \frac{1}{h_a} \frac{dh_v}{dT} \right] \rho' \right]$$

$$\times \left[\frac{T_{i+1,j} - T_{i-1,j}}{u_{i+1} - u_{i-1}} \sin \theta + \frac{T_{i,j+1} - T_{i,j-1}}{v_{j+1} - v_{j-1}} \cos \theta \right]$$

$$\left. - \frac{g\Omega_a}{RT_{i,j}} - \frac{\rho'}{h_a} \right\} \qquad (2\text{-}25)$$

where i and j are indices giving the location of a node in the u,v plane and

$$A_i = 2/[(u_{i+1} - u_i)(u_{i+1} - u_{i-1})] \qquad (2\text{-}26a)$$

$$B_i = 2/[(u_i - u_{i-1})(u_{i+1} - u_{i-1})] \qquad (2\text{-}26b)$$

$$C_j = 2/[(v_{j+1} - v_j)(v_{j+1} - v_{j-1})] \qquad (2\text{-}26c)$$

$$E_j = 2/[(v_j - v_{j-1})(v_{j+1} - v_{j-1})] \qquad (2\text{-}26d)$$

Note that h_v, h_a, and ρ' are always evaluated at node i, j.

The flux equation (2-11) in finite difference form is:

$$\mathbf{q} = - \frac{-g\rho_o k}{\mu} \left[\left[\frac{h_{i+1,j} - h_{i-1,j}}{u_{i+1} - u_{i-1}} \hat{\mathbf{u}} + \frac{h_{i,j+1} - h_{i,j-1}}{v_{i+1} - v_{i-1}} \hat{\mathbf{v}} \right] \right.$$

$$\left. - \rho' (\hat{\mathbf{u}} \sin \theta + \hat{\mathbf{v}} \cos \theta) \right] \qquad (2\text{-}27)$$

2.3 Zone interfaces

Because the governing equation (2-21) is so complex, the usual numerical treatment of heterogeneous permeability [Bear and Verruijt, 1987] becomes inconvenient. It is easier to evaluate the ∇k term independently rather than fold it into the second derivative term as normally done.

We require that zone interfaces follow the lines separating grid blocks. We will begin by supposing that the permeability changes smoothly over a thin transition layer of thickness d, as shown in Figure 2-4, and then will take the limit where the thickness of the interface layer tends to zero.

Using (2-11), the ∇k term in (2-21) may be written as

$$- \frac{\mu}{g\rho_o k} \nabla(\ln k) \cdot \mathbf{q} \tag{2-28}$$

When the governing equation is discretized, this term must be replaced by its average over a grid block. This average is

$$- \frac{\mu}{g\rho_o D} \lim_{d \to 0} \int_{-d/2}^{d/2} \frac{1}{k} \left[\mathbf{q} \cdot \nabla \ln k \right] dy \tag{2-29}$$

where for simplicity we have assumed that the node spacing in the direction normal to the boundary, D, is the same on both sides of the boundary. The integration variable y is a coordinate normal to the zone boundary.

Expression (2-28) can be rewritten in terms of the component of flux normal to the boundary $q_\perp$. We substitute

$$\mathbf{q} \cdot \nabla \ln k = q_\perp \frac{d}{dy} \ln k \tag{2-30}$$

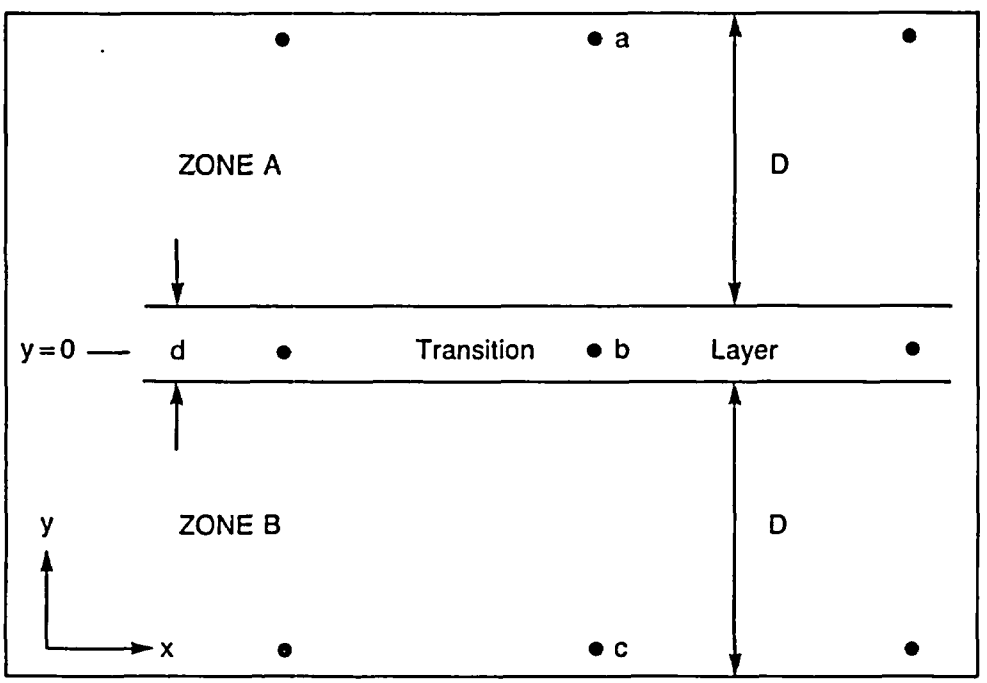

Figure 2-4. Treatment of interfaces between permeability zones.

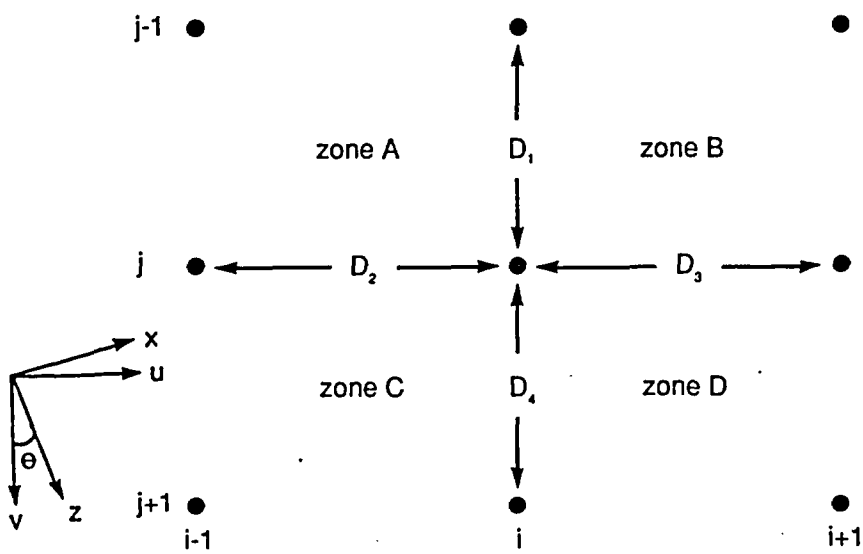

Figure 2-5. Schematic of subzones and node spacing along a zone interface.

into (2-29) and use the integral

$$\int_{-d/2}^{d/2} \frac{1}{k}\left[\frac{d}{dy}\ln k\right] dy = \int_{-d/2}^{d/2} \frac{1}{k^2}\frac{dk}{dy}\, dy = \int_{k_A}^{k_B} \frac{dk}{k^2} = k_B^{-1} - k_A^{-1} \tag{2-31}$$

to obtain

$$-\lim_{d\to 0} \frac{\mu q_\perp}{g\rho_o D} \int_{-d/2}^{d/2} \frac{1}{k}\left[\frac{d}{dy}\ln k\right] dy = \frac{\mu q_\perp}{g\rho_o D}\left[k_A^{-1} - k_B^{-1}\right] \tag{2-32}$$

The problem that remains is to find a value for $q_\perp$. Care must be taken to avoid instabilities when evaluating this quantity. We proceed as follows. Noting that Nodes a and c are equidistant from the boundary, the formula giving the equivalent permeability in the direction normal to the interface is [Freeze and Cherry, 1979]:

$$k_{avg} = \frac{2}{\frac{1}{k_A} + \frac{1}{k_B}} \tag{2-33}$$

and (2-11) can be used to express the flow across the boundary as

$$q_\perp = \frac{-2g\rho_o}{\mu_b\left[\frac{1}{k_A} + \frac{1}{k_B}\right]}\left[\frac{1}{2D}(h_a - h_c) - \rho'\hat{z}\cdot\hat{n}\right] \tag{2-34}$$

where the subscripts a, b, and c refer to quantities evaluated at the nodes so labeled in Figure 2-4 and where $\hat{n}$ is a unit vector normal to the transition layer pointing in the positive direction of grid coordinates.

Substituting (2-34) into (2-32) yields a final expression for the additional term to be inserted in the finite-difference version of (2-21).

$$-\frac{\mu}{g\rho_o D}\lim_{d\to 0}\int_{-d/2}^{d/2}\left[\mathbf{q}\cdot\nabla\ln k\right] dy = \frac{k_A - k_B}{k_A + k_B}\frac{1}{D^2}(h_a - h_c - 2\rho'_b D\hat{z}\cdot\hat{n}) \tag{2-35}$$

where Zone A and Node *a* are at more positive values of the coordinate normal to the interface.

At nodes lying on straight sections of zone interfaces, as illustrated in Fig. 2-4, the term given by (2-35) can be added directly into the governing equation. At nodes where an interface makes a right angle, or three zones adjoin, the situation is somewhat more complicated. At such nodes, terms like (2-35) are calculated for each segment of interface connected to the node, multiplied by half the node spacing in the direction of that segment, and added into the equation. Expression (2-35) then is replaced by

$$\left\{ \frac{2}{D_2+D_3} \left[D_2 \frac{k_C-k_A}{D_4k_A+D_1k_C} + D_3 \frac{k_D-k_B}{D_4k_B+D_1k_D} \right] \left[\frac{h_{i,j+1} - h_{i,j-1}}{D_1 + D_4} + \rho' \cos\theta \right] \right.$$

$$\left. + \frac{2}{D_1+D_4} \left[D_1 \frac{k_B-k_A}{D_3k_A+D_2k_B} + D_4 \frac{k_D-k_C}{D_3k_C+D_2k_D} \right] \left[\frac{h_{i+1,j} - h_{i-1,i}}{D_2 + D_3} - \rho' \sin\theta \right] \right\} \qquad (2\text{-}36)$$

here k_n is the intrinsic permeability of zone n, D_n is the node spacing between pairs of nodes and θ is the angle of rotation of the coordinate axes, all as illustrated on Figure 2-5.

2.4 Boundary conditions

The gas-flow model allows boundary conditions of two types: fixed-head (Dirichlet) or no-flow (Neumann). For fixed-head boundaries representing the ground surface, the model can calculate heads corresponding to the variation of atmospheric pressure with elevation. No-flow boundaries may represent physical obstacles to flow such as low-permeability rocks, flow divides such as would be found beneath a linear valley between two mountains, or locations remote from the area of interest. Implementation of the no-flow boundary is complicated by the ρ' term in the flux equation; this is discussed in Section 2.4.2.

2.4.1 Atmospheric boundary condition

Along the surface of the mountain, P and h are functions of elevation, temperature, and relative humidity. We assume that temperature varies linearly with elevation and that the mole fraction of water vapor in the air is uniform. The boundary condition is then derived from the ideal gas law for moist air, modified to include a term for relative humidity, and the laws of hydrostatics. Wind effects, which may be important, are neglected.

For any fluid in hydrostatic equilibrium:

$$dP = \rho g dz \tag{2-37}$$

The assumptions that temperature is linear in altitude and the mole fraction of water vapor, r, is uniform are now applied. (This implies a slight variation of relative humidity with elevation, even at uniform temperature.) The density of air is then:

$$\rho = \frac{P}{R(T_a + \lambda z)} \left[r\Omega_v + (1-r)\,\Omega_a \right] \tag{2-38}$$

where T_a is the air temperature at elevation z=0 and the empirical coefficient λ is referred to as the "lapse rate."

Substitution of (2-38) into (2-37) yields

$$\frac{dP}{P} = \frac{\Gamma dz}{T_a + \lambda z} \tag{2-39}$$

where

$$\Gamma = \frac{g}{R} \left[r\Omega_v + (1-r)\,\Omega_a \right] \tag{2-40}$$

Equation (2-39) integrates to

$$\ln P = \text{const.} + \frac{\Gamma}{\lambda} \ln (T_a + \lambda z) \tag{2-41}$$

With a bit of manipulation, the constant can be evaluated to give

$$P = P_{atm}\left[1 + \frac{\lambda z}{T_a}\right]^{\Gamma/\lambda} \tag{2-42}$$

where P_{atm} is the atmospheric pressure at z=0.

Unfortunately, the formula (2-42) becomes numerically intractable in the limit $\lambda \to 0$. This problem is overcome by using the expansion

$$(1+x)^{s/x} = e^s\left[1 - \frac{s}{2}x + \left[\frac{s}{3} + \frac{s^2}{8}\right]x^2 - \ldots\right] \tag{2-43}$$

The model uses the first three terms of this expansion instead of evaluating (2-42) directly when $\Gamma/\lambda > 10$ and $\lambda z/T_a < 0.001$. Note that inserting (2-43) into (2-42) yields the expansion in powers of λ

$$P = P_{atm}\, e^{\Gamma z/T_a}\left[1 - \frac{\Gamma\lambda z^2}{2T_a^2} + \ldots\right] \tag{2-44}$$

in which the leading term corresponds to the well-known exponential law for atmospheric pressure at constant temperature.

The head is computed from the atmospheric pressure (2-42) or (2-44) by Eq. (2-10). For convenience, Γ is expressed in terms of the atmospheric relative humidity at z=0, η, by

$$\Gamma = \frac{g}{R}\left[\Omega_a + \eta\,\frac{P_v(T_a)}{P_{atm}}\,(\Omega_v - \Omega_a)\right] \tag{2-45}$$

2.4.2 No-flow boundary condition

From Equation (2-11), the condition for no flow across an arbitrary plane is

$$q_\perp = \mathbf{q}\cdot\hat{\mathbf{n}} = -\,g\rho_o\,\frac{k}{\mu}\left[\frac{\partial h}{\partial n} - \rho'\hat{\mathbf{z}}\cdot\hat{\mathbf{n}}\right] = 0 \tag{2-46}$$

where $\hat{\mathbf{n}}$ is a unit vector normal to the boundary.

We now must implement this condition at a boundary. Figure 2-6 illustrates the nodes at a boundary parallel to the u axis of a grid coordinate system. Equation (2-46) in discretized form is:

$$q_{\perp} = - \frac{g\rho_o k}{\mu} \left\{ \frac{1}{2D} \left[h_{i,j+1} - h_{i,j-1} \right] - \rho' \cos \theta \right\} \qquad (2\text{-}47)$$

The no-flow boundary is specified at the jth row of nodes on Figure 2-6. However, one cannot proceed directly to solve either governing Equation (2-21) or Equation (2-47) for $h_{i,j}$ because this would require a value for $h_{i,j+1}$, a node which lies outside of the flow field.

To overcome this difficulty, we calculate values of $h_{i,j-1}$ and $h_{i,j}$ using the normal governing equation (2-21), and solve Equation (2-47) for the fictitious j+1 node, thereby reducing the equation to one unknown. This method is an extension of the reflection technique commonly used to handle no-flow boundaries when solving Laplace's Equation [Wang and Anderson, 1982].

The boundary condition thus becomes an equation for the head of the fictitious node i, j+1

$$h_{i,j+1} = h_{i,j-1} + 2D\rho' \cos \theta \qquad (2\text{-}48)$$

Values of space-dependent parameters are those assigned to the i, j node.

Note that for a no-flow boundary parallel to the v axis, the condition uses the difference along the v axis and the sine of θ. If θ is equal to zero (no rotation), the no-flow condition across vertical boundaries reduces to simple reflection:

$$h_{i+1,j} = h_{i-1,j} \qquad (2\text{-}49)$$

2.5 Implementation

The steady-state gas flow model, which had initially been developed in spreadsheet form, has now been converted to Fortran code. The Fortran version of TGIF is written in

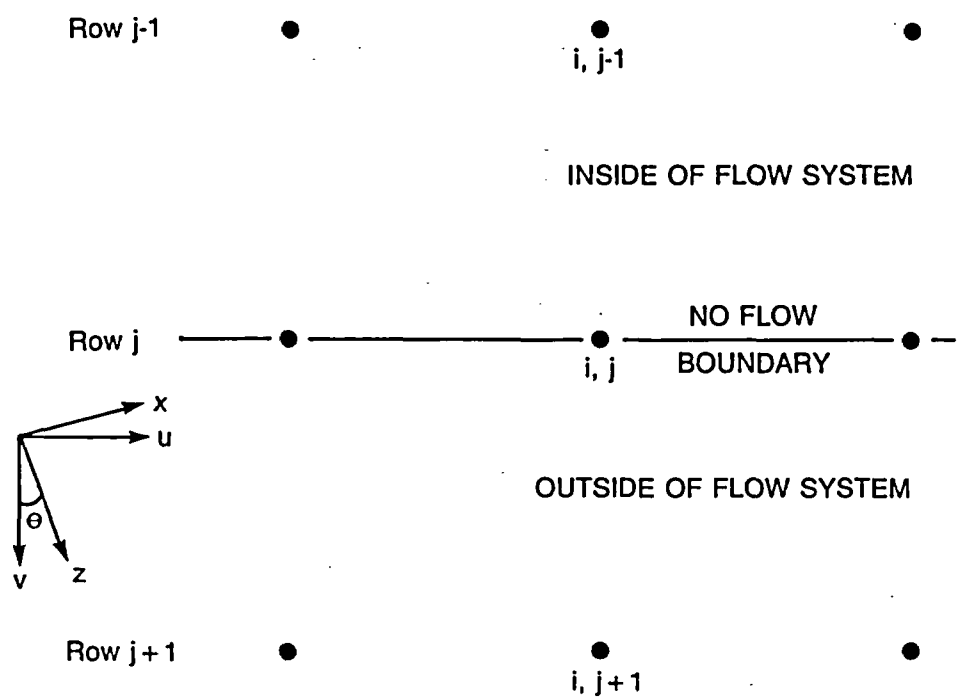

Figure 2-6. Nodes defining a no-flow boundary parallel to an axis in a rotated system. The j+1 row of nodes is fictitious and lies outside the flow system.

Ryan-McFarland Fortran (for micro-computers) and is fully compatible with standard Fortran 77. The program can thus be used on mainframe computers with only trivial modifications to account for specific hardware configurations.

A preprocessor module with descriptions and prompts for the user allows one to rapidly construct input data files of any size. This program is called USER. Both the preprocessor and the main program detect input formatting errors and give error messages on a limited basis. Figures 2-7 and 2-8 illustrate schematically the main components of the preprocessor and the gas-flow model.

The program has the following features:

1. Physical parameters and reference values can be set by the user, or default values (for Yucca Mountain) can be used.

2. The model can handle a variety of finite-difference mesh types. Meshes can contain either squares or rectangular blocks of a single size, or combinations of squares and rectangles of varying size. This allows the user to make the mesh finer in particular areas. The preprocessor can generate grids and calculate the elevations and locations of nodes automatically. It requires only basic information on the spacing between node rows and columns, and the position of a single input "anchor" node.

3. Multi-layered geologic systems can be modeled. The layers can be horizontal, vertical, tilted, and truncated. The model can also handle lenses of geologic media.

4. The user can specify a rotation of coordinates (to aid in the modeling of tilted geologic layers). The mesh is then constructed parallel to the layering and the model calculates the true elevations of the nodes.

5. The user can choose among three types of boundary conditions: a fixed value of the "fresh water head," an atmospheric boundary for which the model will calculate a fixed value of head that depends upon elevation, and no flow.

6. The user can set two parameters which control convergence toward the solution of the flow problem: the successive over-relaxation (SOR) parameter and the convergence criterion.

7. The model can generate a full complement of output, written to both the screen and a file. The user has the option to suppress much of the output.

Non-suppressible output includes the program title, the physical parameters and reference values used, information on the grid geometry, convergence parameters, and tables listing for each node the residual head value, and the components of flux. The residual and head can be printed repeatedly after a specified number of iterations has occurred, or just once after the last iteration.

Suppressible output includes the echoing of arrays of input data, such as temperature, intrinsic permeability, fresh water head, and type of node.

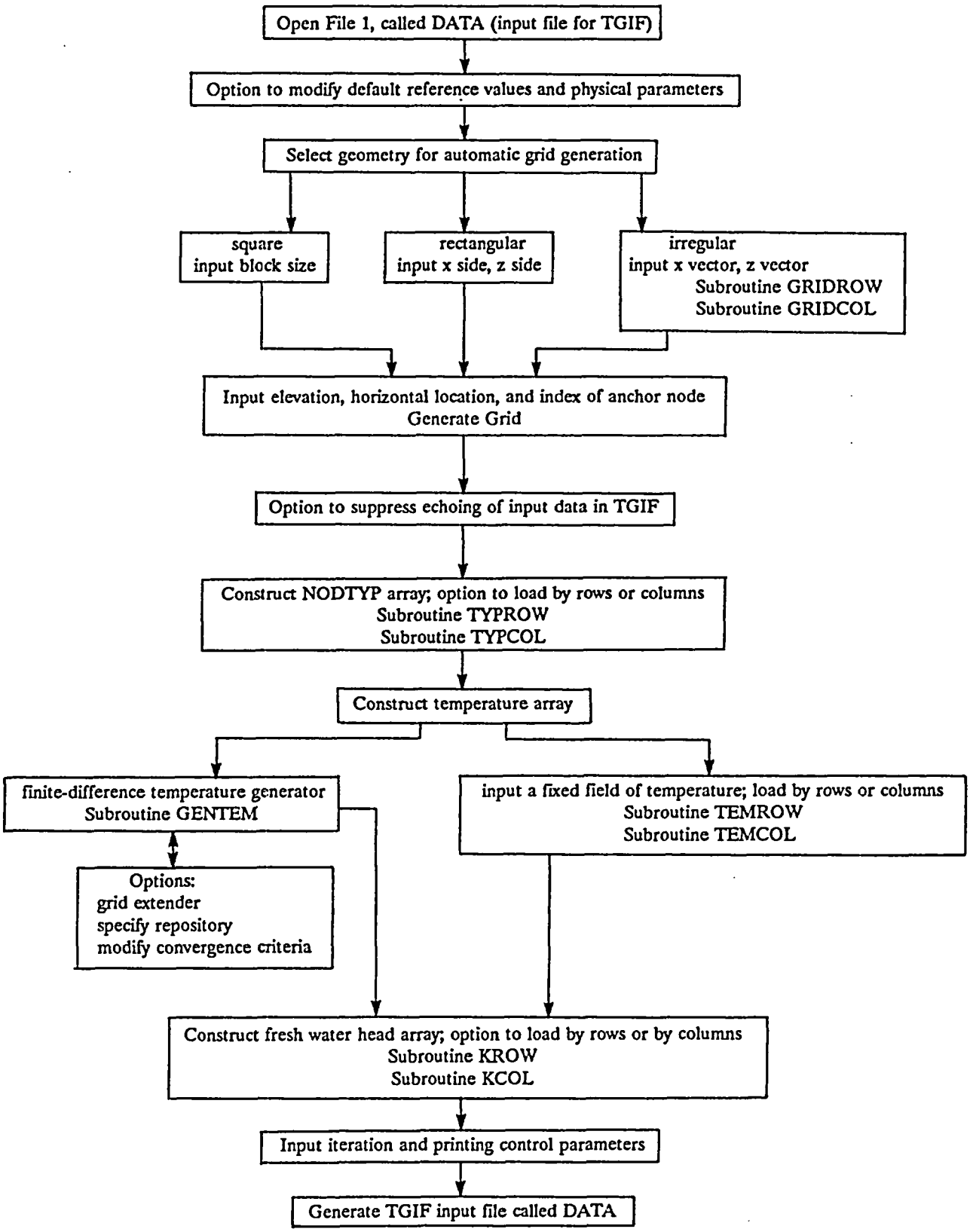

Figure 2-7. Flow chart of USER, the preprocessor to the TGIF gas-flow model.

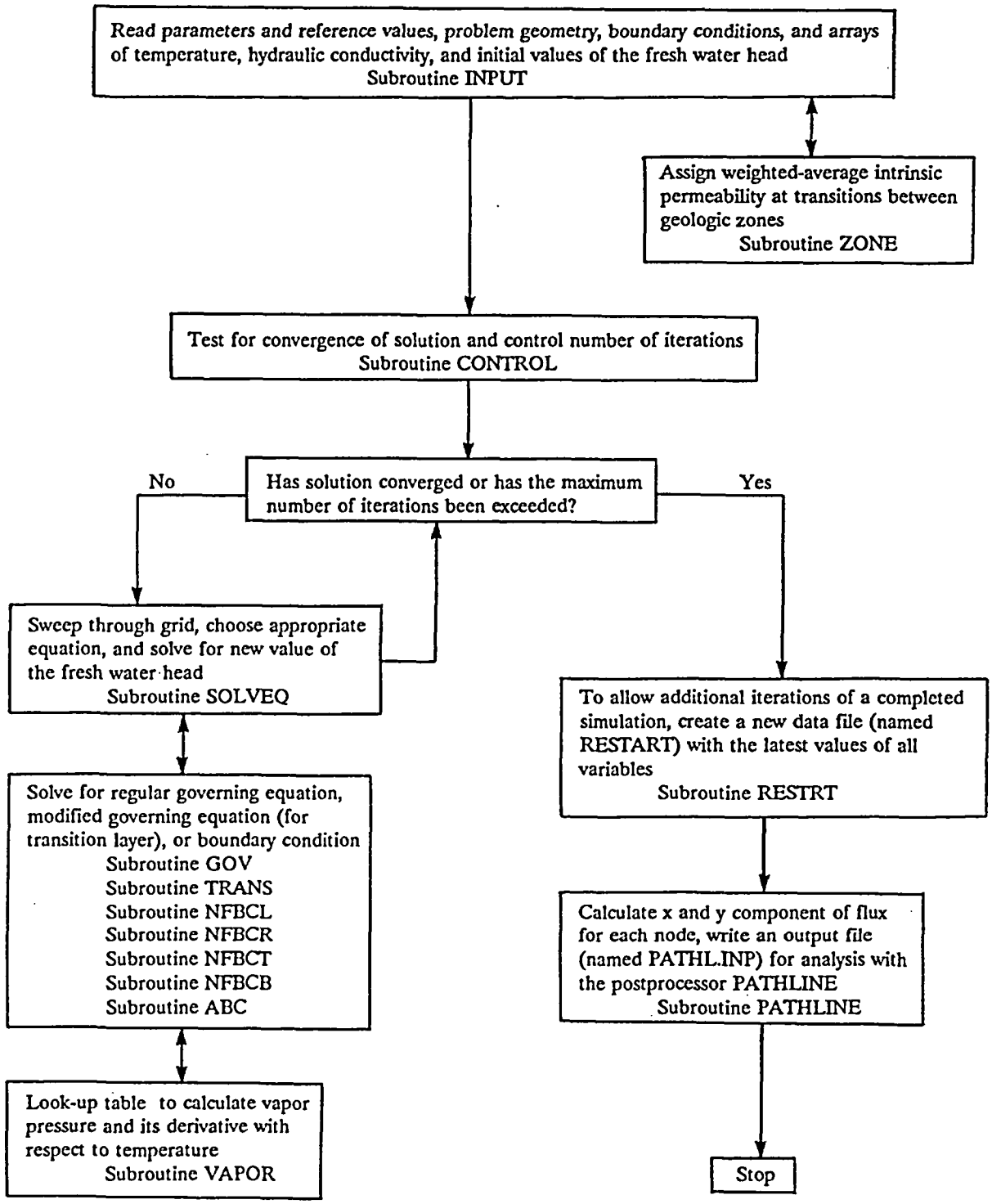

Figure 2-8. Flow chart of the TGIF gas-flow model.

CHAPTER 3
HEAT TRANSFER MODEL

Solution of the freshwater head in TGIF requires that the temperature at every node in the grid be specified in the input data. The preprocessor, USER, simplifies the construction of input data sets for TGIF. The temperature model is a part of the preprocessor which can calculate the temperature field from specified boundary conditions.

The distribution of temperature beneath the ground surface depends upon a number of factors, including the geothermal gradient, which varies regionally and is a function of tectonic setting, topography, climatic factors affecting variation in surface temperature, and local sources of heat such as radioactive rock and thermal springs. Currently, the temperature model accounts only for topography, surface temperature, the geothermal gradient, and heat generated by a radioactive waste repository.

3.1 Assumptions

The temperature model is based on the following assumptions:

- Heat transfer is dominated by conduction. Temperature inside the mountain is independent of convective flow, relative humidity, and pressure.
- The relative humidity is near saturation and remains constant during the duration of the simulation.
- The rock has uniform and isotropic thermal conductivity.
- The geothermal gradient at depth is uniform and vertical to the elevation datum.
- Surface temperature depends only on elevation.

The assumption that conduction is the dominant mechanism of heat tranfer may not be realistic, especially when the mountain is heated by a repository. However, in steady-state simulations in which heat sources are absent or are assigned a fixed temperature (rather than a fixed heat output), the magnitude of the heat-transfer coefficient does not affect the results. In such cases, a conduction model should give a rough approximation to the true temperatures even when convection is an important heat-transfer mechanism. In the

future, we intend to add convection terms to the heat-transfer model so that transient problems and problems involving specified fluxes can be simulated.

3.2 Solution method

The temperature field is solved under steady-state conditions using Laplace's equation for heat flow:

$$\nabla^2 T = 0 \qquad (3\text{-}1)$$

The finite difference method is used to calculate the temperature at grid nodes. To speed convergence, Gauss-Seidel iteration and successive overrelaxation are used.

3.3 Boundary conditions

The assignment of boundary conditions in the temperature model is a four-step process. The first step is to specify air temperatures along the ground surface. The second step is to use the surface temperature and an assumed geothermal gradient to assign temperatures along the bottom of the simulated region. In both cases, it is assumed that ambient conditions apply, that is, repository heating is not yet considered. The third step is to place a boundary condition on the heat flux across the left and right sides of the simulated region -- if the grid is not tilted, then the flux will be zero because the geothermal gradient is assumed vertical. Finally, if the simulation includes a repository, temperature is specified at nodes along the repository horizon.

3.3.1 Atmospheric boundary condition

The temperature of air is dependent on elevation. In the model, temperatures along the atmospheric boundary are assigned based on elevation and a lapse rate (usually assigned a value of 0.65 K per 100 m [Donn, 1975]). A reference value of air temperature, corresponding to a point outside the mountain at the reference elevation (where z = 0), must be specified.

3.3.2 Lower boundary condition

The assignment of a lower boundary condition requires special measures. In reality, there is no lower boundary. However, by assuming that the boundary is at an infinite distance and that the geothermal gradient at the boundary is uniform and vertical, the problem is greatly simplified.

Under the ideal conditions of flat topography, uniform surface temperature, and no local sources of heat, isotherms are horizontal, as shown in Figure 3-1a. However, this is generally not the case. Topographic relief causes isotherms to be curved near the earth's surface. An exception to this rule would occur if the lapse rate (variation in air temperature with altitude) is equal to the geothermal gradient. This rare case is illustrated in Figure 3-1b.

Curvature of isotherms resulting from small-scale relief damps out rapidly with depth, usually within a few meters or tens of meters, as illustrated in Figure 3-1c. However, large scale variations in topography can cause curvature of isotherms to extend to considerable depths, as shown in Figure 3-1d. When simulating such a case, it is important that the lower boundary be placed far enough below the surface, or other sources of heat such as a repository, to make the assumption of a boundary at infinity valid.

The temperature model has been designed with the above precaution in mind. To improve the calculation of the temperature field, the modeler has the option of extending the finite difference grid in the vertical direction. This option extends the grid in the temperature model, but not in the flow model. It adds ten rows of blocks with vertical spacing that increases approximately exponentially.

The assignment of the lower boundary condition is the same whether or not the extension option is used. A point on the ground surface must be specified and temperatures along the lower boundary are calculated from

$$T_{LB}(u) = T_s + G\left[z_{LB}(u) - z_s\right] \qquad (3\text{-}2)$$

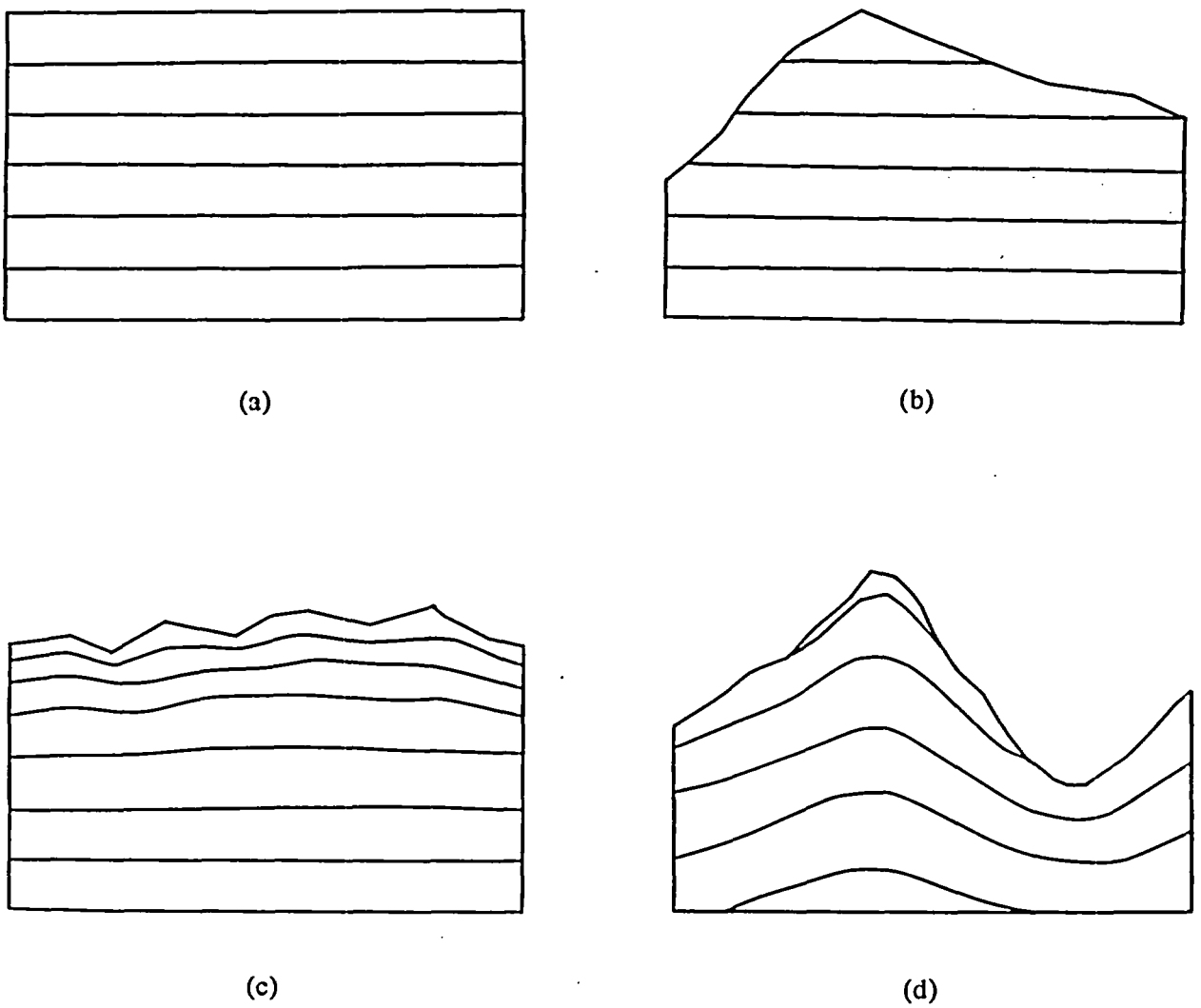

Figure 3-1. Temperature contours showing the relationship among the geothermal gradient, lapse rate, and topography: (a) flat topography and uniform surface temperature; (b) irregular topography and lapse rate equal to the geothermal gradient; (c) geothermal gradient exceeding the lapse rate with small topographic relief, curvature of isotherms damps out rapidly with increasing depth; (d) geothermal gradient exceeding the lapse rate with large topographic relief, curvature of isotherms extend to considerable depth.

where: $T_{LB}(u)$ = temperature at the lower boundary at the base of column u

T_s = air temperature at elevation z_s

G = geothermal gradient; the model uses the geothermal gradient of 2 K per 100 m measured by Montazer et al. [1985].

$z_{LB}(u)$ = elevation at the lower boundary at the base of column u

z_s = specified elevation on ground surface

It is best if z_s is close to the mean elevation of the ground surface in the simulation. This minimizes the influence of non-horizontal isotherms near the ground surface on assignment of lower boundary temperatures.

3.3.3 Vertical flux condition along sides

The model assumes that heat flux along the left and right boundaries of the simulated region is always vertical. When grid coordinates are parallel to global coordinates, this condition can easily be met by using the method of reflection to define no-flow conditions. However, a modification of reflection is necessary to constrain the flux to be vertical when the side boundaries are tilted from vertical.

The usual way to apply the technique of reflection is to set the node on the boundary equal to an appropriate interior node, such that a no-flow condition is generated between the two nodes. (If adjacent nodes are used, the no-flow condition will be at 1/2 the nodal spacing; if two nodes separated by third node are used, the condition will lie on the middle node. In the temperature model we use half spacing.) If reflection is used along all nodes along the side of a grid, a no-flow boundary is generated and flow is constrained to be parallel to the boundary. If the grid boundary is vertical, then only vertical flow can occur.

If, however, the grid boundary is tilted from vertical, simple reflection will result in a tilted no-flow boundary. Because the system has an imposed flow of heat upward from the

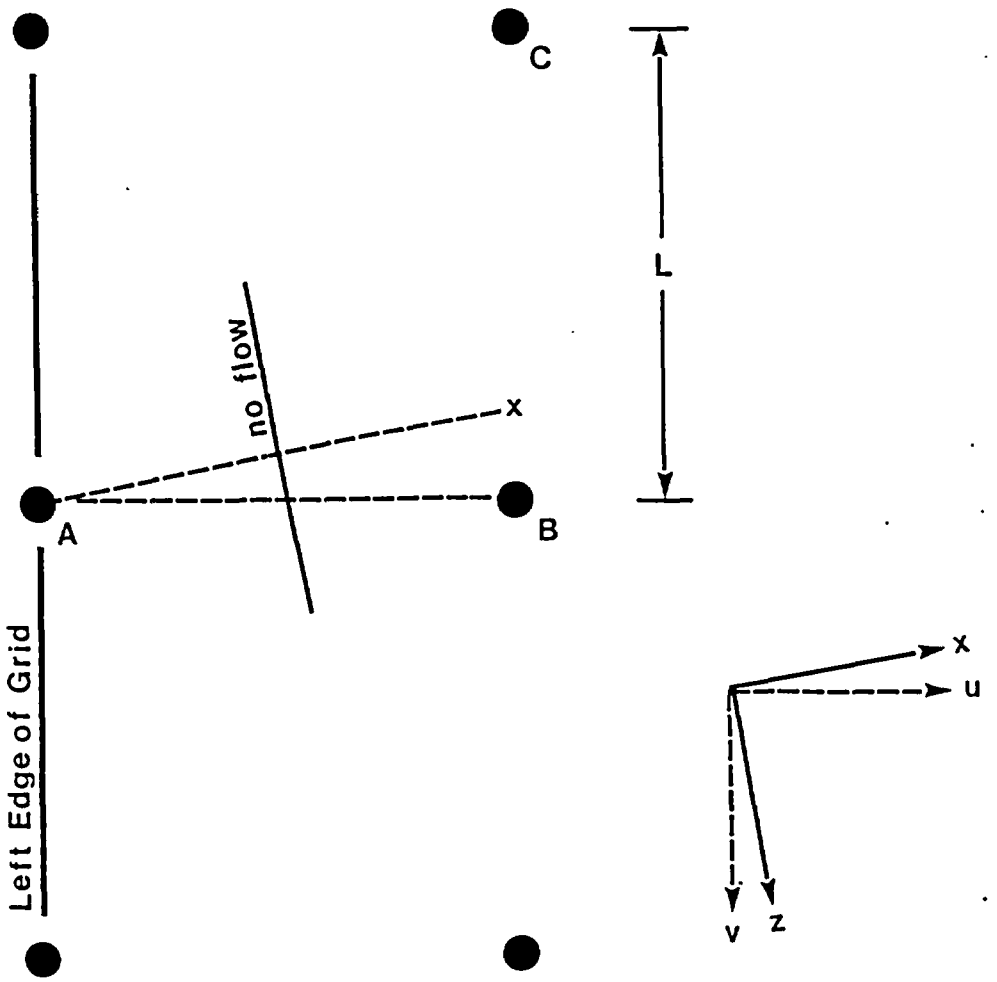

Figure 3-2. Illustration of vertical flux boundary condition for a tilted grid.

bottom, this will have the effect of imposing a horizontal heat flux at the boundaries. For there to be a horizontal component of heat flux, there must also be a horizontal component of the temperature gradient. Artifically imposed horizontal temperature gradients, even if small, are very undesirable because horizontal temperature differences drive convection cells in the gas flow model.

It is therefore preferable to impose a boundary condition that forces the heat flux at the boundary to be exactly vertical. To do this, the reflection technique must be modified so that the reflection occurs across a vertical plane. The temperature of the node on the grid boundary must be set to the temperature at a point that falls between two nodes in the next column or row. The point can be found by extending a horizontal line from a node on the boundary to where it intersects the plane of the adjacent column. The temperature at this point can be found by linear interpolation between the two nodes in the adjacent column.

Figure 3-2 illustrates how the technique would be applied at a left-side boundary that has been tilted 12 degrees from vertical in the clockwise direction. The temperature at point A is set equal to the temperature at point x, which is found by linear interpolation of temperature between B and C. Note that when the condition is applied along a line of nodes a discontinuous no flow boundary results. The degree of jaggedness is dependent on the node spacing.

The temperature T_x at point x is found from:

$$T_x = T_B - \frac{u_B - u_A}{v_B - v_C} \left[T_B - T_C\right] \tan \alpha \qquad (3\text{-}3)$$

where the angle of tilt α is xAB and u and v are untilted coordinates respectively.

3.3.4 Repository

To simulate a repository, uniform temperatures may be assigned to nodes located along the repository. These temperatures may represent cooldown at certain times in the repository's history. Mathematically, the repository is treated as a fixed-temperature boundary, although the "boundary" is located in the interior of the simulation region.

The repository can be located at any orientation anywhere within the interior of the grid. The only limitations are that the repository form a straight line and that it does not intersect a grid boundary. To generate a repository, the temperature model requires only a temperature and the coordinates of the endpoints of the repository.

CHAPTER 4
PARTICLE TRACKER

The TGIF model calculates the volumetric flux, also known as the Darcy velocity. The actual velocity of a particle of gas that does not interact with the liquid or solid phases, or seepage velocity, V, is related to the flux q by

$$V = \frac{q}{n_d} \tag{4-1}$$

where n_d is the drained porosity (gas-filled porosity) of the system. The total drained porosity, rather than an effective porosity, can be used because

- in a partially saturated medium, small non-flowing pores tend to fill with water rather than gas, and
- rapid diffusion in the gas phase promotes mixing between flowing fractures and pores and any dead-end pores that may be filled with gas (see Appendix B).

The seepage velocity at each point can thus be calculated directly from the flux computed by TGIF. But to go from the velocity vector at each point to the trajectory of a single particle over time requires further computation. This work is done by a particle-tracking post-processor, called PATHLINE. The path lines computed by PATHLINE show where contaminants in the gas would migrate. By following particles along these lines, PATHLINE also calculates travel times.

4.1 Theory

The basic concept of particle tracking is to trace specified particles through the flow field [Shafer, 1987]. In the simplest approach, the tracks of the particles are obtained by adding linear steps. This is done by computing the velocities of the particles at initial positions, then moving them to new locations by multiplying each particle's velocity by a finite time step to obtain the changes in position over that time interval. By repeating this process, a time-series of particle positions is obtained, describing the particle's path through the prescribed flow field as a function of time. Because this method ignores the changes in velocity during a time step, it is not very accurate when implemented numerically.

We use a more accurate method of particle tracking, which was originally developed by Pollock [1988; 1989]. This method involves explicit integration of velocity within each grid block. The method is based on the approximation that each directional velocity component varies linearly within a grid cell in its own coordinate directions. Because Pollock obtains his cell face velocities from the "block-centered finite-difference" method of solving the flow equation, Pollock's program cannot be used to compute path lines for other numerical methods, such as the lattice-centered finite difference computation we used in our model. Thus we modified Pollock's method slightly and wrote our own computer program.

A two-dimensional velocity field specified at grid nodes is first obtained by running the TGIF program (Chapter 2). To apply Pollock's method, it is necessary to calculate a velocity on each cell face. Figure 4-1(a) and (b) shows how the cell face velocities (denoted a, b, c, d) are calculated. By averaging the nodal velocities (denoted 1, 2, 3, 4), the cell face velocities are obtained as

$$V_x^a = \frac{1}{2}(V_x^1 + V_x^4) \tag{4-2a}$$

$$V_x^b = \frac{1}{2}(V_x^1 + V_x^2) \tag{4-2b}$$

$$V_x^c = \frac{1}{2}(V_x^2 + V_x^3) \tag{4-2c}$$

$$V_x^d = \frac{1}{2}(V_x^3 + V_x^4) \tag{4-2d}$$

$$V_y^a = \frac{1}{2}(V_y^1 + V_y^4) \tag{4-2e}$$

$$V_y^b = \frac{1}{2}(V_y^1 + V_y^2) \tag{4-2f}$$

$$V_y^c = \frac{1}{2}(V_y^2 + V_y^3) \tag{4-2g}$$

$$V_y^d = \frac{1}{2}(V_y^3 + V_y^4) \tag{4-2h}$$

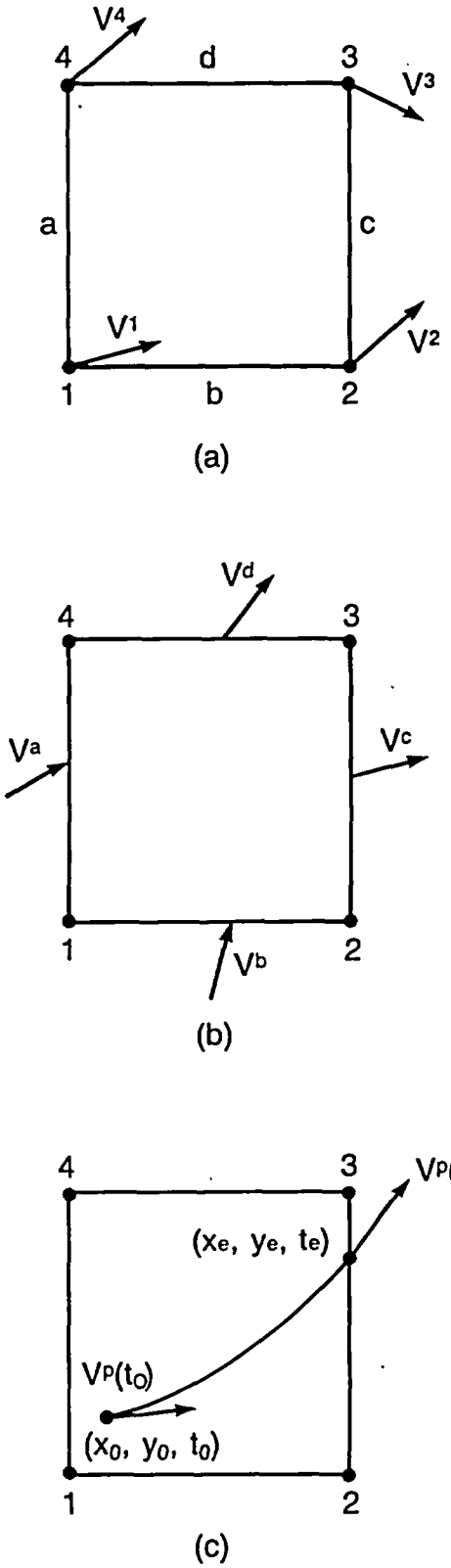

Figure 4-1. Schematic illustration of particle tracking technique, (a) velocities at nodes, (b) velocities at the cell faces, (c) calculated particle path through the cell.

Once the cell face velocities are known, the velocities can be linearly interpolated to obtain the following expressions for the two components of the velocity V^p of a particle located at point x, y (refer to Figure 4-1c)

$$V_x^p = A_x (x-x_1) + V_x^a \tag{4-3a}$$

$$V_y^p = A_y (y-y_1) + V_y^b \tag{4-3b}$$

where A_x and A_y are the components of the velocity gradients of the cell, defined in terms of Δx, the distance between points 1 and 2 or points 4 and 3, and Δy, the distance between points 1 and 4 or points 2 and 3, as

$$A_x = (V_x^c - V_x^a) / \Delta x \tag{4-4a}$$

$$A_y = (V_y^d - V_y^b) / \Delta y \tag{4-4b}$$

There are two main advantages of using simple linear interpolation. First, it produces a continuous velocity vector field within each cell that identically satisfies Laplace's equation, which is a fair approximation to our governing equation. Second, it allows one to obtain the analytical solution of path lines within a cell. By using analytical solutions within each cell, the accuracy of the numerical solution is significantly improved and the computation time greatly reduced.

Knowing the cell face velocities and the particle velocities, the cell face through which the particle exits the grid block can be identified. The travel time can be calculated analytically [Pollock, 1989] as the smaller of

$$\Delta t_x = \frac{1}{A_x} \ln \left[\frac{V_x^c}{V_x^p}\right] \tag{4-5a}$$

or

$$\Delta t_y = \frac{1}{A_y} \ln \left[\frac{V_y^d}{V_y^p}\right] \tag{4-5b}$$

The particle locations at any given time within the time step can be expressed analytically as

$$x_p(t) = x_1 + \frac{1}{A_x}\left[V_x^p(t_o)\exp\left(A_x\,\Delta t\right) - V_x^a\right] \tag{4-6a}$$

$$y_p(t) = y_1 + \frac{1}{A_y}\left[V_y^p(t_o)\exp\left(A_y\Delta t\right) - V_y^a\right] \tag{4-6b}$$

where V_x^p and V_y^p are calculated from (4-3).

If we insert equation (4-5b) or (4-5a) into Equations (4-6a) and (4-6b), the exit coordinates of the particle are

$$x_p(t_e) = x_1 + \frac{1}{A_x}\left[V_x^p\,(t_0)\exp\left(A_x\Delta t_e\right) - V_x^a\right] \tag{4-7a}$$

$$y_p(t_e) = y_1 + \frac{1}{A_y}\left[V_y^p\,(t_0)\exp\left(A_y\Delta t_e\right) - V_y^b\right] \tag{4-7b}$$

4.2 Travel times

For a particle of gas that does not interact with the liquid and solid phases, the time for a particle to travel some distance (say, from the repository to the surface) is easily computed by adding together the travel times for each grid block through which the particle passes. The travel times for individual grid blocks are given by (4-5).

Carbon-14 in the form of $^{14}CO_2$ can interact with the aqueous and solid phases. There is no significant isotopic fractionation between phases and, with the gas and liquid in intimate contact in the pores, isotopic equilibrium is rapidly achieved. If there is no interaction with the solid phase,[1] the speed of carbon-14 transport is reduced by a factor B which is proportional to the concentration ratio of carbon in the liquid and gas phases to gaseous carbon [Ross, 1988]:

[1]This assumption does not seem to hold in all geological systems; see Striegl [1988]. It is adopted here for conservatism.

$$B = 1 + \frac{[n_T - n_D]}{n_D} \left[\frac{C_T^*}{C_T}\right] \quad (4\text{-}8)$$

where

n_T = total porosity for each hydrologic unit

n_D = drained porosity for each hydrologic unit

C_T^* = concentration of carbon ion in the liquid phase at equilibrium

C_T = concentration of carbon ion in the gas phase at equilibrium

The factor B is known as the retardation factor.

4.2.1 Chemical modeling approach

Solution of Equation (4-8) requires that the concentration of dissolved inorganic carbon and the partial pressure of carbon dioxide as functions of temperature be known. A relationship between pressure and temperature in a non-reacting gas phase can easily be developed; however, the temperature dependence of aqueous chemical reactions is complex. We used the reaction path model PHREEQE to model the geochemical system, concentrating on reactions of carbonate species. This model simulated expected equilibria with mineral phases and predicted changes in speciation with temperature. This work is summarized here; it is described in more detail in a forthcoming Pacific Northwest Laboratory report

Perhaps the most fundamental property of the geochemical system that had to be defined is the identity of the mineral phases that govern water chemistry. Because secondary calcite is found in the unsaturated zone in significant quantities and an exogenous source of calcium can be identified in the calcitic sands that mantle much of Yucca Mountain, it is reasonable to conclude that the carbonate system buffers the water chemistry. If calcium is present in only minor amounts, the weathering of tuffaceous

silicate minerals may be the source, and more complex reactions would be needed to predict chemical reactions. Precipitation of solid phases may alter total dissolved carbon concentrations and thereby influence carbon-14 concentrations in all phases.

The conceptual model of the geochemical system adopted here has three principal features:

- Sufficient calcium carbonate is present in the unsaturated zone to dominate the aqueous chemistry and buffer the pH of the water.
- A relatively minor amount of calcium is derived from silicate weathering reactions. As a first approximation, it can be assumed that calcium concentrations are the result of equilibration with calcium carbonate.
- Fractionation plays a negligible role in removing carbon-14 from the gas phase, and concentrations of carbon-14 are proportional to those of carbon-12.

The relative concentrations of carbonate species in liquid and gas phases at equilibrium were used to calculate a retardation factor for carbon-14 transport in the gas phase. The concentration calculated by the above procedure reflects a variety of chemical interactions, including ion exchange, mineral precipitation, and sorption. However, the retardation factor itself reflects only the distribution of carbon-14 between the gaseous and dissolved phases.

4.2.2 Inputs to chemical calculations

Each simulation used the same aqueous chemical concentrations (with the exception of calcium concentrations), gas partial pressure, and temperature. Values of pH are required input to PHREEQE, but were unavailable and had to be solved for iteratively as discussed below. Initial guesses of pH were based on analyses of unsaturated zone water analyzed at Rainier Mesa (near Yucca Mountain) that ranged from 7 to 8.

Few chemical data exist for unsaturated-zone water at Yucca Mountain. The data that have been published are ranges of concentrations reported by Yang et al. [1988]. All samples came from the Paintbrush nonwelded unit. Water samples were obtained by pressure squeezing. A range of calcium concentrations from 27 to 127 mg/L was obtained.

In this report it is assumed that these data are representative of the generalized unsaturated zone water quality.

Yang et al. [1985] measured the partial pressure of carbon dioxide in gas samples collected at intervals to a depth of 1200 feet in Yucca Mountain. A characteristic value of 0.11 % was used in all simulations.

Values of porosity of the three hydrologic units defined in the unsaturated zone at Yucca Mountain are given in Montazer and Wilson [1985]. The data are based on laboratory analyses of core samples.

Table 4-1

Porosity Values

Unit	Total Porosity	Drained Porosity
Tiva Canyon	0.12	0.04
Paintbrush	0.46	0.18
Topopah Spring	0.14	0.05

4.2.3 Results of chemical modeling

Three sets of initial conditions were modeled. A hypothetical range of dissolved carbon concentrations and pH was calculated, using the endpoints of a range of calcium concentrations that nearly spans the measurements of Yang et al. [1988] (110 and 30 mg/L). A third set of simulations changed calcium and bicarbonate concentration to achieve a charge balance.

Concentrations calculated in each set of simulations were used to compute retardation factors. Retardation factors calculated by the charge-balance method were roughly in the center of the range calculated by the other method, so they were adopted for use in travel-time calculations.

Although the calcium concentration predicted by the charge balance is in the lower range of observed calcium concentrations, retardation factors calculated for each

hydrogeologic unit using these values are approximately in the middle of the range of retardation factors defined by calculations using extreme calcium concentrations. These values were therefore adopted for further use. Figure 4-2 shows the retardation factors in each hydrogeologic unit as calculated by the charge balance method.

To simplify calculations, linear approximations of the curves shown in Figure 4-2 were used to calculate travel times. These were generated by linear regression, and are given in Table 4-2.

Table 4-2

Equation for Retardation Factor (T given in °C)

Unit	Retardation Equation	r^2
Tiva Canyon welded	$B(T) = 92.7 - (0.948)T$	0.9985
Paintbrush non-welded	$B(T) = 71.66 - (0.7305)T$	0.9985
Topopah Springs welded	$B(T) = 84.89 - (0.8673)T$	0.9985

4.3 Numerical implementation of particle tracking

The particle tracking method and calculation of travel times described above have been implemented in the program PATHLINE. Figure 4-3 shows a flow chart of the particle tracking program.

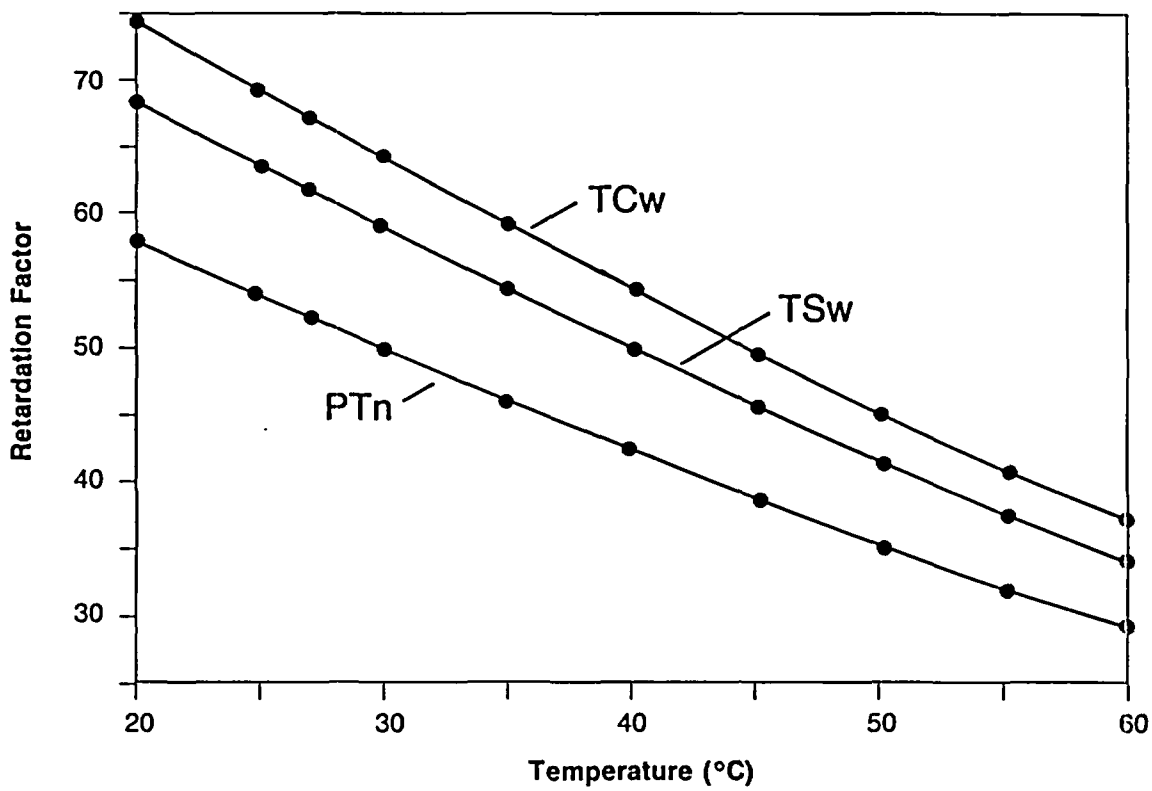

Figure 4-2. Retardation factor as a function of temperature for all units.

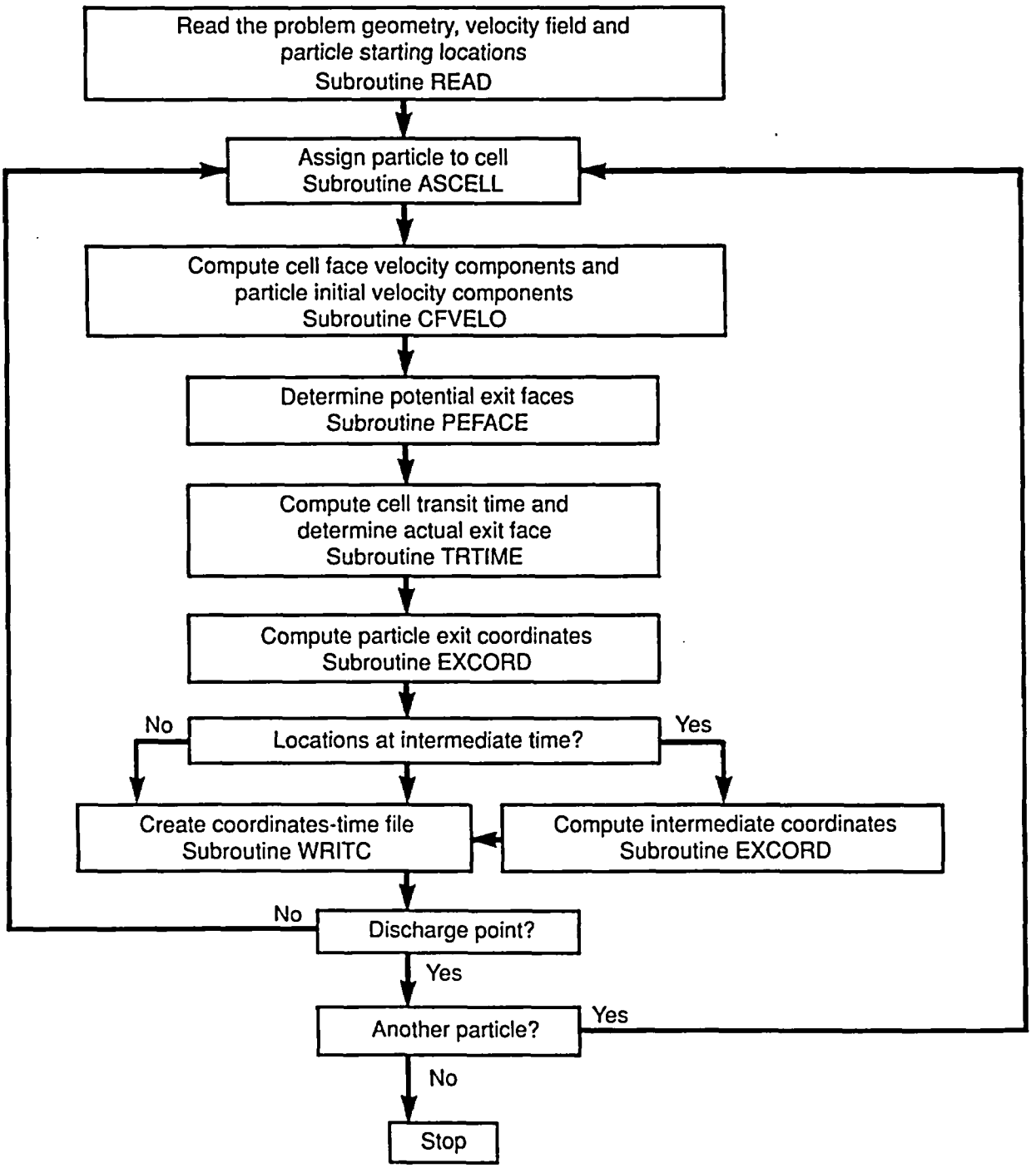

Figure 4-3. Flow chart of PATHLINE particle tracking program.

CHAPTER 5
SENSITIVITY STUDIES

5.1 General

This section describes a systematic sensitivity study that was designed to test the flexibility, convergence, and accuracy of the TGIF model when used to simulate gas flow under Yucca Mountain. Values of three important inputs to the model were systematically varied to form a matrix of 80 runs. The matrix consisted of five values of permeability contrast between a bedded tuff layer and surrounding welded units (in all cases, bulk permeabilities were used to represent the combined effect of both fractures and matrix permeability), four temperature profiles representing different stages of repository cooldown, and four finite-difference grids.

5.2 Physical properties

Gas flow was simulated in a two-dimensional vertical section that cuts across the southern portion of Yucca Mountain within the area where a nuclear waste repository might be located. A schematic of the simulated section is shown in Figure 5-1. The section is different from any of those used in the analyses presented in Chapter 6; a relatively narrow portion of the mountain was selected to economize on computer storage and execution time.

The mountain contains a number of hydrostratigraphic subdivisions of the Paintbrush Tuff Formation. These layers dip approximately six degrees to the east and differ in permeability. The most important hydrostratigraphic feature of the modeled section is a thin, nonwelded tuff layer which includes all or part of several stratigraphic subdivisions of the Paintbrush Tuff [Scott and Bonk, 1984]. This unit, the Paintbrush nonwelded unit, is sparsely fractured and thus is thought to have a relatively lower permeability. It lies between two thick, welded, densely fractured, and relatively permeable units, the Tiva Canyon welded unit (above) and the Topopah Spring welded unit (below).

A permeability of 10^{-11} m^2 [Montazer et al., 1985] was used for both the Tiva Canyon unit and the Topopah Spring unit, while permeabilities of 10^{-14}, 10^{-13}, 10^{-12}, 10^{-11},

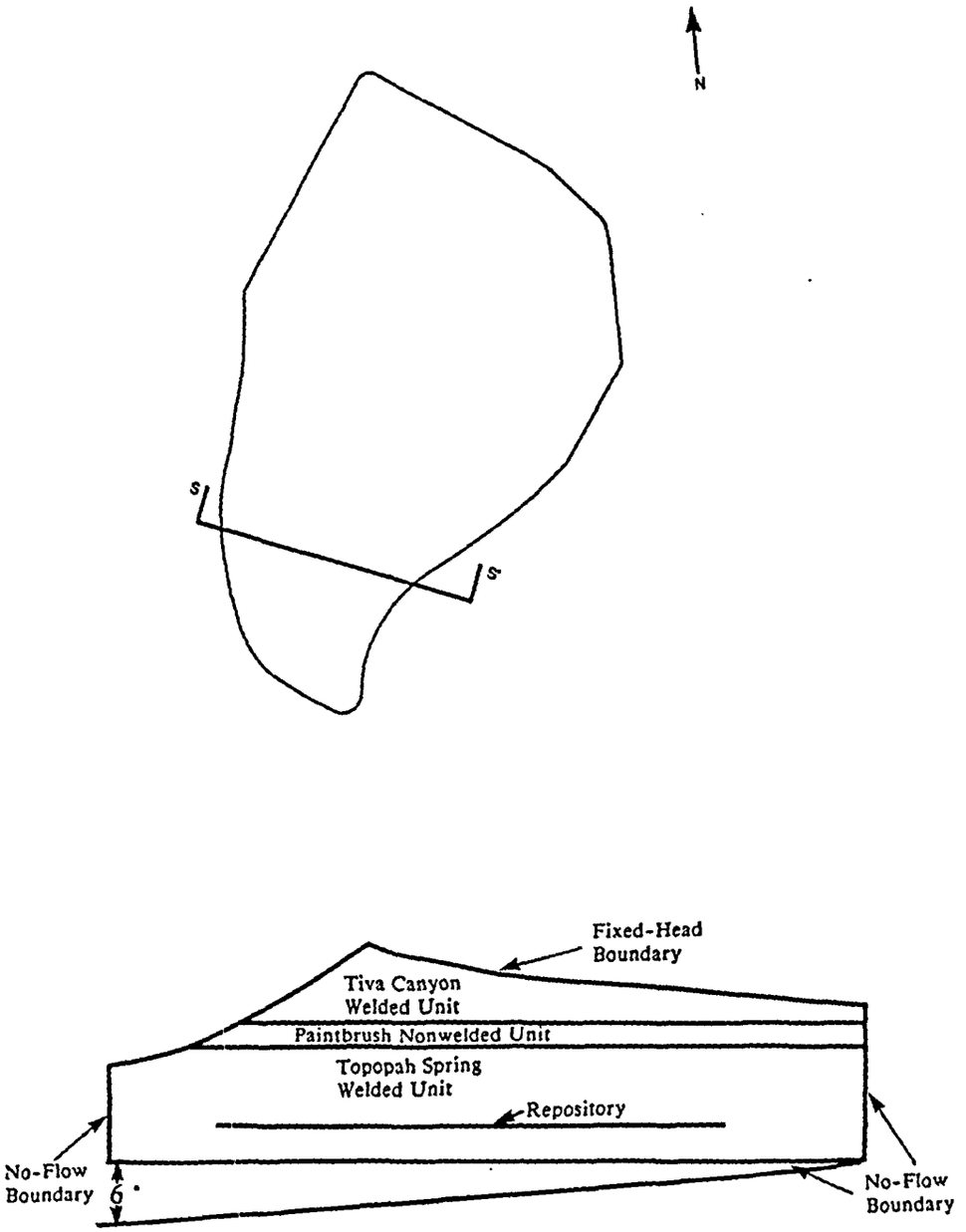

Figure 5-1. Geometry of cross section used in the gas flow simulation.

and 10^{-10} m^2 were used for the nonwelded unit in the simulations. Since the path lines depend only on the degree of the permeability contrast between the two kinds of tuff and not on the absolute magnitude of the permeability, travel times for other values of welded-tuff permeability can be obtained from travel times reported here by dividing by the ratio of the permeabilities.

The simulation region is surrounded by two types of boundary conditions (Figure 5-1),

- the mountain's atmospheric contact along its surface, and
- no-flow conditions along the base and sides.

The no-flow boundary assigned at the base of the simulated region represents the top of the low-permeability tuffaceous beds of the Calico Hills unit, which would impede downward gas flow. The boundary to the west is located in the trough of Solitario Wash, which is a natural flow divide. The third no-flow boundary is located far enough to the east to have little effect on flow near the repository. Numbers shown in Figure 5-1 represent starting locations of particle tracks.

The four temperature fields were calculated using prescribed temperatures at the repository and all boundaries. Along the atmospheric boundary, a uniform temperature (independent of elevation) was assumed. Temperatures were prescribed at the base and sides of the cross-section, following an assumed geothermal gradient. These boundary conditions are less realistic than those described in Chapter 3 and used in Chapter 6, but any distortion they induce in the temperature field should not affect the value of the results as a sensitivity study.

5.3 Simulations

A matrix of 80 runs was constructed by varying three important aspects of the simulation (see Figure 5-2). These were:

- the temperature of the repository and surrounding rock,
- the permeability of the Paintbrush nonwelded unit, which is the middle layer in the simulation, and

- nodal density used to represent the Paintbrush nonwelded unit and also the entire simulation.

The entire three-dimensional matrix of simulations is shown schematically in Figure 5-2, where k is the intrinsic permeability of the Paintbrush nonwelded unit and k' is the intrinsic permeability of the surrounding Tiva Canyon and Topopah Spring welded units.

Five different permeability contrasts were used in the simulations. The Paintbrush nonwelded unit was assumed to be 10 times more permeable and also 1, 10, 100, and 1000 times less permeable than the surrounding welded units, which were assigned a permeability of 10^{-11} m^2. The objective was to test the model over the range of contrasts that was found by Montazer et al. [1985].

As depicted in Figure 5-2, the matrix of simulations included four different assumed temperature profiles. The ambient condition represents the current condition of an average geothermal gradient of 2.0 K per 100 m. In the remaining three situations, the subsurface was assumed to have been heated by the nuclear waste in the repository, raising temperatures at the repository by approximately 3, 14, and 30 K over ambient conditions. This range in temperatures was used to examine how gas flow may be affected by temperature.

We did not try to assess at what times these temperatures would occur. Published calculations of repository temperature employ different assumptions about gas flow from those made here, or else ignore the phenomenon entirely. Any assignment of a specific time to a calculated set of gas fluxes would therefore rest on inconsistent assumptions.

To examine the sensitivity of the model to mesh density, the number of rows used in the simulation, particularly in and around the middle layer, was varied. Four different meshes were employed.

The first mesh contained 13 rows and 45 columns of blocks. The middle layer contained two rows of rectangular blocks that measured 20 m (vertical length) by 40 m. The remaining blocks were squares with sides of 40 m.

In the second mesh, the number of rows and columns was increased to 24 and 90. This resulted in a mesh consisting entirely of square blocks that measured 20 m on a side. As in the first case, two rows of blocks were used to represent the Paintbrush nonwelded unit.

The third mesh was a modification of the second mesh. The number of rows of blocks used to represent the Paintbrush nonwelded unit was increased from two to four by decreasing by half the row spacing in the middle unit. The Paintbrush nonwelded unit was thus represented by 4 rows of rectangular blocks that measured 10 m by 20 m. The rest of the domain retained square blocks.

The fourth mesh was also a modification of the second mesh. The number of rows of blocks was increased to 30 by halving the row spacing not only in the Paintbrush nonwelded unit, but also four blocks into the surrounding units. This mesh, shown in Figure 5-3, contained 12 rows of blocks measuring 10 m by 20 m, 4 of which represented the Paintbrush nonwelded unit. The rest of the mesh retained square blocks.

5.4 Results

The results of the 80 simulations demonstrate that the predicted pattern of flow is highly dependent on the temperature and permeability contrast. Selected output from the model, in the form of particle tracks, illustrates the major trends.

5.4.1 The effect of temperature

The temperature of the repository affects both the velocity of gas particles leaving the repository and the direction of the path lines. Figure 5-4 shows the path lines for simulations in a uniform medium (no permeability contrast) at ambient conditions (approximately 300 K at the repository) and repository temperatures of 314 K and 330 K.

As the repository temperature increases, the vertical velocity component for gas particles exiting from the repository also increases. Increasing temperature thus decreases path-line curvature and length and also decreases transit times for particles traveling from

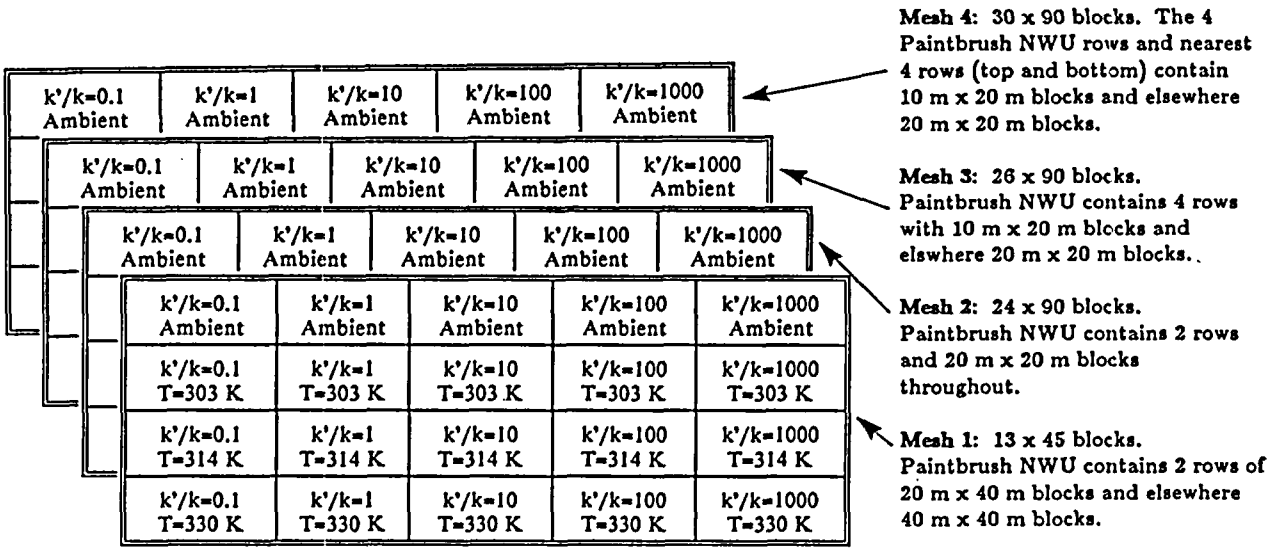

Figure 5-2. Matrix of simulation cases.

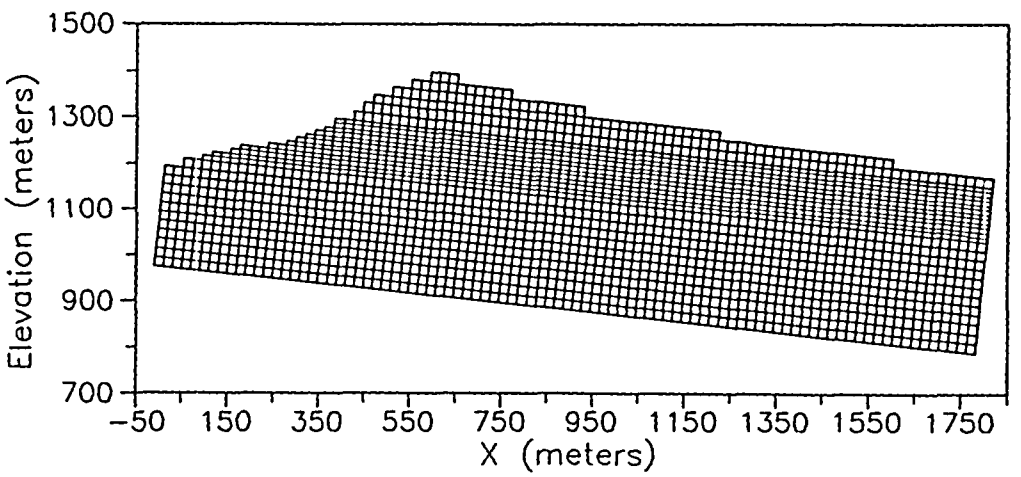

Figure 5-3. Two-dimensional finite difference grid (30 x 90 blocks).

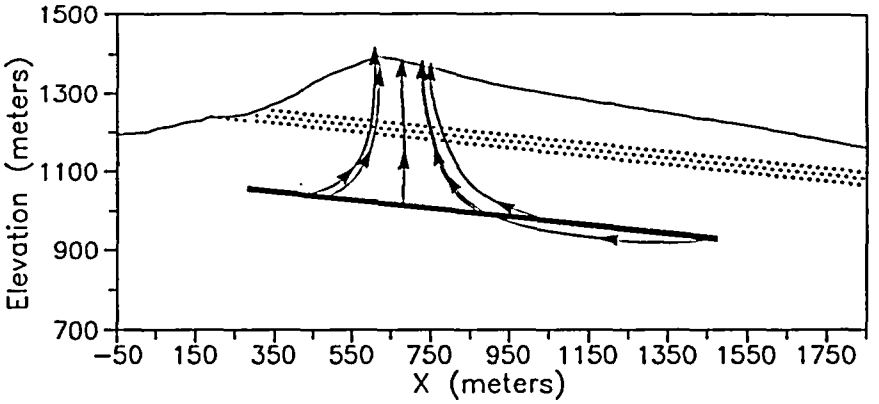

(a)

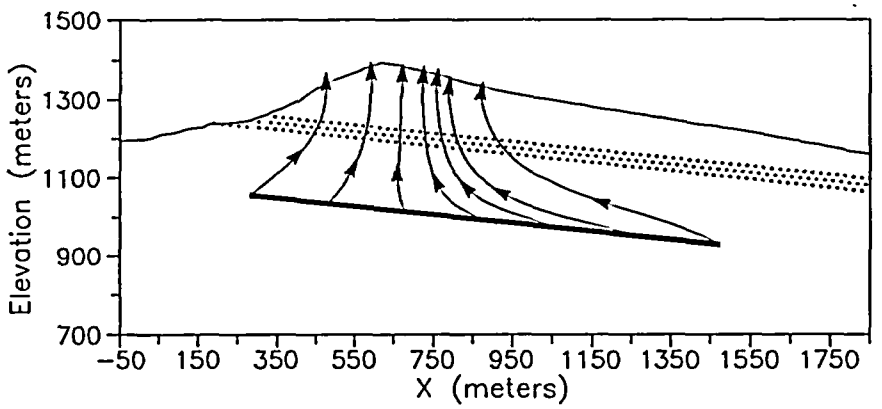

(b)

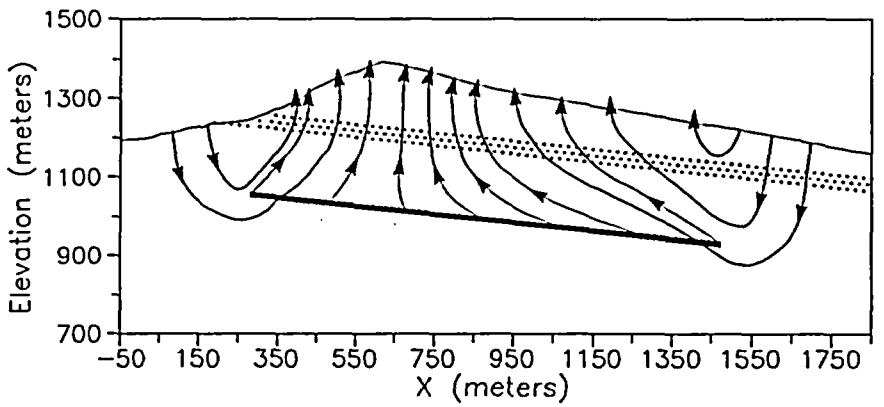

(c)

Figure 5-4. Path lines (a) with ambient temperature, no permeability contrast, (b) with the repository heated to 314 K, no permeability contrast, (c) with the repository heated to 330 K, no permeability contrast.

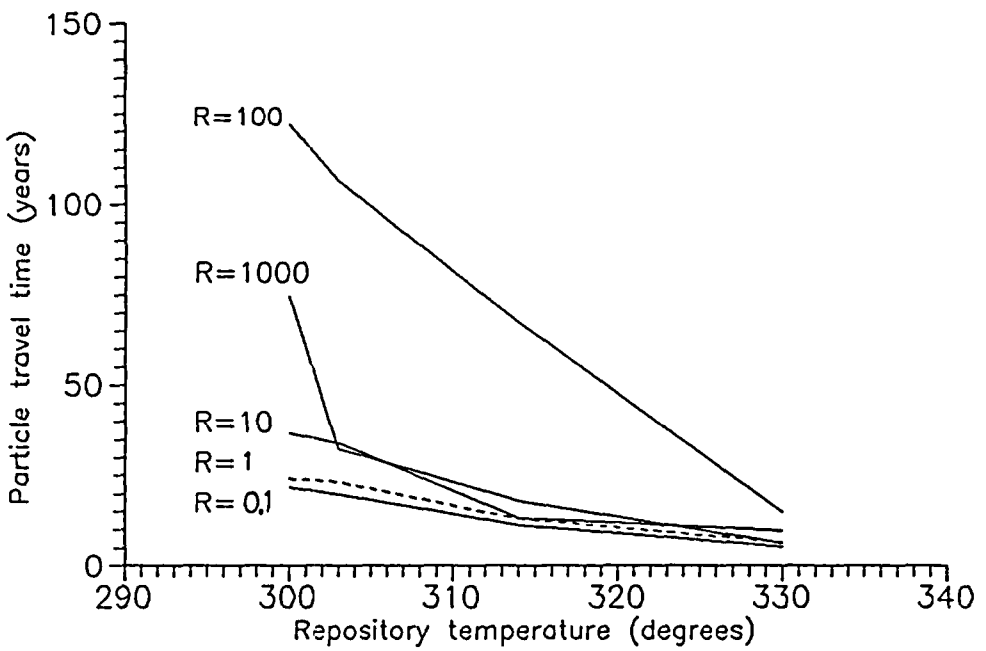

Figure 5-5. The minimum particle travel time from the repository as a function of temperature at the repository. R is the ratio of the intrinsic permeability of the Paintbrush nonwelded unit to that of the surrounding welded units.

the repository to the atmosphere. Figure 5-5 shows how the shortest particle travel time from the repository to the surface is related to the repository temperature. In all simulations, particles starting from near the left end of the repository had the shortest travel time. Since the contrast between the permeability of the middle and surrounding layers also affects travel time, curves corresponding to five different permeability contrasts are shown.

5.4.2 The effect of permeability contrast

The degree to which the permeability of the middle unit differs from the surrounding layers has a pronounced effect on the flow system predicted by the TGIF model. When a particle crosses a permeability boundary, its trajectory appears to follow the law of tangents, as one would expect. In addition, temperature and tilting of the layers affect the pattern of gas flow. With sufficient permeability contrast, the middle layer acts as a true confining layer, with independent flow systems above and below it.

Low-temperature situation--Figures 5-6a-e show path lines with the ambient temperature profile (no repository heating) and five different contrasts in permeability. In Figure 5-6b, the uniform permeability case, the path lines are smooth, are nearly symmetric around the center of the mountain, and all exit near the crest of the mountain. Figure 5-6a shows the case where the middle layer is 10 times more permeable than the surrounding layers. As would be expected, refraction in the direction of the bedding plane causes greater convergence of the flow lines.

Figures 5-6c-e show that when the middle layer has a progressively smaller permeability, the Paintbrush nonwelded unit becomes an increasingly effective confining layer. In Figure 5-6c (middle layer 10 times less permeable), path lines are refracted perpendicular to the bedding plane, reducing the convergence of the path lines. In Figure 5-6d (permeability 100 times less), path lines are diverted some distance laterally outward beneath the middle layer before penetrating it and traveling to the surface. Note that there is a pronounced convergence of these path lines above the layer. At a permeability contrast of a thousand, shown in Figure 5-6e, confinement by the middle layer is nearly complete; only one gas particle penetrates the layer. Path lines originating from the left side of the repository are directed laterally beneath the middle layer until they exit at the atmospheric boundary. Path lines under the layer from the center and right side of the repository form a

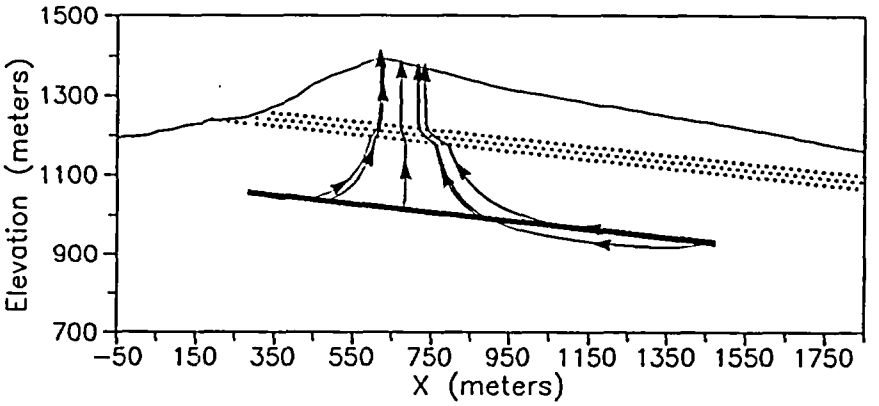

(a)

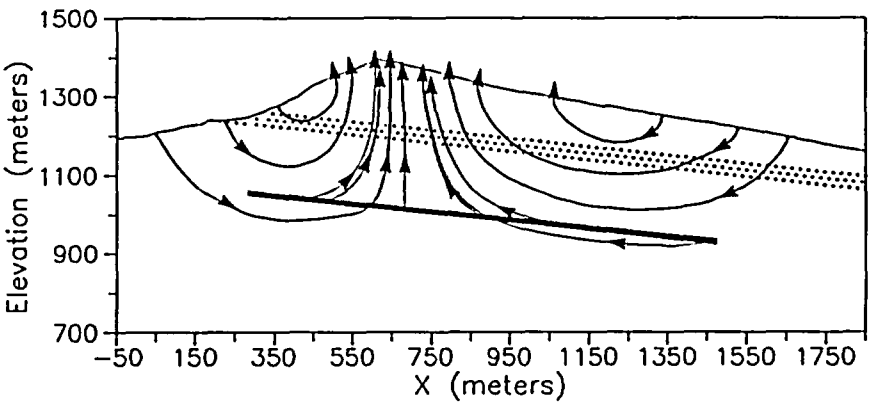

(b)

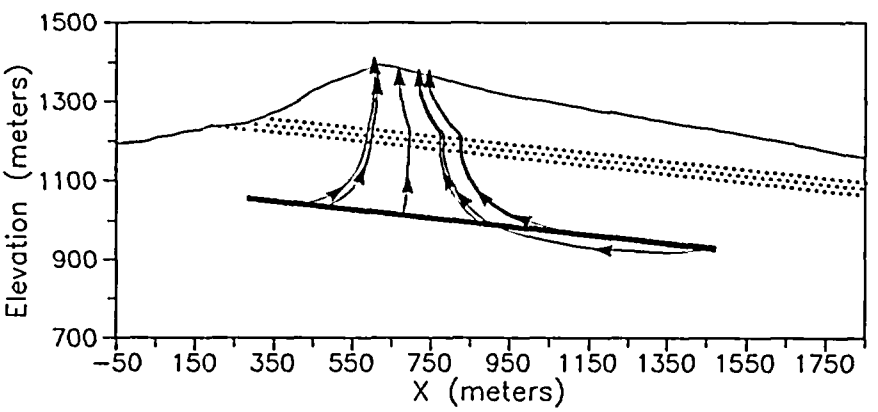

(c)

Figure 5-6. Path lines with ambient temperature, (a) 0.1× permeability contrast, (b) no permeability contrast, (c) 10× permeability contrast.

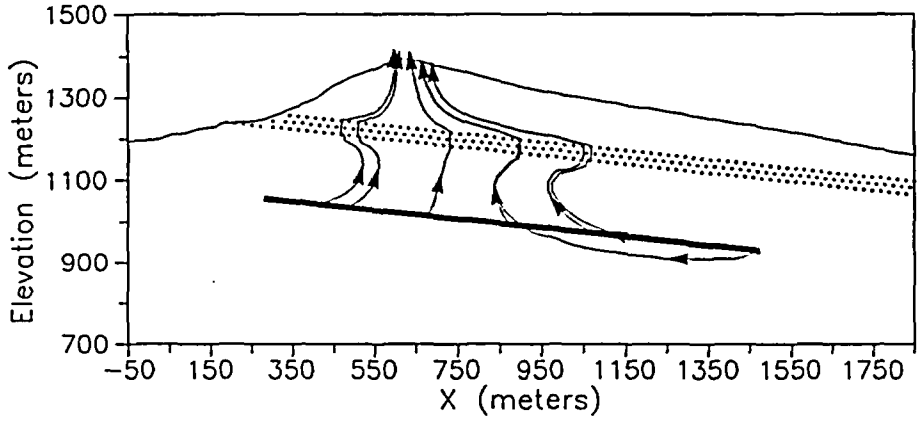

(d)

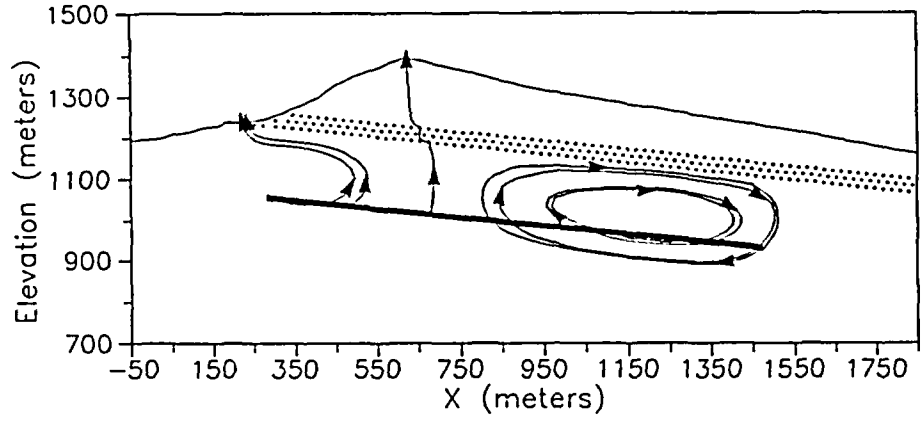

(e)

Figure 5-6 (cont'd). (d) 100× permeability contrast, (e) 1000× permeability contrast.

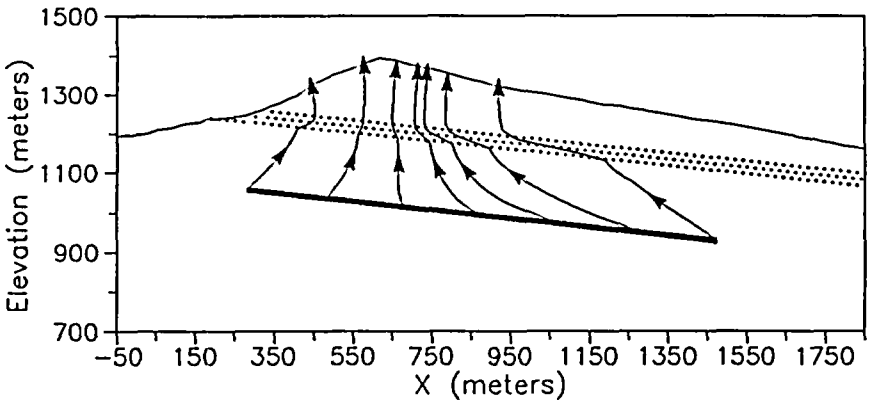

(a)

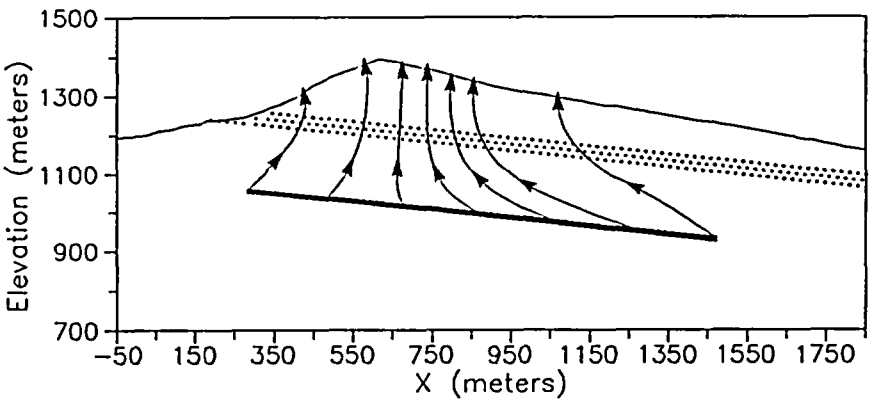

(b)

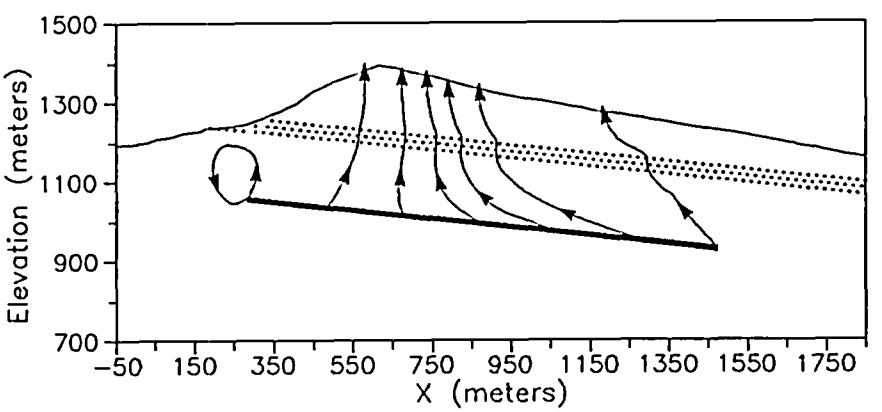

(c)

Figure 5-7. Path lines with the repository heated to 330 K, (a) 0.1× permeability contrast, (b) no permeability contract, (c) 10× permeability contrast.

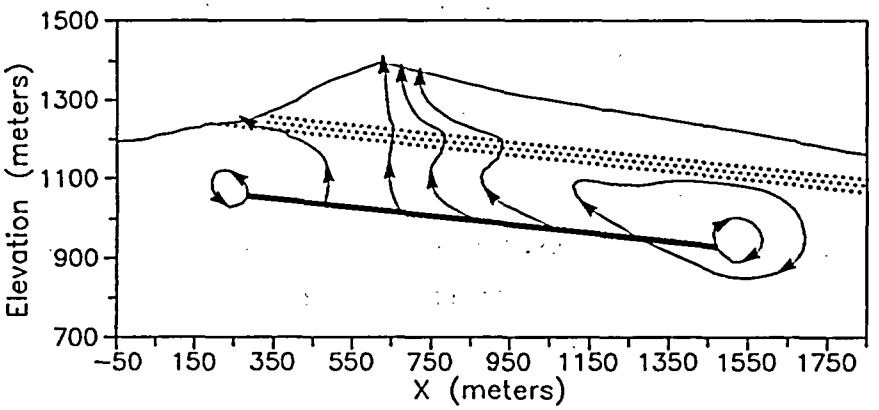

(d)

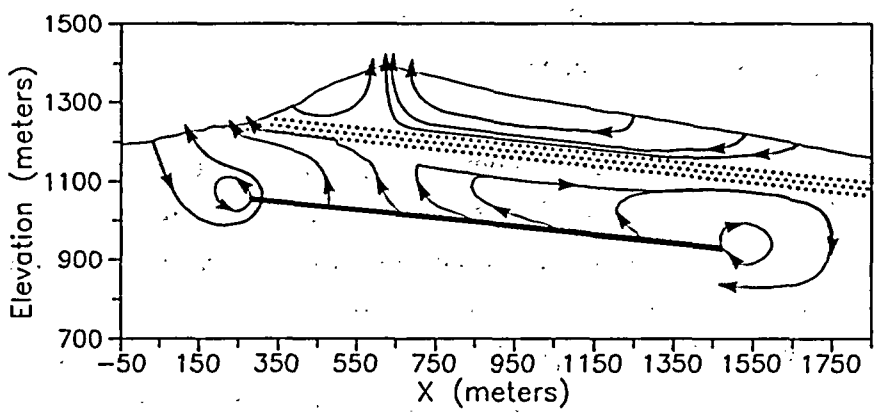

(e)

Figure 5-7 (cont'd). (d) 100× permeability contrast, (e) 1000× permeability contrast.

convection cell driven by a small horizontal temperature gradient. (When the temperature boundary conditions are changed slightly to eliminate the horizontal gradient, the convection cell disappears.)

High-temperature situation--Figures 5-7a-e show the path lines from a repository heated to a temperature of 330 K with five different contrasts in permeability. Although refraction again occurs in the middle layer, there are some important differences from the low temperature situation. Because the higher temperature causes a stronger buoyant flow, path lines tend to be shorter and more vertical when the permeability contrast is relatively small. This can be seen in Figures 5-7a-b. The higher velocities also promote divergent flow beneath the middle layer and the formation of convection cells at both ends of the repository as the permeability contrast increases (Figures 5-7c-e). When the permeability contrast reaches a factor of 1000 (Figure 5-7e), the middle layer becomes an effective confining layer and no path lines penetrate it.

Development of an upper and lower flow system As the permeability contrast increases, there is an increased tendency toward the development of separate flow systems on either side of the middle layer. This can be seen by comparing Figures 5-4c and 5-7e. In the no-contrast, high temperature case depicted in Figure 5-4c, the mountain contains a single flow system with a simple pattern of circulation. Some of the air entering the mountain flows deep enough to pass through the repository. All path lines originating from the repository exit near the crest of the mountain.

A very different situation can be seen in Figure 5-7e, which depicts the high contrast, high temperature case. Completely separate flow systems form above and below the middle layer because gas particles cannot penetrate it. Circulation in the upper system is very shallow and exits at the mountain's crest. In the lower flow system, gas particles from the left portion of the repository exit the left slope of the mountain where the lower layer crops out. Gas particles released from the right portion of the repository circulate back on themselves.

Travel Times Despite the thinness of the Paintbrush nonwelded unit, its permeability has a significant affect on the time required for gas particles originating from the repository to exit the mountain. Travel times generally increase as the permeability of the Paintbrush

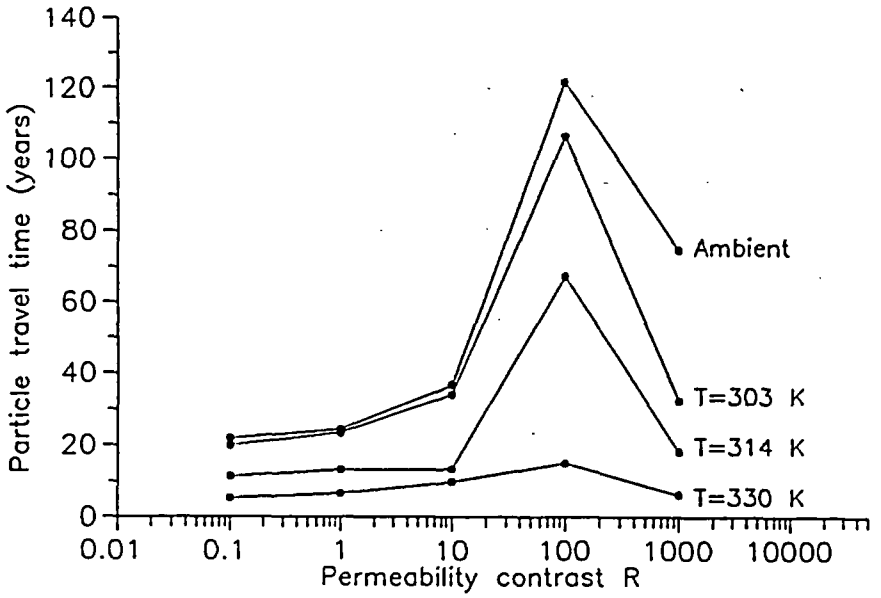

Figure 5-8. The minimum particle travel time from the repository as a function of the permeability contrast.

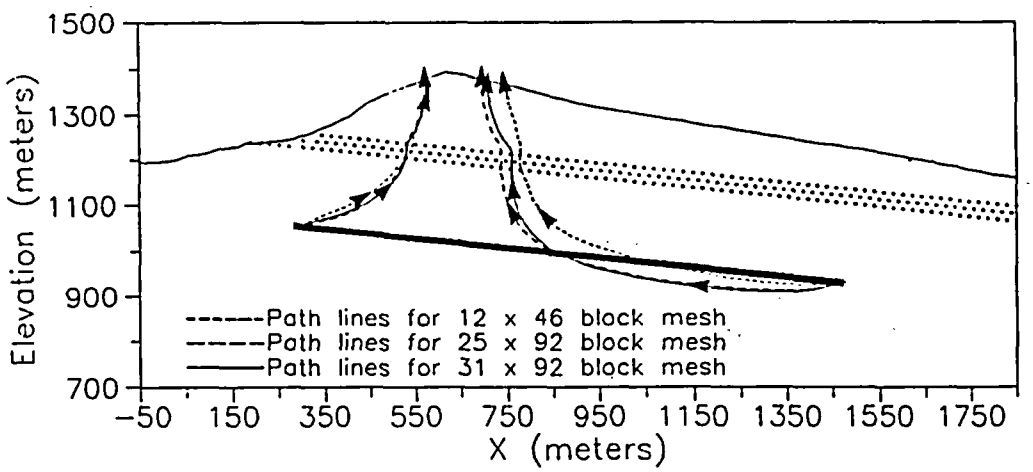

Figure 5-9. Comparison of path lines for different mesh densities with the repository heated to 303 K, 10 x permeability contrast.

nonwelded unit decreases. However, reducing the permeability by three orders of magnitude only increases the travel time by one order of magnitude. The reduction in travel times arises from two causes: decreased velocities through the layer and longer path lengths due to refraction. Figure 5-8 shows the relationship between permeability contrast and the minimum travel time for four different repository temperatures. Up to a permeability contrast of 100 times, there is a steady rise in travel time. An interesting exception to the trend occurs when the permeability contrast is 1000 times. Travel times for particles originating from the left side of the repository decrease because diversion beneath the middle layer causes path lengths to shorten. Examples of this can be seen in Figures 5-6e and 5-7e.

5.4.3 The effect of mesh density

Varying the mesh density produces only minor changes in predicted gas path lines. This can be seen in Figure 5-9, which shows path lines for three different mesh densities when the repository temperature is 303 K and the permeability contrast is 10 times. The predicted path lines for particles released from the repository are very similar for the three different mesh densities. In fact, at the left side of the repository the path lines are virtually indistinguishable. This is also the case for path lines originating from positions 2 through 6. The fact that the path lines are relatively insensitive to the changes in the mesh density indicates that all meshes used in this study are fine enough to yield reasonable results.

The TGIF model appears to be capable of simulating gas flow at Yucca Mountain over a wide range of inputs. Gas-flow path lines and travel times are highly dependent on the repository temperature as well as the degree of contrast between the Paintbrush nonwelded unit and surrounding layers. At extremely high permeability contrasts, two independent flow systems form above and below the middle layer.

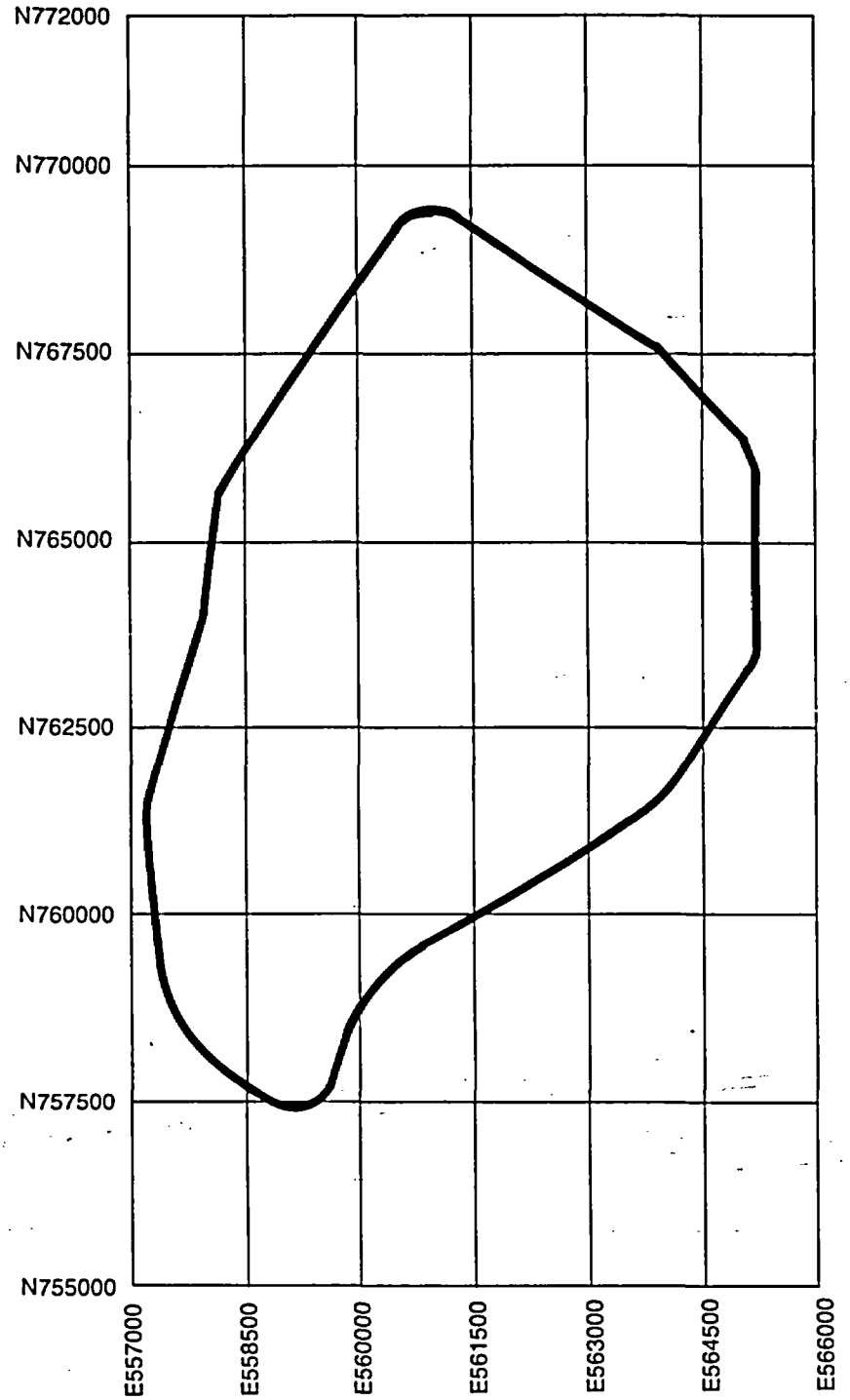

Figure 6-1. Map of the potential repository.

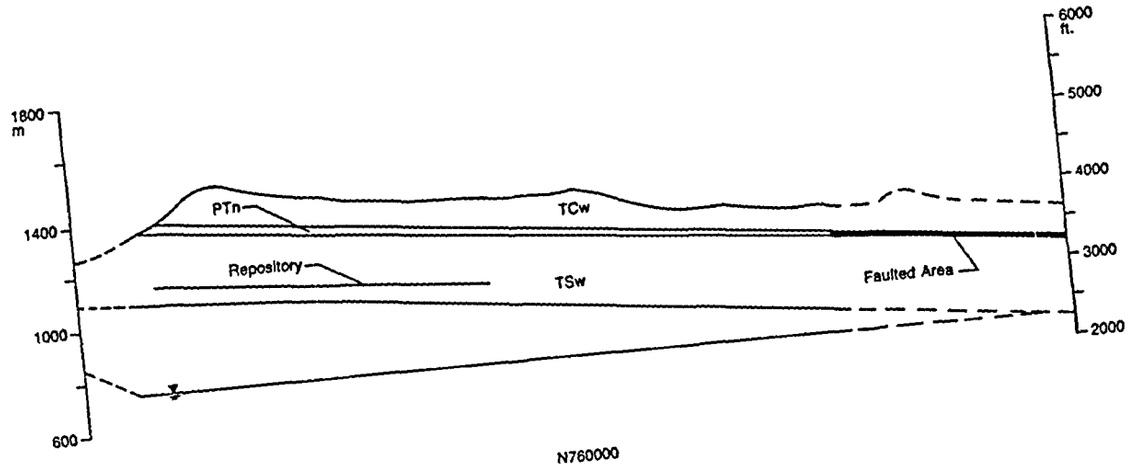

Figure 6-2. Geometry of cross section N760000.

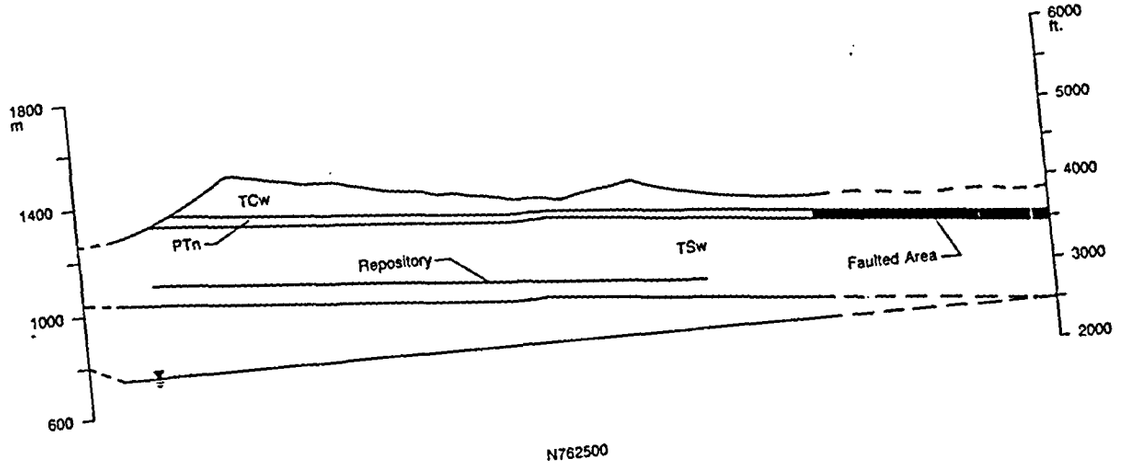

Figure 6-3. Geometry of cross section N762500.

CHAPTER 6
SIMULATION OF YUCCA MOUNTAIN

6.1 Physical problem

6.1.1 General

The TGIF model was used to model flow through the potential repository site at Yucca Mountain, Nevada. The objective of this work was to calculate flow patterns and gas particle travel times throughout the entire repository area. Gas flow in representative east-west cross sections through Yucca Mountain was simulated using the TGIF code described in Chapter 2. Two critical variables, permeability contrast between the Paintbrush nonwelded unit and the surrounding welded units (henceforth referred to as permeability contrast), and repository temperature, were varied to observe the effect on the flow field.

A range of permeabilities have been measured in the welded units of the Paintbrush tuff [Montazer et al., 1985]. Thus, there is some uncertainty in choosing a representative value. However, if the contrast between the welded and nonwelded units is held constant in the simulations, the results can be applied to any permeability because the calculated travel time scales linearly with the reciprocal of the permeability.

In all cases, steady-state conditions and annual average temperatures were assumed. Diurnal and seasonal effects were not considered. The calculated velocities thus represent annual averages. Annual-average velocities should be adequate to predict motion of carbon-14 particles, which will take centuries or millenia to reach the surface.

Permutations of three possible repository temperatures and two permeability contrasts were run for each cross section, resulting in six cases for each of the four cross sections. This resulted in a matrix of 24 computer simulations. Results are discussed below. Gas particle-track plots, created by the PATHLINE code described in Chapter 4, are shown for 16 of the cases. To predict the entire repository's performance, histograms of travel time were prepared, using the combined results of the four cross sections.

6.1.2 Geometry and zonation

Figure 6-1 shows a map view of the potential repository and its location on the State of Nevada coordinate system. (Numbers along the sides indicate distance in feet from the coordinate origin.) The four cross-sections used in this study, shown in Figures 6-2 through 6-5, are aligned along the four N-series coordinates that intersect the interior of the repository. These figures are generated from Sandia's Interactive Graphics Information System (IGIS). The dashed lines in Figures 6-2 through 6-5 represent parts of the cross-sections that were extrapolated using a geologic map [Scott and Bonk, 1984].

The cross-sections contain three hydrostratigraphic subdivisions of the Paintbrush Tuff Formation. These dip approximately six degrees to the east and differ in permeability. The upper and lower layers represent the Tiva Canyon welded unit and the Topopah Spring welded unit. These are thick, welded, densely fractured, and relatively permeable. The middle layer is the Paintbrush nonwelded unit, a thin, nonwelded tuff which includes all or part of several stratigraphic subdivisions of the Paintbrush Tuff.

The hydrostratigraphy just described was represented in the simulations by defining three materials with different permeabilities. The upper and lower welded layers were assumed to have identical material properties. The middle layer was assumed to have a faulted and an unfaulted zone with different permeabilities, both of which are less permeable than the welded units.

A finite difference mesh was prepared for each of the cross sections. All meshes contained 34 rows and 174 columns of blocks--a total of 5,916 blocks. Some of these blocks--the number varied among the four sections--were outside of the simulation boundaries. Figure 6-6 shows the mesh that represents the cross section shown in Figure 6-4. Meshes for other cross sections are similar. The mesh contains two sizes of rectangular blocks. An area including the Paintbrush nonwelded unit and extending approximately four rows into the welded tuff on either side of it contains blocks that measure 10 m high by 25 m long. Blocks in the remainder of the mesh measure 20 m by 25 m.

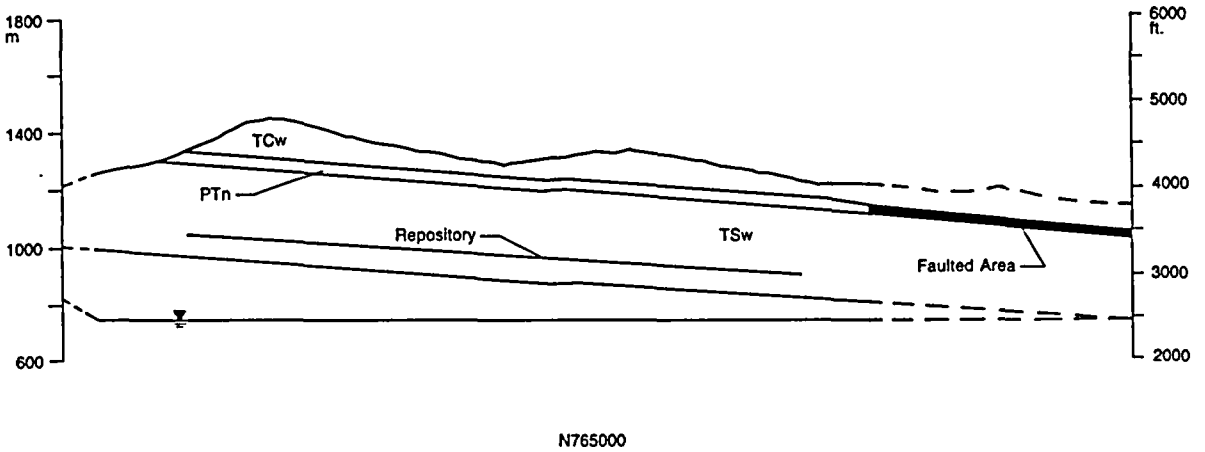

Figure 6-4. Geometry of cross section N765000.

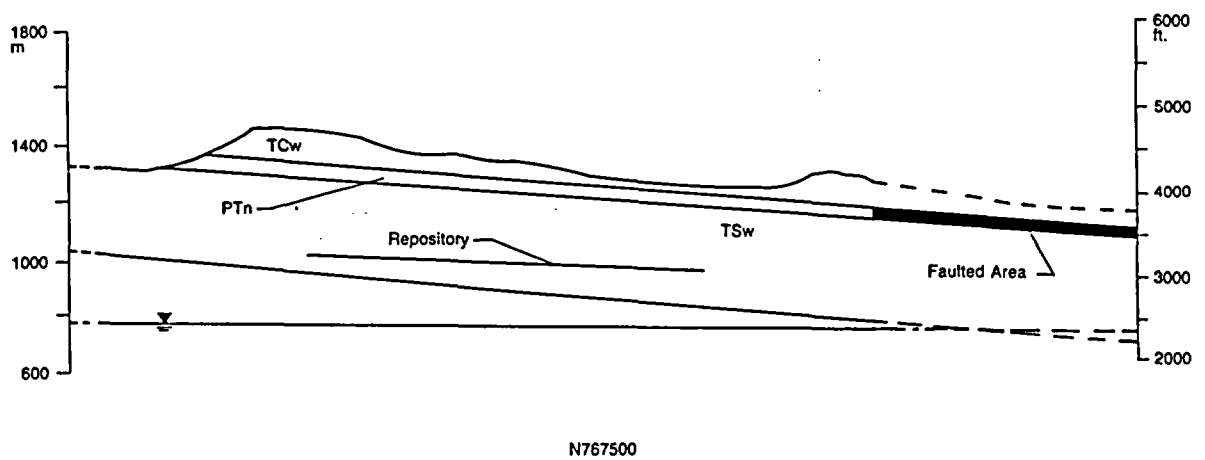

Figure 6-5. Geometry of cross section N767500.

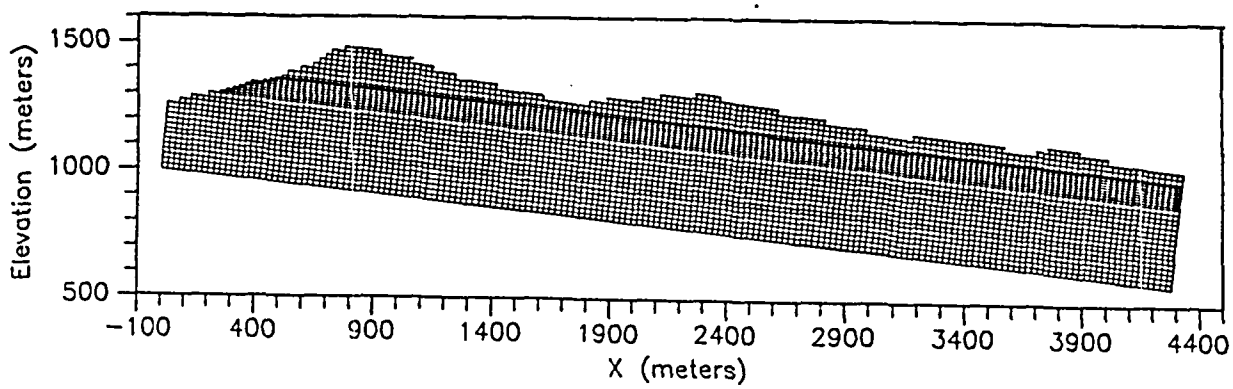

Figure 6-6. Finite difference mesh of cross section N765000.

The simulated region is surrounded by two types of boundary conditions:

- fixed head along the mountain's atmospheric contact, and
- no-flow conditions along the base and sides.

The numerical formulation of these boundary conditions is described in detail in Chapter 2. The no-flow boundary assigned at the base of the simulated region represents the top of the low-permeability tuffaceous beds of the Calico Hills unit, which would impede downward gas flow. The boundary to the west is located in the trough of Solitario Wash, which is a natural flow divide. The third no-flow boundary is located far to the east of the repository, so that it should have little effect on flow near the repository.

6.1.3 Parameter values

Parameter values used in these simulations are given in Tables 6-1 and 6-2. Three repository temperatures and two permeability contrasts were used to generate a matrix of six cases for each cross section. The values used to generate the matrix are listed in Table 6-1. Table 6-2 lists reference values and other parameters that were fixed for all six cases.

In all simulations, the permeability of the fractured Paintbrush nonwelded unit was assumed to be equal to the geometric mean of the unfractured Paintbrush nonwelded and the surrounding welded units.

The temperature field was calculated using the temperature generator described in Chapter 3. The extension grid option was used, which added 10 rows of increasingly thick blocks. This made the temperature grid 550 m longer in the downward direction than the grid used in TGIF.

TGIF calculates the freshwater head around reference values of temperature, pressure, fluid density, and viscosity. In this series of simulations, although these reference values were set at values characteristic of the gas at an altitude of 1075 m, the calculations assumed that conditions were characteristic of an elevation of 1275 m. This discrepancy is not significant because all gas properties are calculated relative to the reference values; it simply causes the model to calculate gas flows as if the Yucca Mountain area were 200 m closer to sea level than it really is.

Table 6.1

Variable Parameters Used in Each Cross Section

Repository temperature [K]	Permeability contrast[1] [dimensionless]	
	Ambient $k'/k = 10$	Ambient $k'/k = 100$
314 K	$k'/k = 10$	$k'/k = 100$
330 K	$k'/k = 10$	$k'/k = 100$

[1] k is the intrinsic permeability of the Paintbrush nonwelded unit. k' is the intrinsic permeability of the surrounding Tiva Canyon and Topopah Spring welded units.

6.2 Results

6.2.1 Flow paths

TGIF calculated the flow velocities, and PATHLINE was used to generate particle-track plots for 16 of the 24 cases. The particle tracks are shown as Figures 6-7 through 6-22. Note that these are tracks of arbitrarily located particles; the density of pathlines is not an indication of flux.

Because there are only minor differences in stratigraphy and topography among the four cross sections, their particle tracks tend to be very similar for conditions of equal permeability contrast and repository temperature.

A number of general conclusions can be drawn from these particle-track figures.

In all cases, the general pattern of flow is that air enters along the flanks of the mountain and converges and exits near the crest. Higher repository temperatures promote

Table 6-2

Values of Fixed Parameters

Parameter	Symbol	Value	Source
reference atmospheric temperature	T_a	296.44 K	--
reference fluid density	ρ_o	0.001007 g cm^{-3}	--
reference internal temperature	T_o	300 K	--
reference elevation	z_o	1275 m	--
reference pressure	P_o	880,521 dyn cm^{-2}	--
viscosity at T_o	$\mu(T_o)$	1.86×10^{-4} g cm^{-1} s^{-1}	Lide [1990]
temperature coefficient of viscosity	$\frac{d\mu}{dT}$	3.5×10^{-7} g cm^{-1} s^{-1} K^{-1}	Lide [1990]
atmospheric relative humidity at $z = 0$	η	20%	--
lapse rate	λ	6.5×10^{-5} K cm^{-1}	Donn [1975]
geothermal gradient	γ	2×10^{-4} K cm^{-1}	Montazer et al. [1985]
intrinsic permeability of the welded tuff	k'	1.0×10^{-7} cm^2	Montazer et al. [1985]

decreased convergence. (This can be seen especially clearly by comparing Figures 6-19 and 6-20.) Flow paths for particles originating on the steep west slope of the mountain tend to be short, while paths originating along the gentle east slope tend to be long.

Flow paths are very sensitive to topography--even small ridges can generate some convergence. This is particularly true at ambient temperatures (shown in odd-numbered Figures starting with 6-7 and ending with 6-21).

Repository temperature has an effect on the flow pattern. As temperature increases, the flow is controlled less by topography and more by temperature. Convergence decreases significantly. The combination of high temperatures and high permeability contrast always results in the formation of a convection cell near one or both ends of the repository. Such convection cells can be seen in Figures 6-10, 6-14, 6-18, and 6-22.

The fault zone below the east slope of the mountain appears to have little effect on the overall flow pattern. The explanation can be seen by examining the paths of the particles traveling through this zone. In most cases, travel distance through the fractured zone is very short in comparison to the distance traveled below the confining layer. Thus, the total resistance to flow is greater in the lower layer even though it has the greater permeability. This effect is less pronounced as repository temperature and permeability contrast increase. Sensitivity studies are required to quantify this conclusion.

6.2.2 Travel times

The PATHLINE program, described in Chapter 4, was used to calculate both gas-particle travel times and retarded carbon-14 travel times from the repository to the surface. The results of all four cross sections were used to generate a distribution of travel times that is representative of the entire repository.

The travel times are calculated for a mathematical particle that is not affected by diffusion or dispersion. These processes would affect a particle of carbon-14 or any other contaminant and cause some spreading in the distribution of travel times. However, the spreading of travel times caused by the geometry of the mountain and the gas flow field is so large that diffusion and dispersion can safely be ignored.

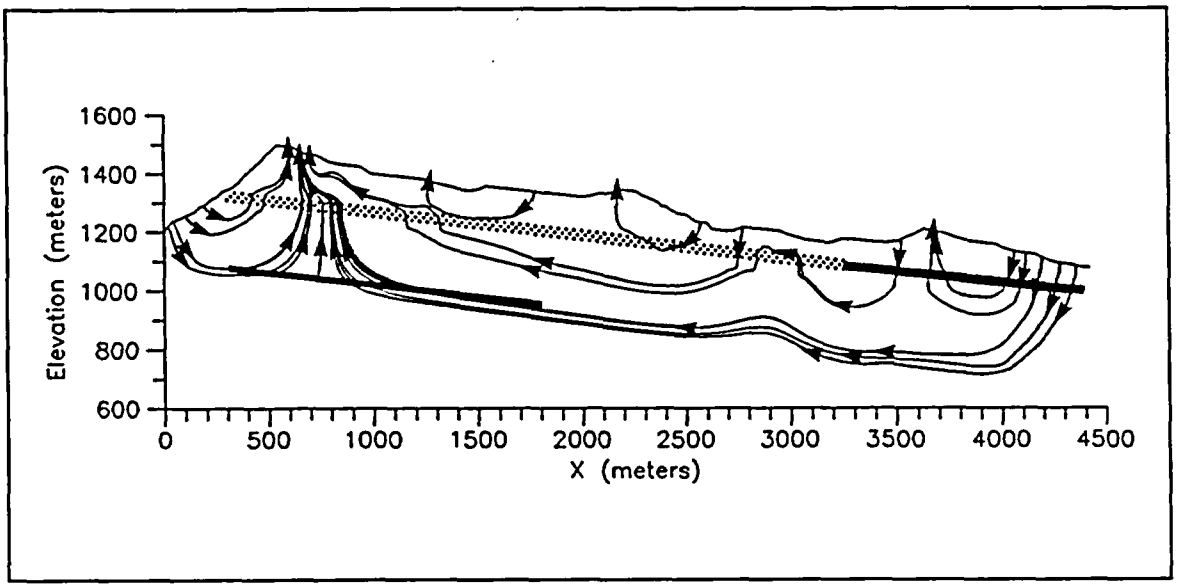

Figure 6-7. Path lines with ambient temperature, permeability contrast between welded and nonwelded tuffs 10× (3.3× in faulted area). (cross section N760000)

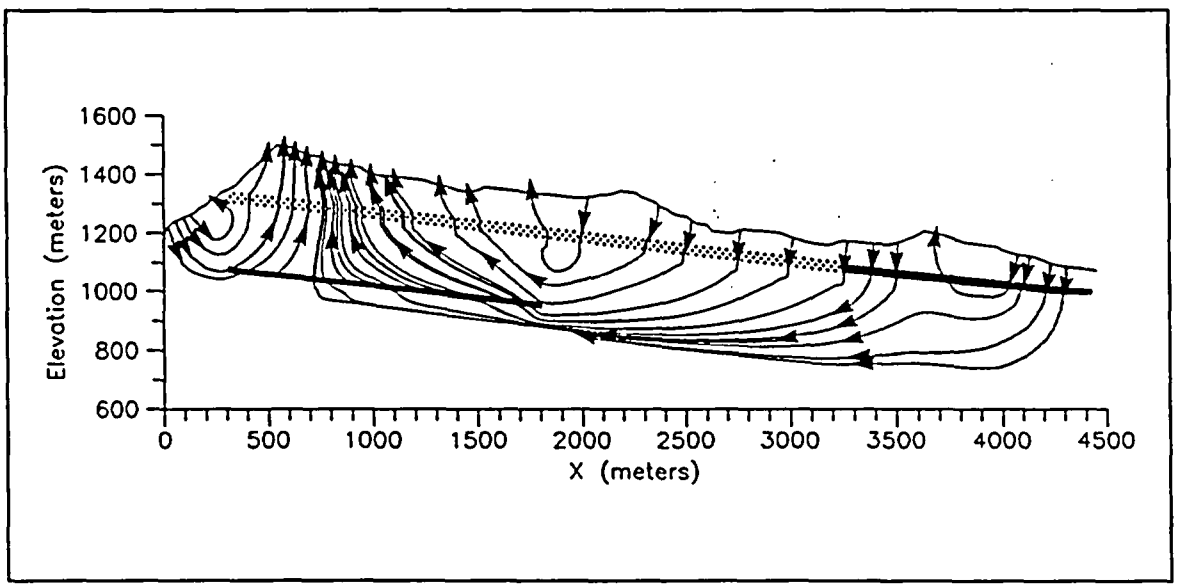

Figure 6-8. Path lines with the repository heated to 330 K, permeability contrast between welded and non welded tuffs 10× (3.3× in faulted area). (cross section N760000)

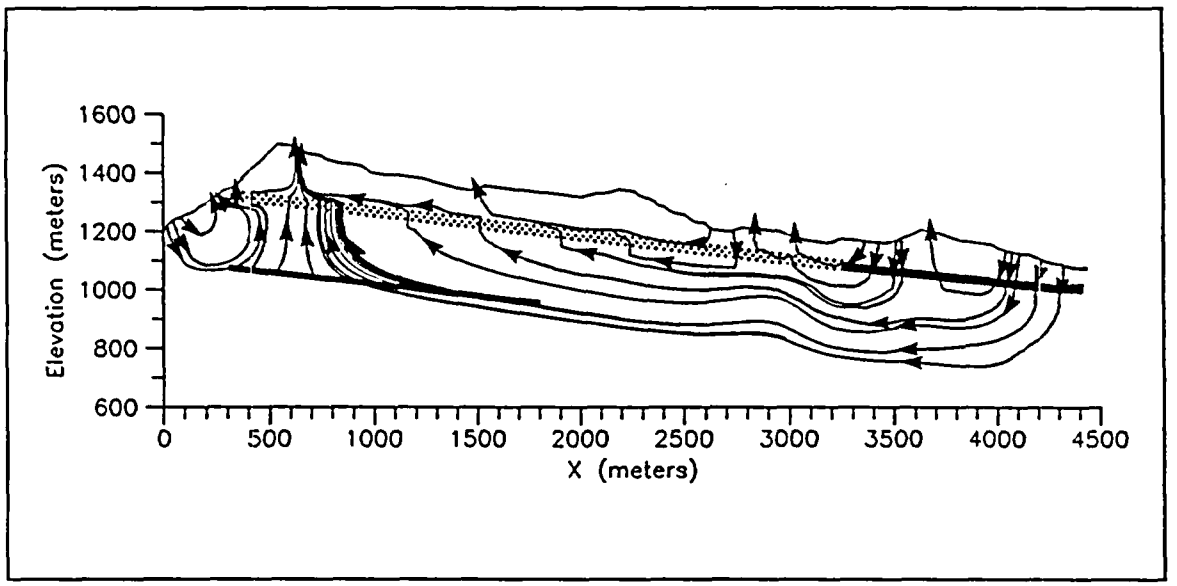

Figure 6-9. Path lines with ambient temperature, permeability contrast between welded and nonwelded tuffs 100x (10x in faulted area). (cross section N760000)

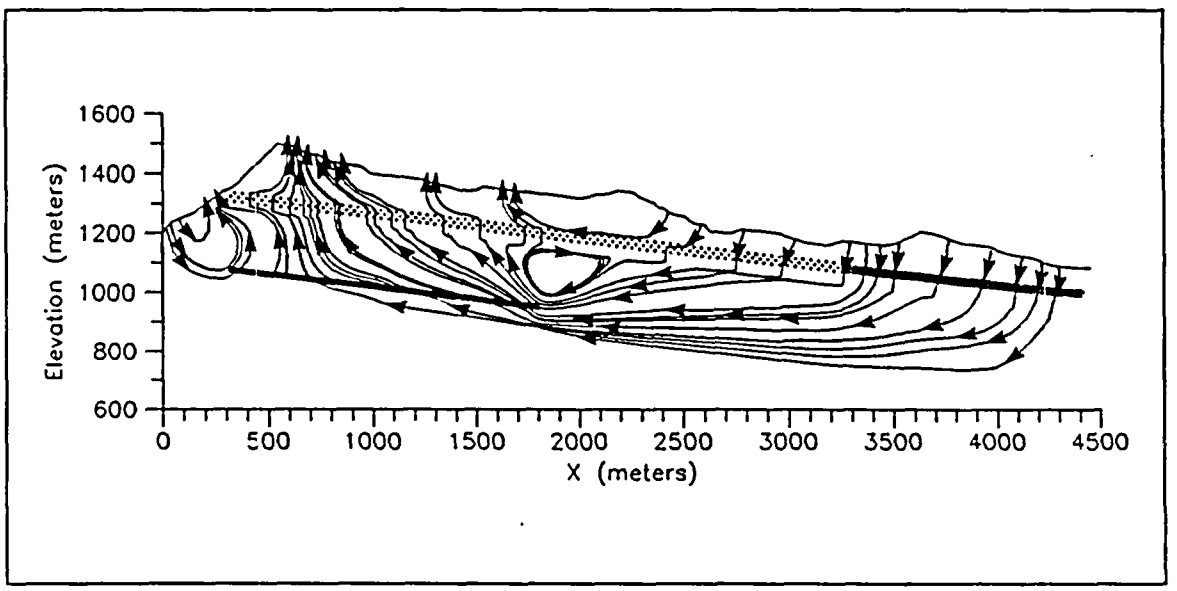

Figure 6-10. Path lines with the repository heated to 330 K, permeability contrast between welded and nonwelded tuffs 100x (10x in faulted area). (cross section N760000)

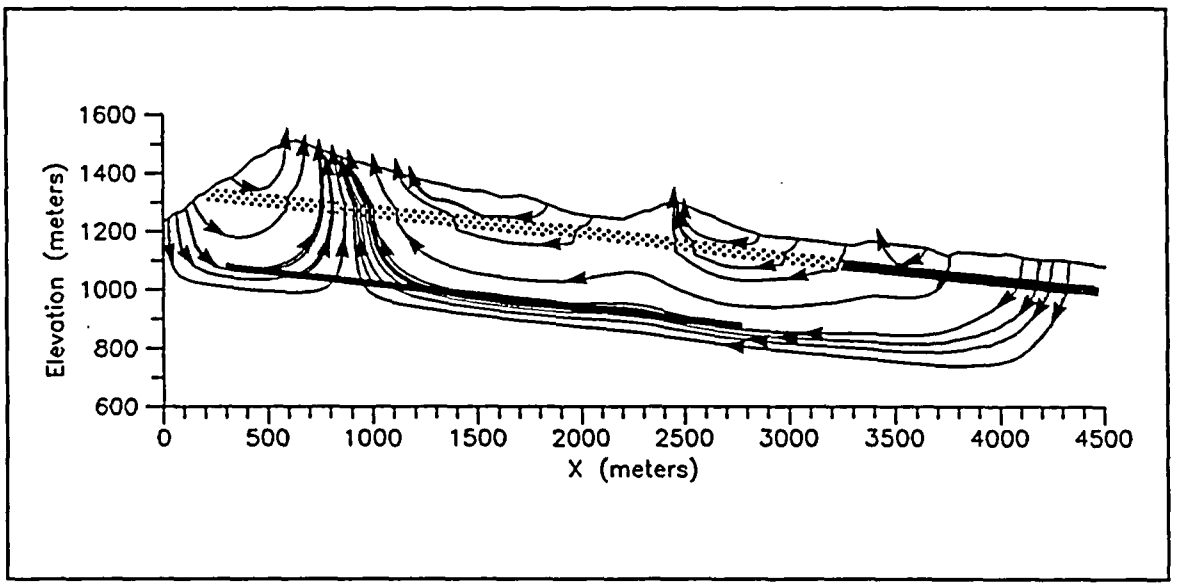

Figure 6-11. Path lines with ambient temperature, permeability contrast between welded and nonwelded tuffs 10× (3.3× in faulted area). (cross section N762500)

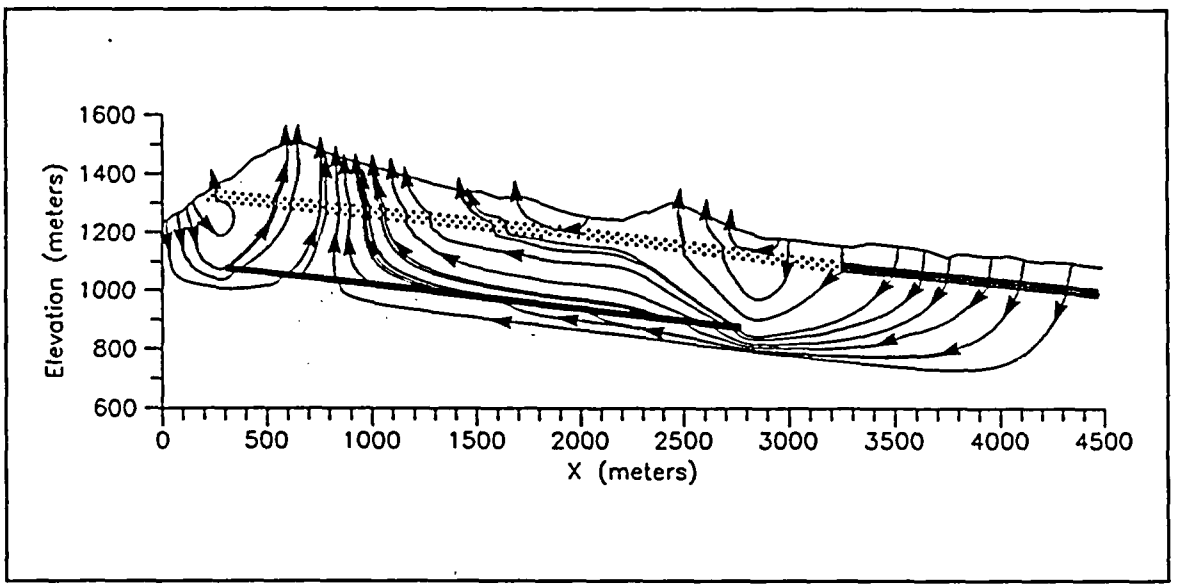

Figure 6-12. Path lines with the repository heated to 330 K, permeability contrast between welded and nonwelded tuffs 10× (3.3× in faulted area). (cross section N762500)

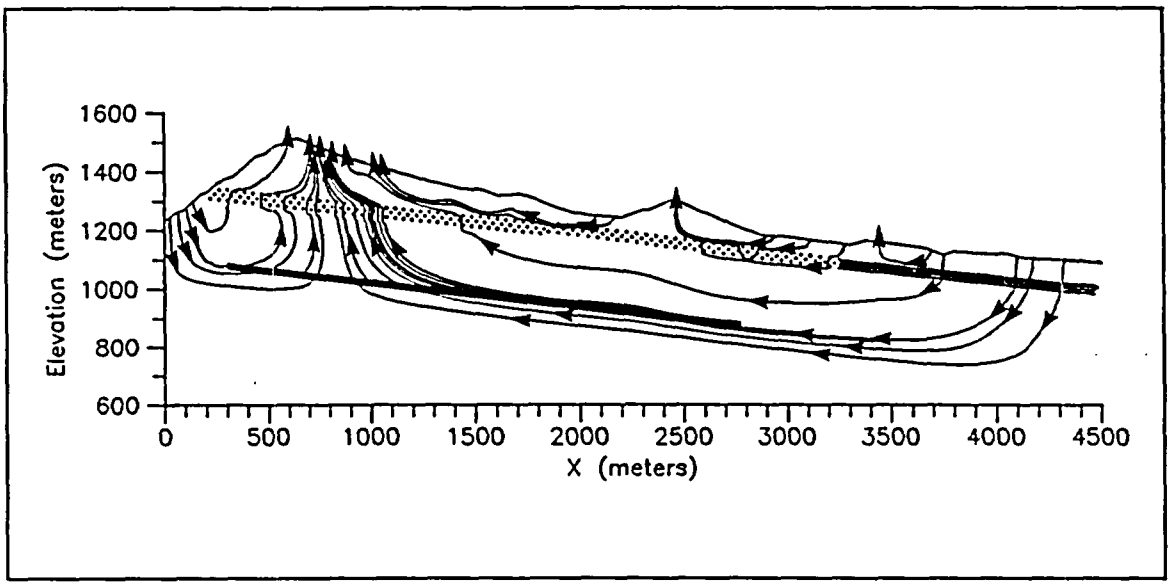

Figure 6-13. Path lines with ambient temperature, permeability contrast between welded and nonwelded tuffs 100x (10x in faulted area). (cross section N762500)

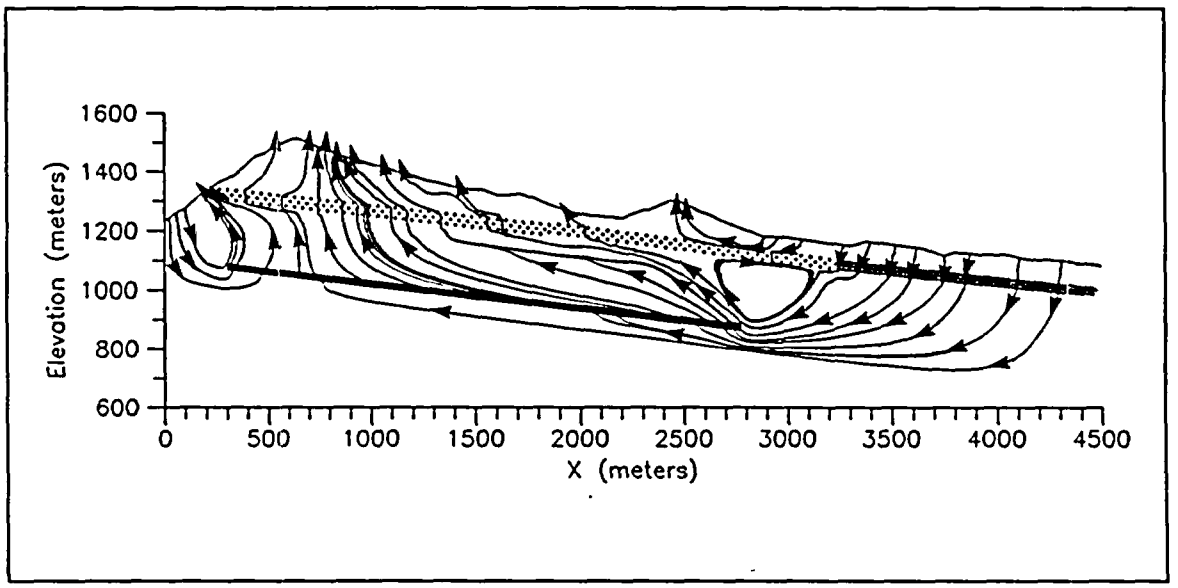

Figure 6-14. Path lines with the repository heated to 330 K, permeability contrast between welded and nonwelded tuffs 100x (10x in faulted area). (cross section N762500)

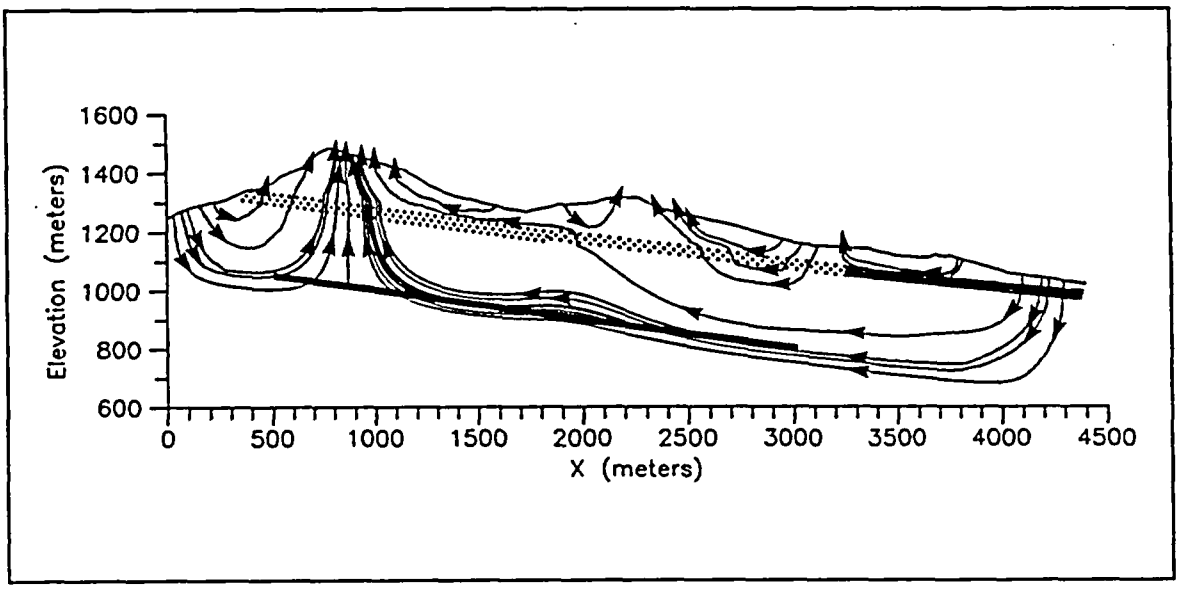

Figure 6-15. Path lines with ambient temperature, permeability contrast between welded and nonwelded tuffs 10× (3.3× in faulted area). (cross section N765000)

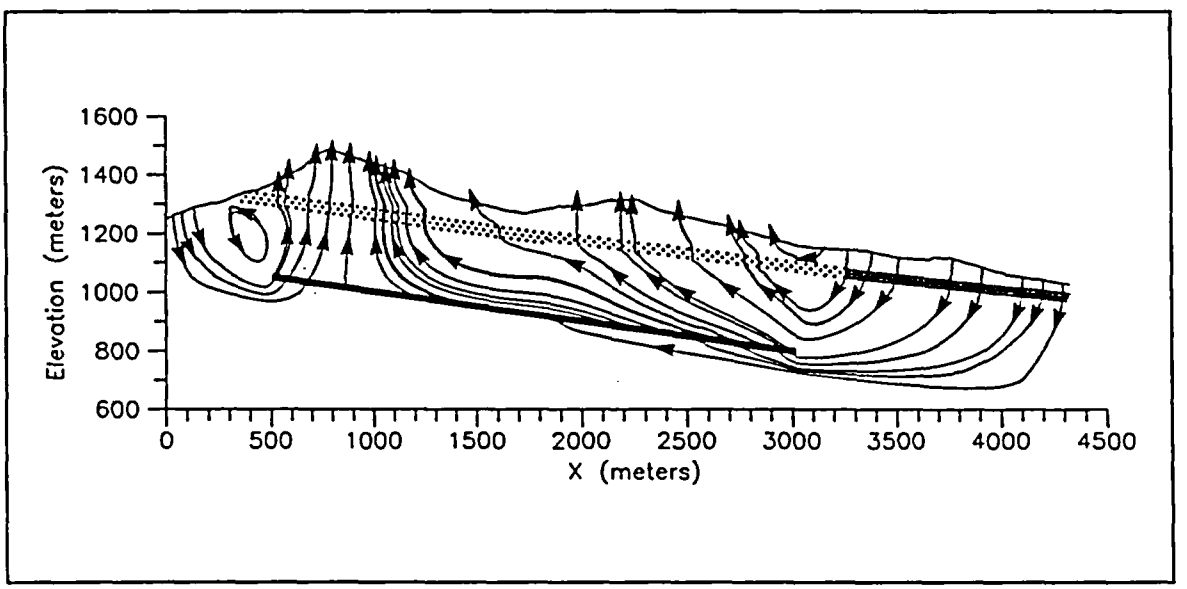

Figure 6-16. Path lines with the repository heated to 330 K, permeability contrast between welded and nonwelded tuffs 10× (3.3× in faulted area). (cross section N765000)

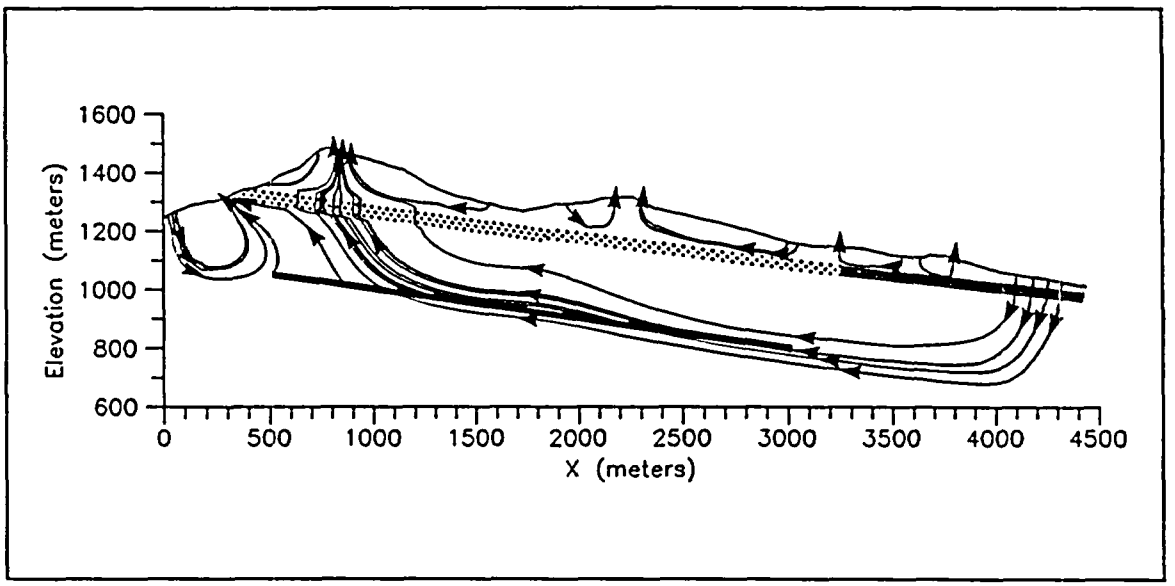

Figure 6-17. Path lines with ambient temperature, permeability contrast between welded and nonwelded tuffs 100x (10x in faulted area). (cross section N765000)

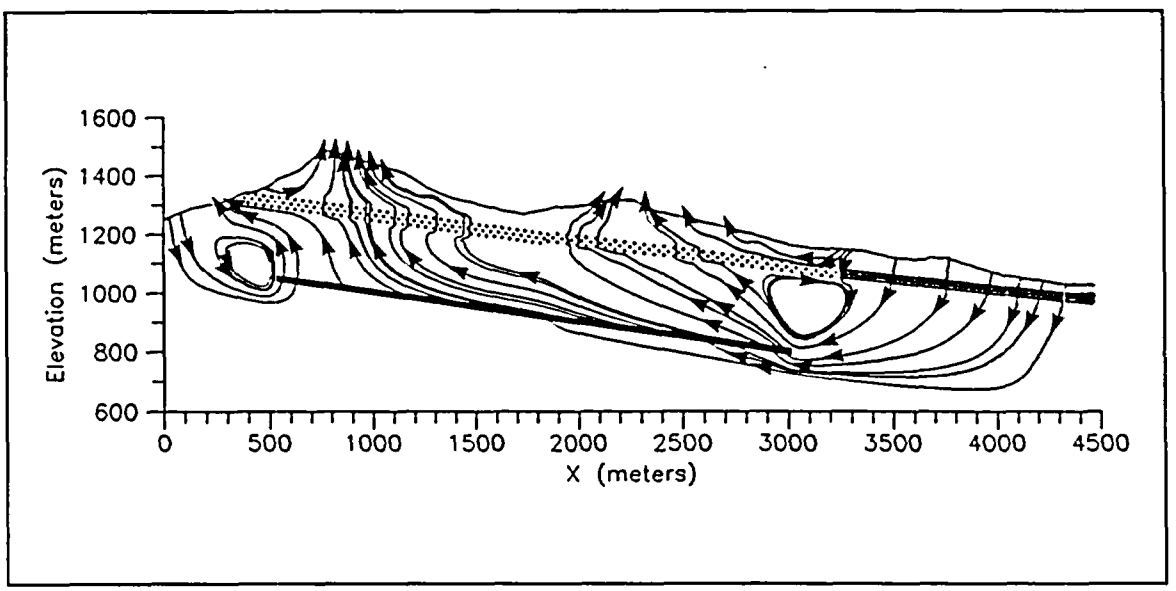

Figure 6-18. Path lines with the repository heated to 330 K, permeability contrast between welded and nonwelded tuffs 100x (10x in faulted area). (cross section N765000)

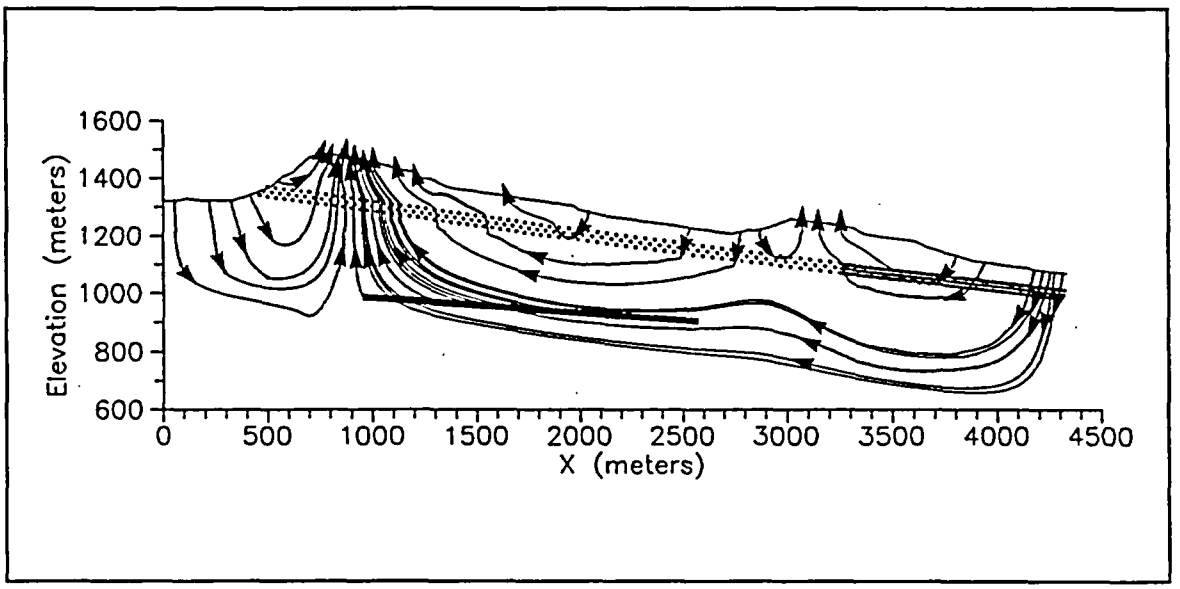

Figure 6-19. Path lines with ambient temperature, permeability contrast between welded and nonwelded tuffs 10× (3.3× in faulted area). (cross section N767500)

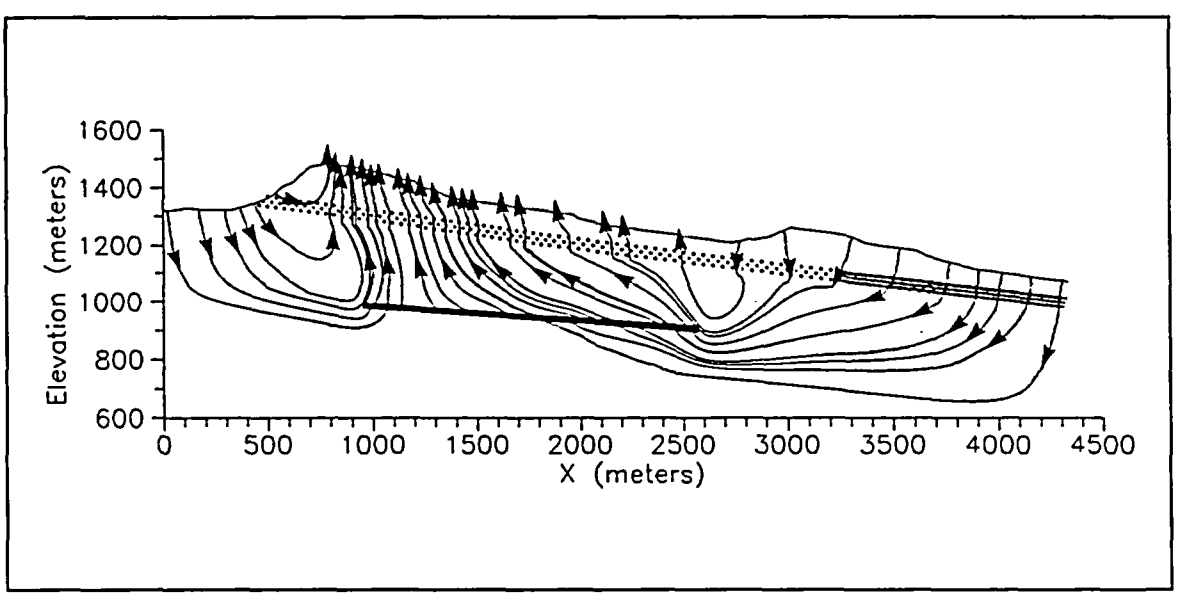

Figure 6-20. Path lines with the repository heated to 330 K, permeability contrast between welded and nonwelded tuffs 10× (3.3× in faulted area). (cross section N767500)

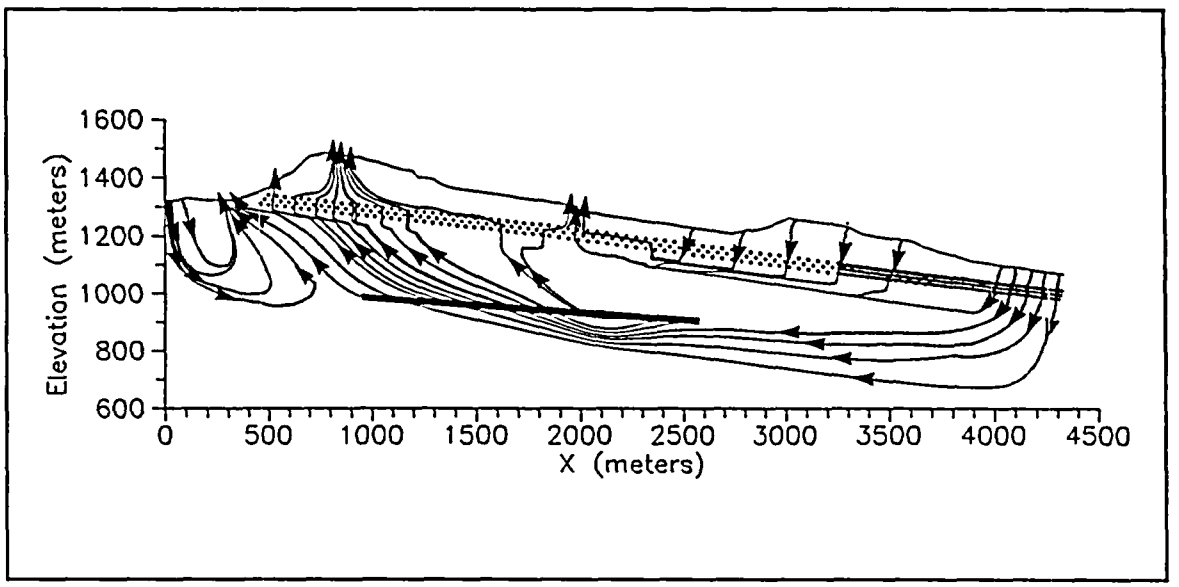

Figure 6-21. Path lines with ambient temperature, permeability contrast between welded and nonwelded tuffs 100x (10x in faulted area). (cross section N767500)

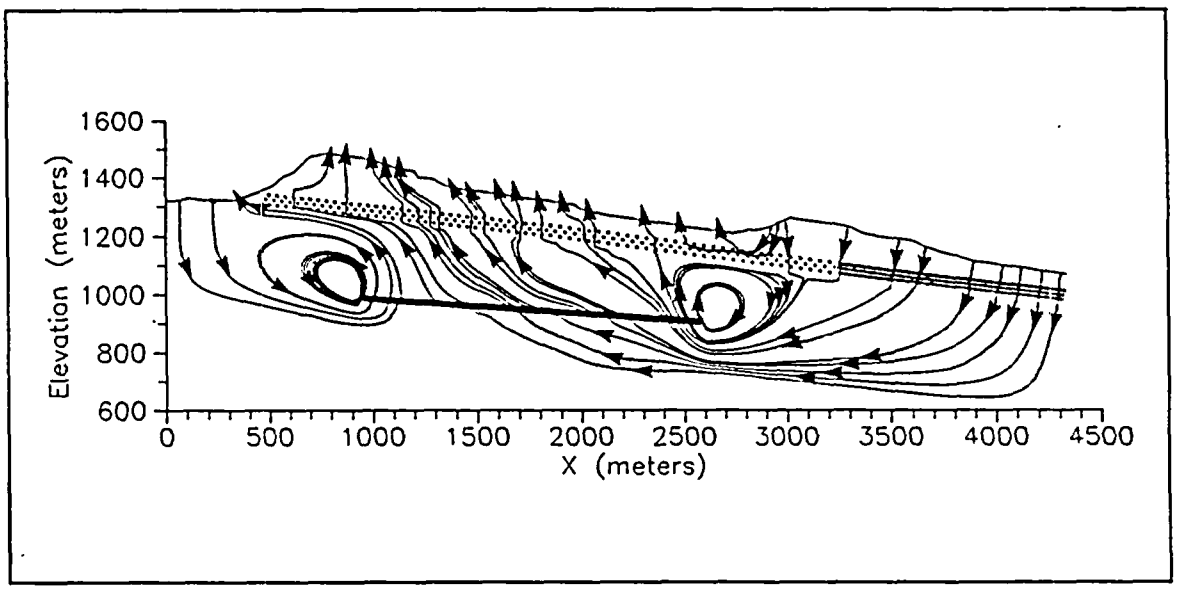

Figure 6-22. Path lines with the repository heated to 330 K, permeability contrast between welded and nonwelded tuffs 100x (10x in faulted area). (cross section N767500)

Measures had to be taken to prevent the results from being biased by a non-random selection of particle origins. Starting points were selected using a simple analogue of the Latin Hypercube method [Doctor, 1989]. In each of the four cross sections, the repository was divided into 25-meter intervals and the particle origin was chosen randomly within each interval. In all, travel times from the repository to the surface were calculated for 323 points. This method gives less statistical noise and avoids clustering of starting points compared to having the same number of particles randomly and independently located.

Figures 6-23 through 6-34 are travel time histograms that combine the results of all four cross sections. Figures 6-23 through 6-28 give the unretarded travel times for each of the six cases described above. Figures 6-29 through 6-34 give the retarded carbon-14 travel times for the six cases. Note that the high temperature, high contrast cases have closed convection cells near one or both ends of the ends of the repository. Particles in these regions thus have infinite travel times, which are shown in black on the histograms.

The retarded and non-retarded histograms are similar in shape but the relationship is more complex than a simple proportionality factor. This is because the retardation factor is dependent on both temperature and stratigraphy. Travel time is thus a function of not only path length, but also on the distribution of velocities and retardation values (both of which depend on stratigraphy) along the path length.

The histograms also demonstrate that the travel time is highly sensitive to both temperature and permeability contrast. At lower temperature and higher permeability contrast, many or most of the retarded travel times exceed the carbon-14 half life of 5730 years, and even the regulatory time frame of 10,000 years. On the other hand, with a low permeability contrast and a repository temperature of 330 K (which is only a moderately high temperature), almost all carbon-14 escapes to the atmosphere in less than 2,000 years.

The ambient-temperature path lines show that the Paintbrush non-welded unit is fairly effective as a semi-confining layer that separates the mountain into two flow systems, especially with 100× or more permeability contrast. This agrees well with the observation by Thorstenson [1991] that carbon-14 abundances differ above and below the non-welded unit. The calculated carbon-14 travel times of several times the carbon-14 half-life of 5730 years also exhibit good qualitative agreement with Thorstenson's measurements that show carbon-14 abundances on the order of one-quarter to one-half of modern.

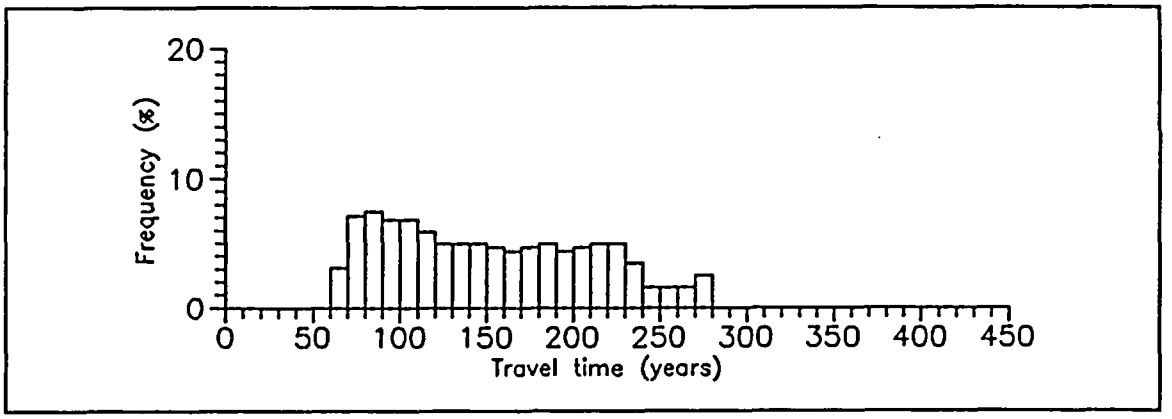

Figure 6-23. Unretarded travel times of particles from the repository to the atmosphere with ambient temperature, permeability contrast between welded and nonwelded tuffs 10× (3.3× in faulted area).

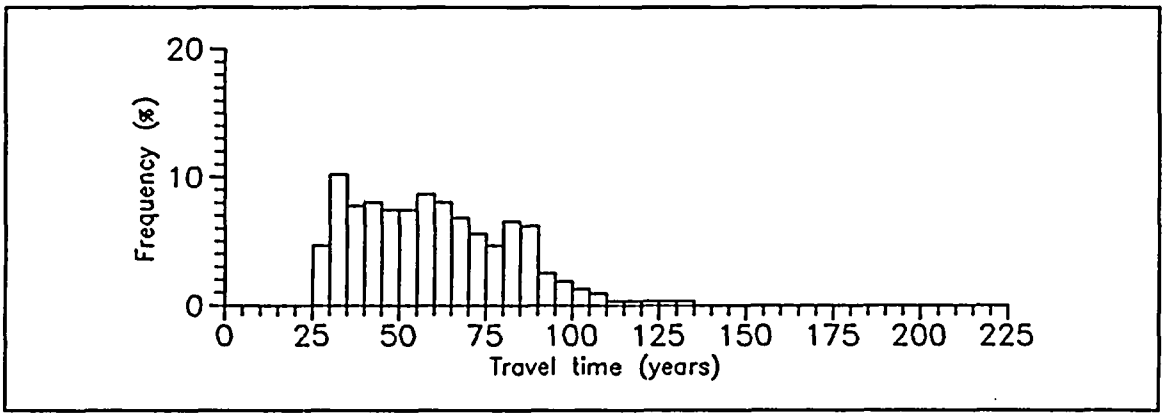

Figure 6-24. Unretarded travel times of particles from the repository to the atmosphere with the repository heated to 315 K, permeability contrast between welded and nonwelded tuffs 10× (3.3× in faulted area).

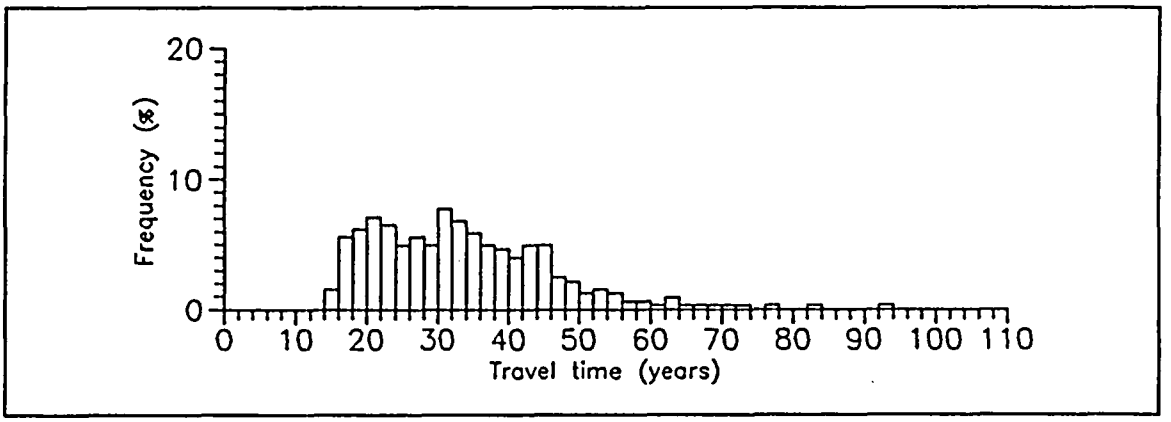

Figure 6-25. Unretarded travel times of particles from the repository to the atmosphere with the repository heated to 330 K, permeability contrast between welded and nonwelded tuffs 10× (3.3× in faulted area).

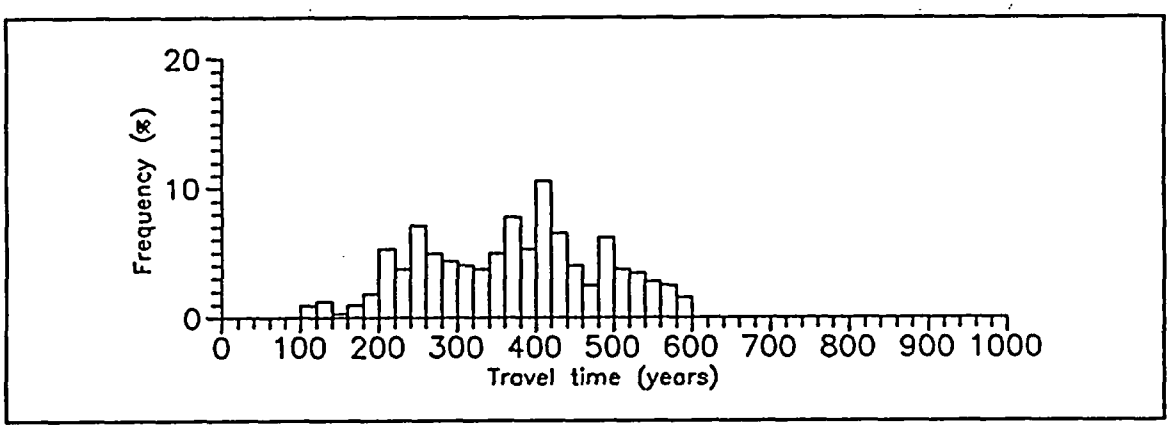

Figure 6-26. Unretarded travel times of particles from the repository to the atmosphere with ambient temperature, permeability contrast between welded and nonwelded tuffs 100× (10× in faulted area).

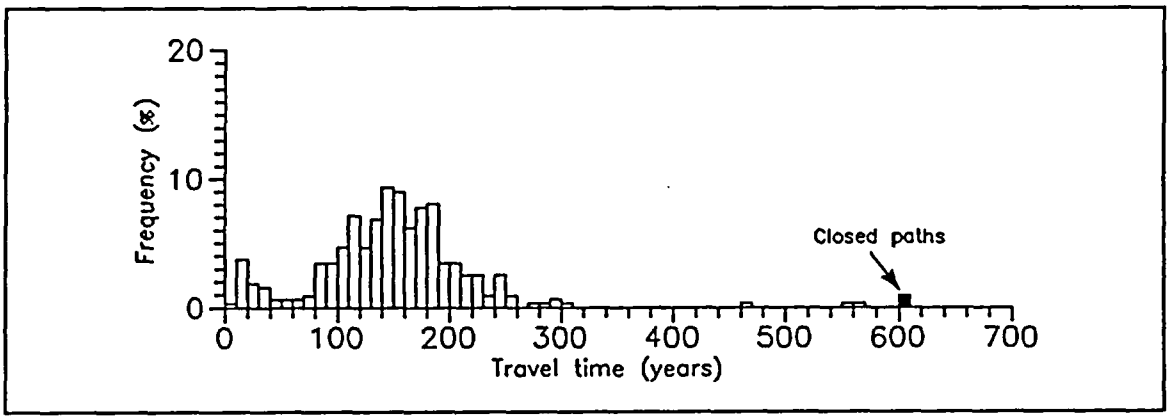

Figure 6-27. Unretarded travel times of particles from the repository to the atmosphere with the repository heated to 315 K, permeability contrast between welded and nonwelded tuffs 100× (10× in faulted area).

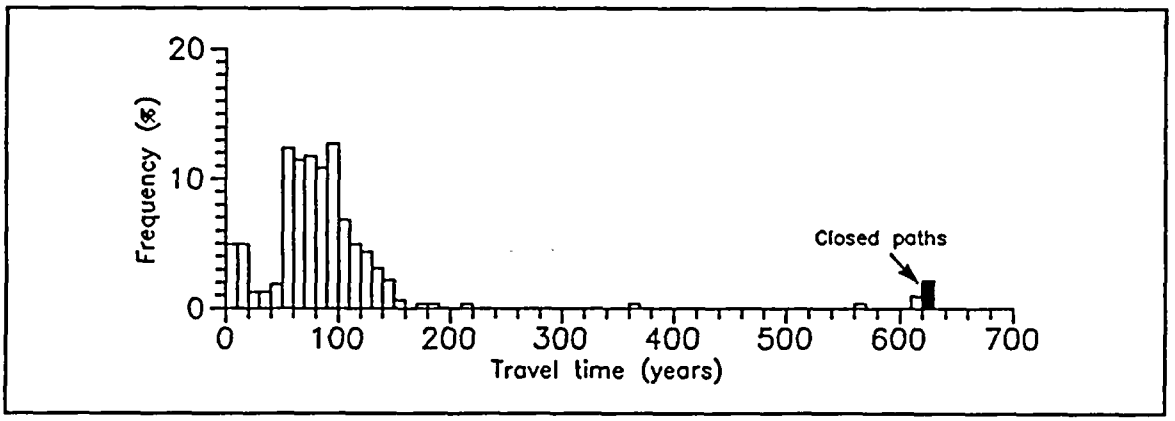

Figure 6-28. Unretarded travel times of particles from the repository to the atmosphere with the repository heated to 330 K, permeability contrast between welded and nonwelded tuffs 100× (10× in faulted area).

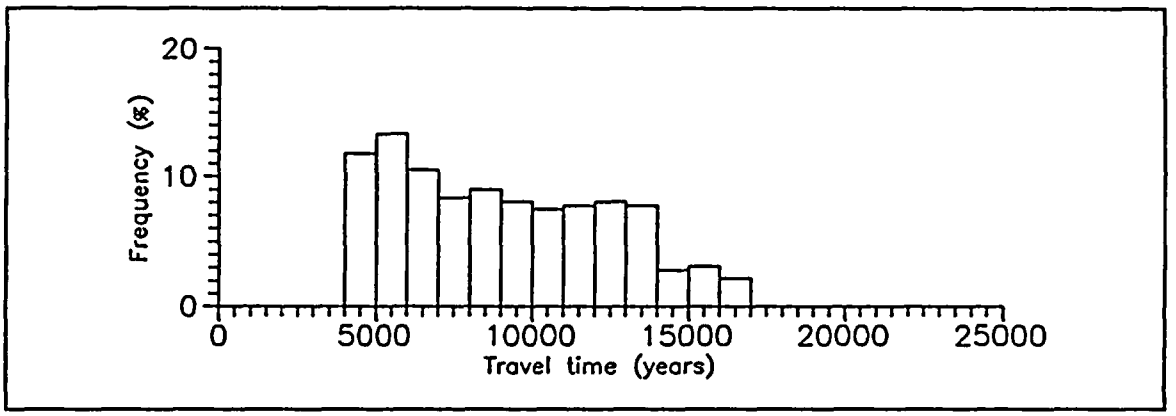

Figure 6-29. Retarded travel times of particles from the repository to the atmosphere with ambient temperature, permeability contrast between welded and nonwelded tuffs 10× (3.3× in faulted area).

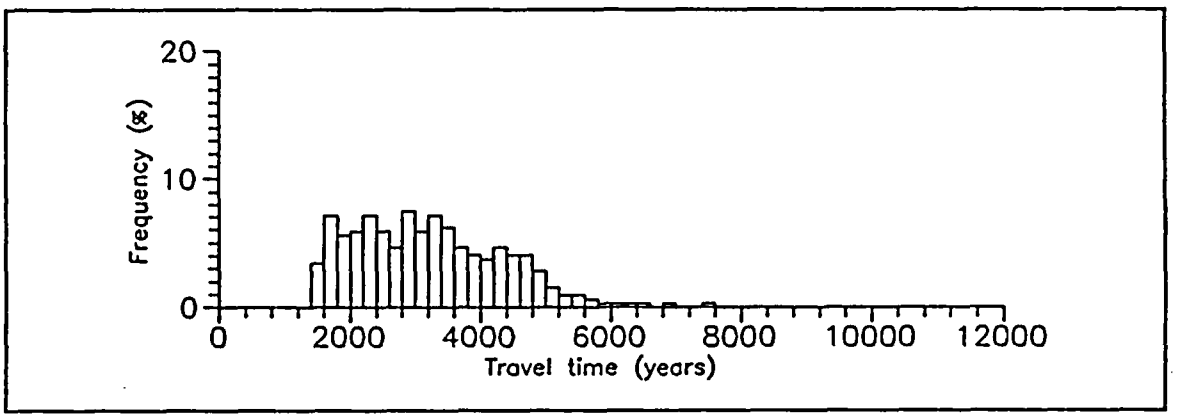

Figure 6-30. Retarded travel times of particles from the repository to the atmosphere with the repository heated to 315 K, permeability contrast between welded and nonwelded tuffs 10× (3.3× in faulted area).

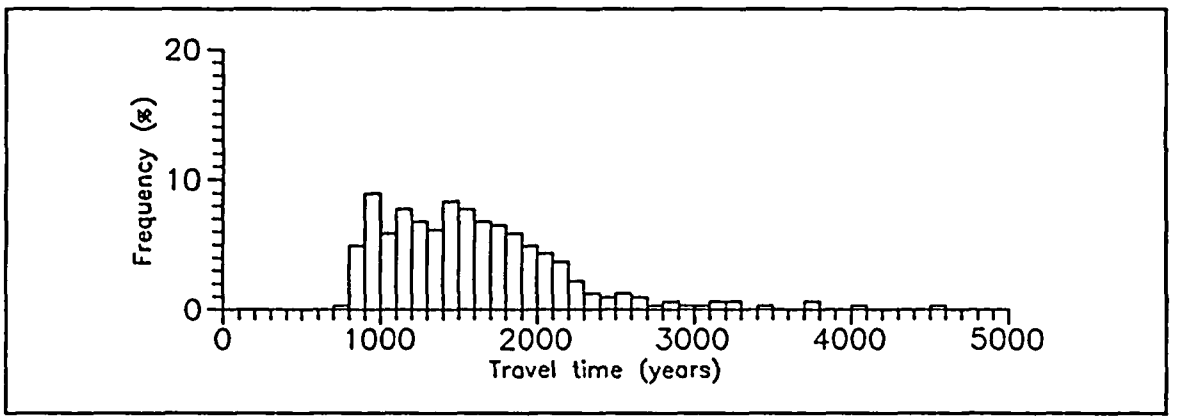

Figure 6-31. Retarded travel times of particles from the repository to the atmosphere with the repository heated to 330 K, permeability contrast between welded and nonwelded tuffs 10× (3.3× in faulted area).

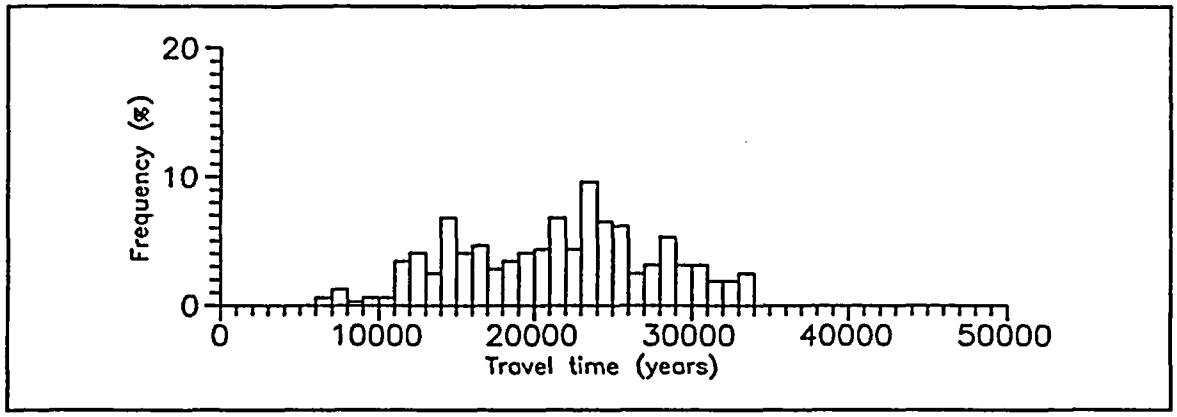

Figure 6-32. Retarded travel times of particles from the repository to the atmosphere with ambient temperature, permeability contrast between welded and nonwelded tuffs 100× (10× in faulted area).

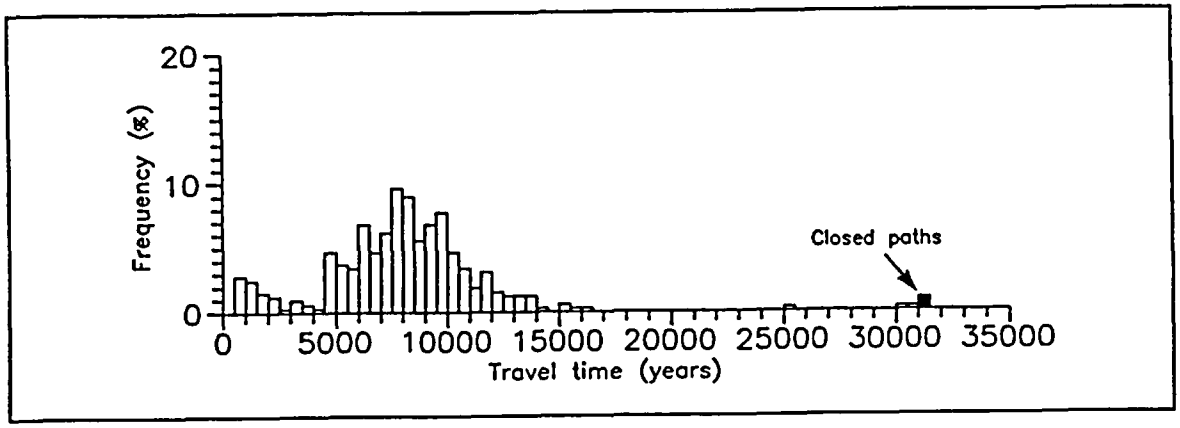

Figure 6-33. Retarded travel times of particles from the repository to the atmosphere with the repository heated to 315 K, permeability contrast between welded and nonwelded tuffs 100× (10× in faulted area).

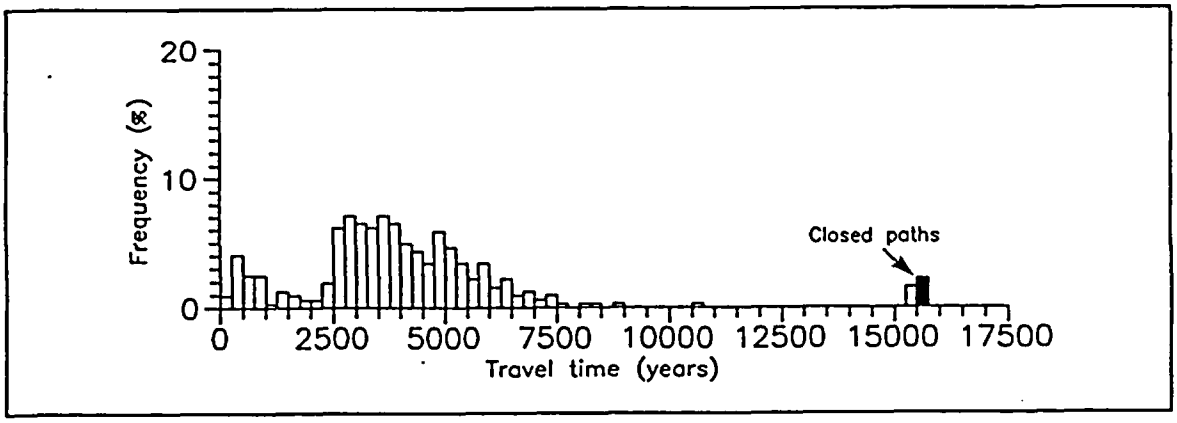

Figure 6-34. Retarded travel times of particles from the repository to the atmosphere with the repository heated to 330 K, permeability contrast between welded and nonwelded tuffs 100× (10× in faulted area).

CHAPTER 7
CONCLUSIONS AND RECOMMENDATIONS

The TGIF model simulates subsurface gas flows driven by topographic and repository-inducted temperature gradients. Because of the fresh-water-head formulation of the governing equation, the model is extremely sensitive and can successfully calculate flows driven by very small temperature differences.

We have used the TGIF model to calculate the movement of gas within Yucca Mountain, Nevada. Simulations were conducted along four east-west cross-sections through the potential high-level waste repository. The geometry of the cross-sections closely follows the current understanding the mountain's stratigraphy and topography. Six different cases were simulated, reflecting different temperatures as the repository cools and different assumptions about the permeability contrast between welded and non-welded tuffs. All simulations were annual averages, based on constant atmospheric temperatures.

In each case, travel times of particles moving with the gas from the repository to the land surface were calculated. Two different kinds of travel times were computed: one for a particle that moves with the gas, and one for a carbon-14 particle whose movement is retarded by isotopic exchange with the aqueous phase. The amount of retardation of the carbon-14 was calculated from a chemical model that assumes the water is in isotopic equilibrium with calcite.

Travel times were calculated for particles starting from 323 locations distributed along all four cross-sections. The results are presented in Chapter 6 in the form of histograms, giving a synoptic view of gas and carbon-14 travel times throughout the potential repository.

At temperatures close to pre-emplacement values, especially if the non-welded tuffs have a small permeability, carbon-14 travel times tend to be comparable to or larger than the half-life of 5730 years. At the highest temperature simulated, a case where the repository is at 330 K (a value that will be reached only after some period of cooling), the carbon-14 travel times were mostly in the range of 1000 to 2000 years in the case where the nonwelded tuff is relatively permeable, and somewhat longer in the less permeable case.

These travel times are all based on an assumed welded-tuff permeability of 10^{-11} m^2. As the model is linear in permeability (as long as the ratio of welded-tuff to non-welded-tuff permeability is held constant), travel times for other values of this parameter can be calculated by direct scaling. However, the value of 10^{-11} m^2 is based on a large-scale measurement involving the propagation of barometric-pressure fluctuations into the mountain and is therefore fairly reliable.

Additional field or experimental work could reduce uncertainty in predictions made by the model. Areas where significant reductions in uncertainty might be achievable include:

- Measurement of the permeability of the nonwelded tuffs.
- Confirmation or rejection of the hypothesis that ground-water chemistry is controlled by calcite equilibrium.

In addition, an estimate of the rate at which carbon-14 will be released from the repository is needed to predict carbon-14 releases to the surface.

There are several areas where the TGIF model should be improved to make it more accurate, applicable over a larger range, and usable for more purposes. Recommended model improvements include:

- Add a convection term (including latent heat) to the temperature model and couple it to the gas-flow model.
- Make the temperature model transient rather than steady-state. This, along with the inclusion of a convection term, would give TGIF the capability of predicting temperatures in a regime to which other heat-transfer codes used by the Yucca Mountain Project are ill-adapted.
- Allow the model to solve problems in radial coordinates. This would permit solution of flows through open boreholes, improving the opportunities for validation by comparison with field experiments.
- Add alternative retardation curves that reflect different assumptions about water chemistry.
- Devise a means of accounting for the effect of wind and include it in the model.

Additional model calculations are also desirable, some doable with the current program and others that would require model improvements. Important studies that have not yet been done include:

- Calculate seasonal gas flows through Yucca Mountain.
- Run one or more benchmark problems on both TGIF and the multi-phase flow simulator TOUGH [Pruess, 1987].
- Run cases with higher temperatures and more realistic temperature fields, using an improved version of the model.
- Use a version that couples heat transfer and gas flow to predict repository temperatures over time.
- Compare model predictions with measured gas flows at Yucca Mountain, Apache Leap, or elsewhere.

As more information is collected to characterize the Yucca Mountain site, the TGIF model can be used to provide improved predictions of gas flow and carbon-14 migration. In either current or improved versions, the model will be a sensitive and flexible tool for predicting repository performance.

APPENDIX A

FLOW DRIVEN BY BINARY DIFFUSION

In the presence of a temperature gradient in the subsurface, there is a partial pressure gradient of water vapor because relative humidity in the deep subsurface is always close to 100%. Because the total pressure is approximately uniform [Ross, 1984], there will be a partial pressure gradient of the other components of air (referred to here as "dry air") in the opposite direction.

Evaporation and condensation will provide a source or sink of water vapor to maintain a steady-state diffusive flow. However, the countervailing diffusion of air requires a return flow to maintain a constant partial pressure. Consequently, a mass flow of air from higher to lower temperatures will be driven by this diffusion mechanism. This flow can be neglected because it is smaller than the temperature-driven flow.

To show this, one observes that the diffusion-driven mass flow of dry air, which is approximately equal to the total diffusion-driven flow, is equal in magnitude to the diffusion flux. The volumetric gas flux due to diffusion q_d is

$$q_d = \tau D n_D \gamma \frac{1}{P} \frac{dP_v}{dT}$$

where τ is the tortuosity, D is the diffusion constant, n_D is the drained porosity, γ is the temperature gradient, and $\frac{1}{P}\frac{dP_v}{dT}$ is the temperature derivative of the partial pressure of saturated water vapor as a fraction of ambient pressure.

Under ambient conditions, the temperature gradient is 2×10^{-4} K/cm. The derivative $\frac{1}{P}\frac{dP_v}{dT}$ is equal to about 2.2×10^{-3} K^{-1} at 30°C [Weast, 1986]. Using a typical tortuosity of 0.1, a molecular diffusion constant for water vapor into air, corrected to ambient temperature and pressure, of 1000 m^2/yr [Weast, 1986], and a drained porosity of 0.05, a gas flux of about 4×10^{-10} cm/sec is obtained. This is negligible compared to the temperature-driven flow. Redoing the calculation at any of the higher temperatures considered in this analysis would not change this conclusion.

At yet higher temperatures, like those considered by Tsang and Pruess [1987], dP_v/dT may become large enough to make diffusion-driven flow important. At such temperatures, the model presented would become inapplicable and a model that explicitly considers diffusion (such as that of Tsang and Pruess) must be used.

APPENDIX B
UNSATURATED FRACTURED TUFF TREATED AS A HOMOGENEOUS POROUS MEDIUM

In the unsaturated fractured tuffs of Yucca Mountain, the permeability to gas associated with the fractures far exceeds the permeability of the unfractured rock matrix, even though the drained porosity of the matrix is well in excess of the fracture porosity. Consequently, the mass flow of air in response to a pressure gradient will proceed almost entirely through the fractures, and the air in the drained matrix pores may be thought of as stagnant.

In such situations, it is common to conceive of the seepage velocity of the gas flow as being equal to the Darcy velocity or mass flux divided by the fracture porosity. (See, for example, Tsang and Pruess [1987]). This is, after all, the average velocity that would be measured if one were somehow to install miniature wind gauges in the fractures. It is well established, however, that the velocity of movement of a contaminant borne by a fluid through a fractured porous medium can be less than the seepage velocity in the fractures because of the phenomenon of "matrix diffusion." In this process, molecules or ions of the contaminant species diffuse out of the moving fracture fluid into the stagnant pores of the matrix, there to remain immobile until they diffuse back into the fractures.

In the extreme case of matrix diffusion, diffusive transfer between fractures and matrix is so rapid compared to the transport in the fractures that the concentration of contaminant everywhere in the matrix pores is the same as in the adjoining fractures. Computations of contaminant transport can then be carried out by ignoring the distinction between fractures and matrix pores, so that the seepage velocity is defined as the mass flux divided by the total porosity and the contaminant velocity is equal to the seepage velocity [de Marsily, 1986, p. 245]. The purpose of this appendix is to demonstrate the applicability of this description to the movement of carbon-14 in the gas phase at Yucca Mountain.

To analyze this question, we take advantage of previous work on matrix diffusion in saturated rocks. Mathematical results from studies of the saturated zone may be adapted to our situation by noting that liquid-phase advection and diffusion are both much slower than the same processes in the gas phase. Carbon-14 in dissolved bicarbonate can therefore be

treated as completely immobile, allowing a mathematical analogy to species sorbed on the rock. If the ratio of gas-phase to liquid-phase concentrations is constant (as would be the case if total carbon dioxide and bicarbonate concentrations remained constant as carbon-14 moved through a system, or even with changing concentrations of CO_2 if pH were held constant by a buffer and the solution were undersaturated with respect to calcite), the governing equations are identical to those generally used to analyze matrix diffusion with adsorption. While these chemical assumptions may be somewhat unrealistic, they are no more so than the assumptions underlying the analogous postulate of a constant ratio of dissolved to sorbed concentration, which is commonly used to analyze saturated-zone transport.

Published analyses of the saturated-zone problem have addressed two somewhat different situations which are both relevant to our concerns. These situations differ in the time dependence of the source of contamination. Neretnieks [1981] studied the migration of dissolved natural carbon-14 in fractured porous rocks. The carbon-14 concentration at the source is constant. This is analogous to the interpretation of existing carbon-14 concentrations under ambient conditions at Yucca Mountain. Rasmuson and Neretnieks [1981] studied the migration of non-decaying contaminants with a square-wave input (that is, a concentration at the source which changes instantaneously from zero to a constant value and later returns instantaneously to zero). The solution to this problem can be applied directly to decaying contaminants if the source concentration undergoes radioactive decay. (This may be confirmed by substituting $C_{nd} = Ce^{\lambda t}$ into the solute transport equation with radioactive decay.) This formulation is applicable to the migration of carbon-14 from the repository to the surface, because the source is an initial inventory of carbon-14 which undergoes radioactive decay.

For the case of the contaminant which does not decay, or whose source undergoes radioactive decay, Rasmuson and Neretnieks define a dimensionless group δ which represents the ratio of the time for fluid to flow from source to outlet to the time for an unsorbed contaminant to diffuse to the center of a matrix block. This group is, in our notation

$$\delta = \frac{12\tau D n_D L}{q s^2} \qquad \text{(B-1)}$$

where s is the fracture spacing. (Note that this formulation requires substitution of Rasmuson and Neretnieks' Eq. (42), the relationship between seepage and Darcy velocity, and the assumption that fracture porosity is much less than drained porosity into the definition of δ in the Rasmuson and Neretnieks paper.)

If δ is much greater than unity, the fractures and matrix pores will be well mixed. This condition may be written as

$$s^2 >> \frac{12\tau D n_D L}{q} \tag{B-2}$$

We may adopt the values $\tau = 0.1$ and $D = 500$ m^2/yr. The quantity $n_D L/q$ is the gas travel time, which we give a range of 10 to 1000 yr based on results in Chapters 5 and 6. Equation (B-2) then gives the threshold fracture spacing, below which the gas phase will be well mixed, as between 80 and 800 m, with smaller values corresponding to faster gas travel. One can surely assume that the fracture spacing in the welded tuffs is less than 80 m. Furthermore, if the gas travel time is below 10 yr, escape of carbon-14 will be so rapid that details of fracture-matrix interactions will be of little importance. Thus the assumption of complete mixing is well supported.

In the case of a constant source, Neretnieks [1981] shows that the ratio of apparent carbon-14 age t_a to the travel time of fluid through fractures t_f is

$$\frac{t_a}{t_f} = 1 + \frac{\left[n_D - n_f\right]\left[2A-1\right]}{n_f p} \tag{B-3}$$

where

$$A = \frac{e^p}{e^p + e^{-p}} \tag{B-4}$$

$$p = \frac{s}{2}\left[\frac{\lambda}{D\tau}\right]^{1/2} \tag{B-5}$$

n_f is the fracture porosity, and λ is the radioactive decay constant, equal to the natural logarithm of 2 divided by the half-life.

The behavior of Eq. (B-3) is that for large p, or large fracture spacing s, the ratio approaches a constant (not necessarily 1 because $n_f s$ is constant for a given fracture aperture). For small fracture spacings, as will be shown below, the ratio (B-3) approaches n_D/n_f, and the apparent carbon-14 age will be equal to the fluid travel time calculated as in this report, using the drained porosity of both fractures and matrix as the effective porosity. We will now calculate how small s must be for this to be a good approximation.

Expanding the exponentials of (B-4) in power series, one obtains after a bit of manipulation

$$A = \frac{1}{2}\left[1 + p - \frac{1}{3}p^3 + O(p^5)\right] \tag{B-6}$$

Substituting this into (B-3) yields

$$\frac{t_a}{t_f} = 1 + \frac{n_D - n_f}{n_f}\left[1 - \frac{1}{3}p^2 + O(p^4)\right] \tag{B-6}$$

Therefore the condition for $t_a/t_f \approx n_D/n_f$ is

$$\frac{1}{3}p^2 << 1 \tag{B-8}$$

or

$$\frac{s^2\lambda}{12D\tau} << 1 \tag{B-9}$$

It is remarkable that this formula is identical to Eq. (B-2), with the decay time λ^{-1} substituted for the travel time $n_D L/q$.

Before applying this formula, we note that the derivation of Eq. (B-3) by Neretnieks [1981] assumed no sorption. If a retardation factor B is introduced into Neretnieks' governing equations, and the term representing radioactive decay in the fracture is dropped (easily justified under the conditions of interest to us, where most of the carbon-14 is in the

matrix), one obtains a set of equations and boundary conditions identical to Neretnieks', with the substitutions of Cp/B for the pore concentration Cp and λB for λ. Only the latter variable appears in the solution. Making the replacement in Eq. (B-9) gives

$$\frac{s^2 \lambda B}{12 D \tau} << 1 \qquad \text{(B-10)}$$

or

$$s^2 << \frac{12\ D\tau}{\lambda B} \qquad \text{(B-11)}$$

Substituting the value $\lambda = 1.21 \times 10^{-4}$ and a range of B from 10 to 1000 gives the condition that s be less than a number between 70 m and 2200 m. Again, this is a safe assumption.

We conclude that the assumption of complete mixing of carbon species between fractures and pores may safely be made for all conditions of interest.

APPENDIX C
COMPARISON OF VOLUME BALANCE EQUATION WITH MASS BALANCE EQUATION USING VIRTUAL TEMPERATURE

Another approach that has been used to model subsurface gas flow is based on the concept of the "virtual temperature," which is the temperature at which dry air would have the density that humid air has at the actual temperature. The density is expressed in terms of the pressure and virtual temperature, which is related to the actual temperature by a straightforward formula. Density differences drive flow in the same way as in our model.

In comparing the two approaches, we will focus on a model developed by Kipp [1987]. We will begin by rewriting Kipp's balance equation in terms of pressure and true temperature. The two equations can then be compared term by term.

To do this, we must relate the virtual temperature T' to the true temperature T. We first use the definition of virtual temperature [Kipp's Eq. (3)],

$$\rho = \frac{P\Omega_a}{RT'} \tag{C-1}$$

where the remainder of the notation is taken from Chapter 2. Comparing this to our own formula for density, Eq. (2-1), gives

$$\frac{P\Omega_a}{RT'} = \frac{1}{RT}\left[P_v\Omega_v + (P-P_v)\Omega_a\right] \tag{C-2}$$

A little manipulation puts this in the form

$$T' = \frac{T}{1 - \frac{P_v}{P}\left[1 - \frac{\Omega_v}{\Omega_a}\right]} \tag{C-3}$$

from which we obtain

$$\nabla T' = \nabla T\left[\frac{1}{1 - \frac{P_v}{P}\left[1 - \frac{\Omega_v}{\Omega_a}\right]} + \frac{T\frac{dP_v}{dT}\frac{1}{P}\left[1-\frac{\Omega_v}{\Omega_a}\right]}{\left[1-\frac{P_v}{P}\left[1-\frac{\Omega_v}{\Omega_a}\right]\right]^2}\right] \tag{C-4}$$

Now Kipp's model is based on a mass balance rather than a volume balance. The gas balance equation in Kipp's paper [his Eq. (1)], written for steady state, can be expressed as

$$\nabla \cdot (\rho \mathbf{q}) = 0 \tag{C-5}$$

or

$$\nabla \cdot \mathbf{q} + \frac{\nabla \rho}{\rho} \cdot \mathbf{q} = 0 \tag{C-6}$$

Because by Equation (C-1) the density can be expressed as a function only of pressure and virtual temperature, we can expand the density gradient to make the balance equation

$$\nabla \cdot \mathbf{q} + \frac{1}{P} \nabla P \cdot \mathbf{q} - \frac{1}{T'} \nabla T' \cdot \mathbf{q} = 0 \tag{C-7}$$

Substituting equations (C-3) and (C-4) puts this in terms of P and T:

$$\nabla \cdot \mathbf{q} + \frac{1}{P} \nabla P \cdot \mathbf{q} - \left[\frac{1}{T} + \frac{\frac{dP_v}{dT} \left[1 - \frac{\Omega_v}{\Omega_a} \right]}{P - P_v \left[1 - \frac{\Omega_v}{\Omega_a} \right]} \right] \nabla T \cdot \mathbf{q} = 0 \tag{C-8}$$

This can now be compared with the balance equation (2-8) derived in Chapter 2, which is

$$\nabla \cdot \mathbf{q} + \frac{1}{P - P_v} \nabla P \cdot \mathbf{q} - \left[\frac{1}{T} + \frac{1}{P - P_v} \frac{dP_v}{dT} \right] \nabla T \cdot \mathbf{q} = 0 \tag{C-9}$$

At temperatures around 30°C the ∇T terms in the two formulas differ by about 25% and the ∇P terms differ by about 4%.

Unless Kipp's model includes additional terms not discussed in his paper, it would appear that Kipp's mass balance does not account for evaporation and condensation in the same way as our model.

APPENDIX D
RIB AND SEPDB INFORMATION

Information from the Reference Information Base used in this Report.

This report contains no information from the Reference Information Base.

Candidate information for the Reference Information Base.

This report contains no candidate information for the Reference Information Base.

Candidate information for the Site & Engineering Properties Data Base.

This report contains no candidate information for the Site and Engineering Properties Data Base.

REFERENCES

Bear, J. *Hydraulics of Groundwater*, McGraw-Hill, New York, 1979. (NAA.890906.0184)

Bear, J. and A. Verruijt, *Modeling Groundwater Flow and Pollution*, D. Reidel, Dordrecht, 1987. (NNA.900212.0003)

Davies, P.B., Modeling a real, variable-density, ground-water flow - analysis of potentially significant errors, in Proceedings of the Solving Ground Water Problems with Models Conference and Exposition, Denver, February 10-12, 1987, pp. 888-903. (NNA.910429.0155)

De Marsily, G., *Quantitative Hydrogeology*, Academic Press, Orlando, FL, 1986. (NNA.910207.0116)

Doctor, P.G., Sensitivity and uncertainty analyses for performance assessment modeling, *Eng. Geol.*, 26, pp. 411-429, 1989. (NNA.910306.0123)

Donn, W.L., *Meteorology*, 4th edition, McGraw Hill, New York, 1975. (Chapter 3.) (NNA.911024.0074)

Doughty, C., and K. Pruess, A similarity solution for two-phase fluid and heat flow near high-level nuclear waste packages emplaced in porous media, *Int. J. Heat Mass Transfer, 33*, 1205-1222 (1990). (NNA.910328.0083)

Freeze, R.A. and J.A. Cherry, *Groundwater*, Prentice-Hall, Englewood Cliffs, N.J., 1979. (NNA.870406.0444)

Frind, E.O., Simulation of long-term transient density-dependent transport in groundwater, *Adv. Water Resources, 5*, 73-88 (1982). (NNA.910522.0055)

Huyakorn, P.S. and C. Taylor, Finite element models for coupled groundwater and convective dispersion. Proceedings of the 1st International Conference on Finite Elements in Water Resources, pp. 1.131-1.151, Pentech Press, London, 1976 (NNA.910523.0004)

Huyakorn, P.S., Andersen, J.W. Mercer, and H.O. White, Jr., Saltwater intrusion in aquifers: development and testing of a three-dimensional finite element model, *Water Resour. Res., 23*, 293-312 (1987). (NNA.910523.0012)

Kipp, K.L., Jr., Effect of topgraphy on gas flow in unsaturated fractured rock: numerical simulation, in *Flow and Transport Through Unsaturated Fractured Rock*, edited by D.D. Evans and T.J. Nicholson, Geophysical Monograph 42, American Geophysical Union, Washington, 1987, pp. 171-176. (HQS.880517.3117)

Lide, D.R., ed., *CRC Handbook of Chemistry and Physics*, 71st ed., CRC Press, Boca Raton, FL, 1990. (NNA.901127.0187)

Lusczynski, N.J., Head and flow of water of variable density, *J. Geophys. Res., 66*, 4247-4256 (1961). (NNA.910523.0013)

Montazer, P., E.P. Weeks, F. Thamir, S.M. Yard, and P.B. Hofrichter, Monitoring the vadose zone in fractured tuff, Yucca Mountain, Nevada, in Proceedings of the NWWA Conference on Characterization and Monitoring of the Vadose (Unsaturated) Zone, Denver, November 19-21, 1985, pp. 439-469. (HQS.880517.1797)

Montazer, P. and W.E. Wilson, Conceptual hydrological model of flow in the unsaturated zone, Yucca Mountain, Nevada, USGS Water-Resources Investigations Report 84-4345, 1984. (NNA.890327.0051)

Neretnieks, I., Age dating of groundwater in fissured rock: influence of water volume in micropores, *Water Resour. Res., 17*, 421-422 (1981). (NNA.910523.0014)

Pollock, D.W., Semianalytical computation of path lines for finite-difference models, *Ground Water, 26*, 743-750 (1988). (NNA.901005.0042)

Pollock, D.W., Documentation of computer programs to compute and display pathlines using results from the U.S. Geological Survey modular three-dimensional finite-difference groundwater flow model, U.S. Geological Survey, Open File Report 89-381, 1989. (NNA.910701.0093)

Pruess, K., TOUGH User's Guide, U.S. Nuclear Regulatory Commission Report NUREG/CR-4645 (1987). (NNA.890315.0010)

Rasmuson, A., and I. Neretnieks, Migration of radionuclides in fissured rock: the influence of micropore diffusion and longitudinal dispersion, *J. Geophys. Res., 86*, 3749-58 (1981). (NNA.870728.0020)

Ross, B., A conceptual model of deep unsaturated zones with negligible recharge, *Water Resour. Res., 20*, 1627-1629 (1984). (HQS.880517.1832)

Ross, B., Gas-phase transport of carbon-14 released from nuclear waste into the unsaturated zone, in *Scientific Basis for Nuclear Waste Management XI*, edited by M.J. Apted and R.E. Westerman, Materials Research Society, Pittsburgh, 1988, pp. 273-284. (NNA.901005.0035)

Scott, R.B., and J. Bonk, Preliminary geologic map of Yucca Mountain, Nye County, Nevada, with geologic sections, U.S. Geological Survey Open-File Report 84-494, Denver, CO, 1984. (HQS.880517.1443)

Shafer, J.M., Reverse pathline calculation of time-related capture zones in nonuniform flow, *Ground Water, 25*, 283-289 (1987). (NNA.910523.0015)

Striegl, R.G., Geochemical interactions that influence the transport of 14-carbon dioxide in the unsaturated zone, *Eos Trans. AGU, 69*, 1216 (1988). (NNA.910523.0016)

Thorstenson, D.C., The composition and CO2 carbon isotope signature of gases from Borehole USW UZ-6, Yucca Mountain, Nevada, presented to Workshop on Unsaturated Flow and Transport, Tucson, January 1991. (NNA.911004.0004)

Tsang, C.-F., Coupled processes, presented to Workshop on Unsaturated Flow and Transport, Tucson, January 1991. (NNA.911004.0003)

Tsang, Y.W. and K. Pruess, A study of thermally induced convection near a high-level nuclear waste repository in partially saturated fractured tuff, *Water Resources Research, 23*, 1958-1966 (1987). (NNA.890522.0273)

Wang, H.F., and M.P. Anderson, *Introduction to Groundwater Modeling*, W.H. Freeman, New York, 1982. (NNA.910620.0121)

Weeks, E.P., Effect of topography on gas flow in unsaturated fractured rock--concepts and observations, in *Flow and Transport Through Unsaturated Fractured Rock*, edited by D.D. Evans and T.J. Nicholson, Geophysical Monograph 42, American Geophysical Union, Washington, 1987, pp. 165-170. (HQS.880517.3214)

Yang, I.C., H.H. Hess, E.P. Weeks, and D.C. Thorstenson, Analysis of gaseous-phase stable and radioactive isotopes in the unsaturated zone, Yucca Mountain, Nevada, in Proceedings of the NWWA Conference on Characterization and Monitoring of the Vadose (Unsaturated) Zone, Denver, November 1985, pp. 488-506. (HQS.880517.1880)

Yang, I.C., A.K. Turner, T.M. Sayre, and P. Montazer, Triaxial-compression extraction of pore water from unsaturated tuff, Yucca Mountain, Nevada, U.S. Geological Survey Water-Resources Investigations Report 88-4189, 1988. (NNA.890309.0161)

DISTRIBUTION LIST

1 J. W. Bartlett, Director (RW-1)
Office of Civilian Radioactive Waste Management
U.S. Department of Energy
1000 Independence Avenue, S.W.
Washington, DC 20585

1 F. G. Peters, Deputy Director (RW-2)
Office of Civilian Radioactive Waste Management
U.S. Department of Energy
1000 Independence Avenue, S.W.
Washington, DC 20585

1 T. H. Isaacs (RW-4)
Office of Strategic Planning and International Programs
Office of Civilian Radioactive Waste Management
U.S. Department of Energy
1000 Independence Avenue, S.W.
Washington, DC 20585

1 J. D. Saltzman (RW-5)
Office of External Relations
Office of Civilian Radioactive Waste Management
U.S. Department of Energy
1000 Independence Avenue, S.W.
Washington, DC 20585

1 Samuel Rousso (RW-10)
Office of Program and Resources Management
Office of Civilian Radioactive Waste Management
U.S. Department of Energy
1000 Independence Avenue, S.W.
Washington, DC 20585

1 J. C. Bresee (RW-10)
Office of Civilian Radioactive Waste Management
U.S. Department of Energy
1000 Independence Avenue, S.W.
Washington, DC 20585

1 C. P. Gertz (RW-20)
Office of Geologic Disposal
Office of Civilian Radioactive Waste Management
U.S. Department of Energy
1000 Independence Avenue, S.W.
Washington, DC 20585

1 S. J. Brocoum (RW-22)
Analysis and Verification Division
Office of Civilian Radioactive Waste Management
U.S. Department of Energy
1000 Independence Avenue, S.W.
Washington, DC 20585

1 D. D. Shelor (RW-30)
Office of Systems and Compliance
Office of Civilian Radioactive Waste Management
U.S. Department of Energy
1000 Independence Avenue, S.W.
Washington, DC 20585

1 J. Roberts (RW-33)
Office of Civilian Radioactive Waste Management
U.S. Department of Energy
1000 Independence Avenue, S.W.
Washington, DC 20585

1 G. J. Parker (RW-332)
Office of Civilian Radioactive Waste Management
U.S. Department of Energy
1000 Independence Avenue, S.W.
Washington, DC 20585

1 Associate Director (RW-40)
Office of Storage and Transportation
Office of Civilian Radioactive Waste Management
U.S. Department of Energy
1000 Independence Avenue, S.W.
Washington, DC 20585

1 Associate Director (RW-50)
Office of Contract Business Management
Office of Civilian Radioactive Waste Management
U.S. Department of Energy
1000 Independence Avenue, S.W.
Washington, DC 20585

1 C. G. Russomanno (RW-52)
Office of Civilian Radioactive Waste Management
U.S. Department of Energy
1000 Independence Avenue, S.W.
Washington, DC 20585

1 D. U. Deere, Chairman
Nuclear Waste Technical Review Board
1100 Wilson Blvd. #910
Arlington, VA 22209-2297

1 Dr. John E. Cantlon
Nuclear Waste Technical Review Board
1795 Bramble Dr.
East Lansing, MI 48823

1 Dr. Melvin W. Carter
Nuclear Waste Technical Review Board
4621 Ellisbury Dr., N.E.
Atlanta, GA 30332

1 Dr. Donald Langmuir
Nuclear Waste Technical Review Board
109 So. Lookout Mountain Cr.
Golden, CO 80401

1 Dr. D. Warner North
Nuclear Waste Technical Review Board
Decision Focus, Inc.
4984 El Camino Real
Los Altos, CA 94062

1 Dr. Dennis L. Price
Nuclear Waste Technical Review Board
1011 Evergreen Way
Blacksburg, VA 24060

1 Dr. Ellis D. Verink
Nuclear Waste Technical Review Board
4401 N.W. 18th Place
Gainesville, FL 32605

5 C. P. Gertz, Project Manager
Yucca Mountain Project Office
U.S. Department of Energy
P.O. Box 98608—MS 523
Las Vegas, NV 89193-8608

1 C. L. West, Director
Office of External Affairs
DOE Field Office, Nevada
U.S. Department of Energy
P.O. Box 98518
Las Vegas, NV 89193-8518

12 Technical Information Officer
DOE Field Office, Nevada
U.S. Department of Energy
P.O. Box 98518
Las Vegas, NV 89193-8518

1 P. K. Fitzsimmons, Director
Health Physics and Environmental Division
DOE Field Office, Nevada
U.S. Department of Energy
P.O. Box 98518
Las Vegas, NV 89193-8518

1 D. R. Elle, Director
Environmental Protection Division
DOE Field Office, Nevada
U.S. Department of Energy
P.O. Box 98518
Las Vegas, NV 89193-8518

1 Repository Licensing and Quality Assurance Project Directorate
Division of Waste Management
U.S. Nuclear Regulatory Commission
Washington, DC 20555

1 Senior Project Manager for Yucca Mountain Repository Project Branch
Division of Waste Management
U.S. Nuclear Regulatory Commission
Washington, DC 20555

1 NRC Document Control Desk
Division of Waste Management
U.S. Nuclear Regulatory Commission
Washington, DC 20555

1 P. T. Prestholt
NRC Site Representative
301 E. Stewart Ave.
Las Vegas, NV 89101

1 E. P. Binnall
Field Systems Group Leader
Building 50B/4235
Lawrence Berkeley Laboratory
Berkeley, CA 94720

1 Center for Nuclear Waste Regulatory Analyses
6220 Culebra Road
Drawer 28510
San Antonio, TX 78284

3 L. J. Jardine
Technical Project Officer for YMP
Lawrence Livermore National Laboratory
Mail Stop L-204
P.O. Box 808
Livermore, CA 94550

4 R. J. Herbst
Technical Project Officer for YMP
Los Alamos National Laboratory
N-5, Mail Stop J521
P.O. Box 1663
Los Alamos, NM 87545

1 H. N. Kalia
Exploratory Shaft Test Manager
Los Alamos National Laboratory
Mail Stop 527
101 Convention Center Dr.
Suite 820
Las Vegas, NV 89109

1 J. F. Divine
Assistant Director for Engineering Geology
U.S. Geological Survey
106 National Center
12201 Sunrise Valley Dr.
Reston, VA 22092

6 L. R. Hayes
Technical Project Officer
Yucca Mountain Project Branch—MS 425
U.S. Geological Survey
P.O. Box 25046
Denver, CO 80225

1 V. R. Schneider
Asst. Chief Hydrologist—MS 414
Office of Program Coordination and Technical Support
U.S. Geological Survey
12201 Sunrise Valley Dr.
Reston, VA 22092

1 R. B. Raup, Jr.
Geological Division Coordinator
Mail Stop 913
Yucca Mountain Project
U.S. Geological Survey
P.O. Box 25046
Denver, CO 80225

1 D. H. Appel, Chief
Hydrologic Investigations Program
Mail Stop 421
U.S. Geological Survey
P.O. Box 25046
Denver, CO 80225

1 E. J. Helley
Branch of Western Regional Geology
Mail Stop 427
U.S. Geological Survey
345 Middlefield Road
Menlo Park, CA 94025

1 Chief
Nevada Operations Office
U.S. Geological Survey
101 Convention Center Dr.
Suite 860, MS 509
Las Vegas, NV 89109

1 D. Zesiger
U.S. Geological Survey
101 Convention Center Dr.
Suite 860, MS 509
Las Vegas, NV 89109

1 R. V. Watkins, Chief
Project Planning and Management
U.S. Geological Survey
P.O. Box 25046
421 Federal Center
Denver, CO 80225

1 A. L. Flint
U.S. Geological Survey
Mail Stop 721
P.O. Box 327
Mercury, NV 89023

1 D. A. Beck
U.S. Geological Survey
1500 E. Tropicana, Suite 201
Las Vegas, NV 89119

1 P. A. Glancy
U.S. Geological Survey
Federal Building, Room 224
Carson City, NV 89701

1 Sherman S. C. Wu
Branch of Astrogeology
U.S. Geological Survey
2255 N. Gemini Dr.
Flagstaff, AZ 86001

1 J. H. Sass
Branch of Tectonophysics
U.S. Geological Survey
2255 N. Gemini Dr.
Flagstaff, AZ 86001

1 DeWayne A. Campbell
Technical Project Officer for YMP
Bureau of Reclamation
Code D-3790
P.O. Box 25007
Denver, CO 80225

1 K. W. Causseaux
NHP Reports Chief
U.S. Geological Survey
421 Federal Center
P.O. Box 25046
Denver, CO 80225

1 V. M. Glanzman
U.S. Geological Survey
913 Federal Center
P.O. Box 25046
Denver, CO 80225

1 J. H. Nelson
Technical Project Officer for YMP
Science Applications International Corp.
101 Convention Center Dr.
Suite 407
Las Vegas, NV 89109

2 SAIC-T&MSS Library
Science Applications International Corp.
101 Convention Center Dr.
Suite 407
Las Vegas, NV 89109

1 Elaine Ezra
YMP GIS Project Manager
EG&G Energy Measurements, Inc.
Mail Stop D-12
P.O. Box 1912
Las Vegas, NV 89125

1 R. E. Jackson, Program Manager
Roy F. Weston, Inc.
955 L'Enfant Plaza, S.W.
Washington, DC 20024

1 Technical Information Center
Roy F. Weston, Inc.
955 L'Enfant Plaza, S.W.
Washington, DC 20024

1 D. Hedges, Vice President
Quality Assurance
Roy F. Weston, Inc.
4425 Spring Mountain Rd., Suite 300
Las Vegas, NV 89102

1 D. L. Fraser, General Manager
Reynolds Electrical & Engineering Co.
Mail Stop 555
P.O. Box 98521
Las Vegas, NV 89193-8521

1 R. F. Pritchett
Technical Project Officer for YMP
Reynolds Electrical & Engineering Co.
Mail Stop 408
P.O. Box 98521
Las Vegas, NV 89193-8521

1 B. W. Colston
General Manager and President
Las Vegas Branch
Raytheon Services Nevada
Mail Stop 416
P.O. Box 95487
Las Vegas, NV 89193-5487

1 R. L. Bullock
Technical Project Officer for YMP
Raytheon Services Nevada
Suite P250, Mail Stop 403
101 Convention Center Dr.
Las Vegas, NV 89109

1 R. E. Lowder
Technical Project Officer for YMP
MAC Technical Services
101 Convention Center Dr.
Suite 1100
Las Vegas, NV 89109

1 C. K. Hastings, Manager
PASS Program
Pacific Northwest Laboratories
P.O. Box 999
Richland, WA 99352

1 A. T. Tamura
Science and Technology Division
Office of Scientific and Technical Information
U.S. Department of Energy
P.O. Box 62
Oak Ridge, TN 37831

1 Carlos G. Bell, Jr.
Professor of Civil Engineering
Civil and Mechanical Engineering Department
University of Nevada, Las Vegas
4505 South Maryland Parkway
Las Vegas, NV 89154

1 C. F. Costa, Director
Nuclear Radiation Assessment Division
U.S. Environmental Protection Agency
Environmental Monitoring Systems Laboratory
P.O. Box 93478
Las Vegas, NV 89193-3478

1 ONWI Library
Battelle Columbus Laboratory
Office of Nuclear Waste Isolation
505 King Avenue
Columbus, OH 43201

1 T. Hay, Executive Assistant
Office of the Governor
State of Nevada
Capitol Complex
Carson City, NV 89710

3 R. R. Loux, Jr.
Executive Director
Nuclear Waste Project Office
State of Nevada
Evergreen Center, Suite 252
1802 North Carson Street
Carson City, NV 89701

1 C. H. Johnson
Technical Program Manager
Nuclear Waste Project Office
State of Nevada
Evergreen Center, Suite 252
1802 North Carson Street
Carson City, NV 89710

1 John Fordham
Water Resources Center
Desert Research Institute
P.O. Box 60220
Reno, NV 89506

1 Dr. Martin Mifflin
Water Resources Center
Desert Research Institute
2505 Chandler Avenue
Suite 1
Las Vegas, NV 89120

1 Eric Anderson
Mountain West Research-Southwest, Inc.
2901 N. Central Ave. #1000
Phoenix, AZ 85012-2730

1 Department of Comprehensive Planning
Clark County
225 Bridger Avenue, 7th Floor
Las Vegas, NV 89155

1 Planning Department
Nye County
P.O. Box 153
Tonopah, NV 89049

1 Lincoln County Commission
Lincoln County
P.O. Box 90
Pioche, NV 89043

5 Judy Foremaster
City of Caliente
P.O. Box 158
Caliente, NV 89008

1 Economic Development Department
City of Las Vegas
400 East Stewart Avenue
Las Vegas, NV 89101

1 Community Planning and Development
City of North Las Vegas
P.O. Box 4086
North Las Vegas, NV 89030

1 Director of Community Planning
City of Boulder City
P.O. Box 367
Boulder City, NV 89005

1 Commission of the European Communities
200 Rue de la Loi
B-1049 Brussels
BELGIUM

2 M. J. Dorsey, Librarian
YMP Research and Study Center
Reynolds Electrical & Engineering Co., Inc.
Mail Stop 407
P.O. Box 98521
Las Vegas, NV 89193-8521

1 Amy Anderson
Argonne National Laboratory
Building 362
9700 So. Cass Ave.
Argonne, IL 60439

2 L. D. Foust
Nevada Site Manager
TRW Environmental Safety Systems
101 Convention Center Dr.
Suite 540—MS 423
Las Vegas, NV 89109

25 Benjamin Ross
Disposal Safety, Inc.
1660 L Street NW, Suite 314
Washington, DC 20036

1 Claudio Pescatore
Brookhaven National Laboratory
Department of Nuclear Energy
Upton, NY 11973

1 Karsten Pruess
Lawrence Berkeley Laboratory
Building 50E
1 Cyclotron Road
Berkeley, CA 94720

1 Larry Rickertsen
Roy F. Weston, Inc.
955 L'Enfant Plaza, S.W.
Washington, DC 20024

1 Richard Codell
U. S. Nuclear Regulatory Commission
Mail Stop 4H3
Washington, DC 20555

1 Leon Reiter
U. S. Nuclear Waste Technical Review Board
1100 Wilson Blvd., Suite 910
Arlington, VA 22209

1 R. K. McGuire
Risk Engineering, Inc.
5255 Pine Ridge Road
Golden, CO 80403

1 Ian Miller
Golder Associates Inc.
4104 148th Avenue, N.E.
Redmond, WA 98052

1 Bill Wilson
U. S. Geological Survey
Federal Center, MS 425
P. O. Box 25046
Lakewood, CO 80225

1 Christine Doughty
Lawrence Berkeley Laboratory
Building 50E
1 Cyclotron Road
Berkeley, CA 94720

1 Dan Fehringer
U. S. Nuclear Regulatory Commission
Mail Stop 4H3
Washington, DC 20555

1 Janet Herman
Department of Environmental Science
University of Virginia
2565 Wyngate Road
Charlottesville, VA 22901

1 Dwight Hoxie
U. S. Geological Survey
Federal Center, MS 425
P. O. Box 25046
Lakewood, CO 80225

1 W. W.-L. Lee
Department of Nuclear Engineering
University of California
Berkeley, CA 94720

1 Donald R. Nielsen
LAWR Veihmeyer Hall
University of California
Davis, CA 95616

1 John Nitao
Lawrence Livermore National Laboratory
Mail Stop L-206
P. O. Box 808
Livermore, CA 94551

1 Thomas H. Pigford
Department of Nuclear Engineering
University of California
Berkeley, CA 94720

1 Yvonne Tsang
Lawrence Berkeley Laboratory
Building 50E
1 Cyclotron Road
Berkeley, CA 94720

1 Richard Van Konynenburg
Lawrence Livermore National Laboratory
P. O. Box 808
Livermore, CA 94551

1 Ed Weeks
U. S. Geological Survey
Federal Center, MS 413
P. O. Box 25046
Lakewood, CO 80225

1 Paul Eslinger
Pacific Northwest Laboratories
P. O. Box 999
Richland, WA 99352

1 Lee Plansky
Pacific Northwest Laboratories
Sigma III Building
P. O. Box 999
Richland, WA 99352

1 Jim Buelt
Pacific Northwest Laboratories
P. O. Box 999
Richland, WA 99352

1 Mark Reeves
Intera, Inc.
6850 Austin Center Blvd., Suite 300
Austin, TX 78731

1 Leo E. Thompson
Pacific Northwest Laboratories
In Situ Vitrification Integrated Program
P. O. Box 999
Richland, WA 99352

1 Örjan Hedenberg
STFI
Drottningkristinasväg 61
Box 5604
S-11486 Stockholm
SWEDEN

1 W. C. Morgan
Pacific Northwest Laboratories
Mail Stop P8-10
P. O. Box 999
Richland, WA 99352

1 Richard R. Parizek
Department of Geosciences
340 Deike Building
Pennsylvania State University
University Park, PA 16802

1 Vern Rogers
Rogers & Associates Engineering
515 East 4500 South
P. O. Box 330
Salt Lake City, UT 84110

1 Frits van Dorp
NAGRA
Hardstraße 73
CH-5430 Wettingen
SWITZERLAND

1 Sam Worcester
Associate Dean for Research and Graduate Study
Montana Tech
Butte, MT 59701

1 Wei-xing Guo
Department of Geosciences
Pennsylvania State University
University Park, PA 16802

1 Mark White
Pacific Northwest Laboratories
P. O. Box 999
Richland, WA 99352

1 U-S. Park
Science Applications International Corp.
101 Convention Center Dr.
Las Vegas, NV 89109

1 Scott Sinnock
NWMS M & O
101 Convention Center Dr.
Phase II, Suite P110
Las Vegas, NV 89109

5	3141	S. A. Landenberger
8	3145	Document Processing for DOE/OSTI
3	3151	G. C. Claycomb
1	6300	T. O. Hunter
1	6310	T. E. Blejwas, Actg.
1	6312	F. W. Bingham
1	6312	R. W. Barnard
1	6312	G. E. Barr
1	6312	W. F. Chambers
1	6312	H. A. Dockery
1	6312	E. Dunn
1	6312	J. H. Gauthier
1	6312	P. G. Kaplan
1	6312	F. C. Lauffer
15	6312	M. L. Wilson
1	6313	L. S. Costin
1	6313	M. E. Fewell
1	6313	E. E. Ryder
1	6313	S. R. Sobolik
1	6313	A. H. Treadway
1	6315	F. B. Nimick, Actg.
1	6315	J. A. Fernandez
1	6315	M. D. Siegel
1	6316	R. P. Sandoval
2	6318	R. J. Macer for 100/12141/SAND91-7034/NQ
1	6319	R. R. Richards
1	6416	L. L. Price
20	6341	WMT Library
1	6410	D. A. Dahlgren
1	8523-2	Central Technical Files

☆ U.S. GOVERNMENT PRINTING OFFICE 1992 - 673-245/54150

SAND91-7034

The number in the lower right-hand corner is an accession number used for Office of Civilian Radioactive Waste Management purposes only. It should not be used when ordering this publication.